NOTE TO USERS

University of Alberta

A Case Study and Comparitive Design of the 130TH Avenue and Deerfoot Trail Overpass

by

Michael William Paulsen ©

A thesis submitted to the Faculty of Graduate Studies and Research in partial fulfillment of the requirements for the degree of **Master of Science**

in

Structural Engineering

Department of Civil and Environmental Engineering

Edmonton, Alberta
Fall 2005

Your file Votre référence
ISBN: 0-494-09261-0
Our file Notre référence
ISBN: 0-494-09261-0

Abstract

External prestressing has shown to be advantageous in segmental construction and rehabilitation, but has not been introduced into general precast construction. A case study and comparative design was performed to determine the effectiveness of external prestressing in highway overpass design. The overpass uses precast-prestressed concrete girders as the main structural elements, made continuous through deck and diaphragms and longitudinally post-tensioned.

Deflections and strains in two girders were monitored from fabrication to service, and a comprehensive material testing program was done on the concrete mix. A model describing all relevant concrete properties was formulated from the testing program and a structural analysis method incorporating the concrete properties was validated through the field study. The method of analysis was expanded, using current literature, to predict the behaviour using external rather than internal tendons. Results show a decrease in weight and more efficient use of prestressing and post-tensioning is possible with external tendons.

Acknowledgements

This research project was conducted under the guidance of Dr. Dave Rogowsky and Dr. Scott Alexander. Their experience, technical skills and wisdom gave me new insight into every area of research and engineering I explored. I have been extremely fortunate to have worked with them.

Financial support for this project was provided by the Natural Sciences and Engineering Research Council of Canada, Con-Force Structures Ltd., the Cement Association of Canada, and the University of Alberta.

Many people at Con-Force Structures Ltd deserve recognition. Bill LeBlanc was instrumental in the formation of this project and continued to provide his support and advice along the way. I would also like to thank Filip Brogowski for providing his technical expertise on the precast industry, and answering my almost daily questions. Many others at Con-Force Structures Ltd deserve recognition for their help in fabrication of the concrete specimens and in the instrumentation of the girders. Additionally, I would like to recognise the help from Dennis Bischoff and Rasvan Pentanca.

I would also like to thank Azita Azarnejad of CH2M Hill Canada. Her technical knowledge of the design of the 130th Avenue and Deerfoot Trail overpass was very helpful throughout the duration of this project.

Throughout my time at the University of Alberta I have received much support from fellow graduate students. This included running material testing, solving technical problems, and providing an extra hand when needed. The interaction with my colleagues contributed greatly to the experience I gained over the past two years. The following deserve a special recognition: Cara Denkhaus, Tim Van Zwol, Dave Taylor, Grant Ormberg, and my good friend Robert Lopetinsky.

Finally I would like to thank family; My parents, Bill and Inger Paulsen for their continued support, and in particular, I would like to thank my wife Isabelle for providing endless support, encouragement and understanding.

Table of Contents

List of Tables

List of Figures

List of Symbols

Symbols

A	Area
A_{ps}	Area of prestressing
$A_{ps,int}$	Area of internal prestressing steel
$A_{ps,tot}$	Total area prestressing steel
B	First moment of area
b_v	Effective web thickness in shear
c	Depth of neutral axis
d_{ps}	Depth of prestressing steel
d_{pso}	Depth of external prestressing steel in the undeformed case
d_{psu}	Depth of external prestressing steel at ultimate condition
E_c	Modulus of elasticity of concrete
$E_{c,aa}$	Age-adjusted elastic modulus of concrete
$E_{c,eff}$	Effective modulus of elasticity of concrete
E_{ci}	Modulus of elasticity of concrete at 28 days of age
E_{ps}	Modulus of elasticity of prestressing steel
$E_{ps,eff}$	Effective modulus of prestressing steel
E_{ref}	Reference modulus of elasticity
f'_c	Specified compressive strength of concrete
f_{cm}	Mean compressive strength of concrete
f_{cmo}	10 MPa

f_{cr}	Tensile strength of concrete
$f_p(x)$	Tendon stress as a function of position along member
f_{pi}	Stress in prestressing steel at time zero
f_{ps}	Tendon stress
f_{pe}	Effective tendon stress
f_{po}	Jacking stress of prestressing tendon
f_{PT}	Tendon stress specifically for post-tensioned tendon
f_{pu}	Ultimate strength of prestressing steel
f_{py}	Prestressing steel yield strength
f_y	Reinforcing steel yield strength
h	Overall depth of section, or notional thickness of concrete section
h_o	100 mm
I	moment of inertia
$\tilde{I}$	Moment of inertia transformed with respect to the reference modulus, E_{ref}
J	Creep function
k_s	A coefficient that accounts for second-order effects
k	Number of degrees of freedom
K	Wobble coefficient
L	Span length
l_e	Effective tendon length
l_i	Length of tendon between anchors
L_1	Length, or sum of lengths of loaded spans affected by the same tendon
L_2	Length of tendon between anchors
L_s	Distance from beam support to loading point
M	Sectional bending moment
M_o	Bending moment due to self-weight
n	Sample size
n_j	Number of prestressing strands in layer j
N	Sectional normal force
N_s	Number of support hinges crossed by an unbonded tendon
N_o	Normal force due to self-weight

P_j	Prestressing force for layer j
R_d	Depth reduction factor
RH	Relative humidity (%)
RH_o	100 %
u	Perimeter of concrete section
L_q	Distance between concentrated loads
S_d	Distance between deviators
s^2	Estimate of population variance
t	Age of concrete
t_s	Age of concrete when drying begins
t_i	Actual age at loading used to compute aging coefficient
$t_{0,Adj}$	Age of concrete at loading, adjusted to account for curing conditions and cement type
T	Temperature
T_0	1^oC
V_c	Concrete contribution to shear resistance
V_r	Factored shear resistance
V_p	Prestressing contribution to shear resistance
t_k	Concrete age adjusted for thermal effects during curing
x	Distance along member
y_{psj}	Distance to centroid of prestressing steel layer j from reference axis
[X]	Matrix of measured data used in multiple linear regression
{y}	Vector of measured data used in multiple linear regression
$\{\hat{y}\}$	Best-fit solution
{Z}	Set of parameters that minimise sum of the square of the residual error
{e}	Vector of residual errors
α	Cumulative angle change of prestressing tendon
α_d	Load factor for dead loads
α_p	Load factor for secondary prestressing effects
Δ	Change in a associated parameter or anchorage set
β	Rate of stress change of tendon with respect to location, x

β_{sc}	Factor depending on cement type
χ	Aging coefficient
χ_r	Reduction coefficient
ε_c	Concrete strain
ε_{cc}	Creep strain
ε_{cs}	Shrinkage strain
ε_{cu}	Concrete strain at ultimate
ε_j	Strain in prestressing in layer j
ε_o	Reference Strain
ϕ_c	Material resistance factor for concrete
ϕ_p	Material resistance factor for prestressing steel
ϕ_s	Material resistance factor for reinforcing steel
ϕ_0	Creep coefficient as ratio of creep strain to initial strain
ϕ_{28}	Creep coefficient as ratio of creep strain to equivalent 28 day strain
μ	Coefficient of friction
Ω_u	Bond reduction coefficient at ultimate
σ_0	Sustained stress
σ_c	Concrete stress
σ^2	Population variance
Σ	Summation
ψ	Section curvature
ρ_p	Ratio of prestressing reinforcement to concrete area
ζ	Fitted parameters as designated by subscript, used in Model A
$\{\zeta\}$	Vector of fitted parameters

Subscripts

c	Associated with the concrete section only
D	Associated with the deck

Superscripts

~	Associated section property is transformed with respect to the reference modulus, E_{ref}
′	Associated section property is transformed with respect to the effective modulus, $E_{c,eff}$
¯	Associated section property is transformed with respect to the age-adjusted modulus, $E_{c,aa}$

1

Introduction

1.1 General

This thesis presents a case-study analysis and comparative design of the 130th Avenue and Deerfoot Trail Overpass located in Calgary, Alberta. This overpass uses precast, prestressed open-top trapezoidal concrete girders as the main structural elements. The overpass is made continuous through a cast-in-place deck and diaphragms, and following hardening of the cast-in-place concrete, the entire structure is longitudinally post-tensioned. This system has been used extensively in Calgary, Alberta, where nine such overpasses have been constructed in the past four years

It is hypothesised that the next step in overpass design will include external post-tensioning. As opposed to internal post-tensioning, where tendons are housed in ducts that are cast into the concrete, external post-tensioning only involves attaching the tendons to the concrete structure at discrete locations.

External post-tensioning has been used extensively in segmentally constructed viaducts in Europe and worldwide over the past three decades. As well, many structures have been strengthened and had their service life extended through the use of external post-tensioning. These uses have highlighted several advantages that point to the benefits of external post-tensioning in highway overpass design.

1.2 Objectives and Scope

The final objective of this research project is to investigate the implications of changing the structural system of the 130th Avenue and Deerfoot trail overpass from internal post-tensioning to external post-tensioning. To achieve this objective, the project was subdivided into three sections.

The first section is concerned with predicting the behaviour of the current standard overpass design. A case study was performed on the 130th Avenue and Deerfoot Trail Overpass in Calgary, Alberta, Canada. This involved material testing of mechanical properties and instrumentation and monitoring of two girders from fabrication to service. The objective of this section is to develop a method of analysis that can accurately predict the behaviour of the structure throughout its service life.

The objective of the second section is to identify what differences in behaviour will result when the structural system is changed from internal post-tensioning to external post-tensioning. A literature review was conducted to identify the differences and determine how to incorporate them into analysis.

The objective of the third section is to compare two viable overpass designs, one internally post-tensioned and one externally post-tensioned, to determine what differences result from the different structural systems. In the first section, a method capable of accurately predicting behaviour was developed for the internally-post tensioned overpass. Through the use of the same methods, with rational changes supported by current literature from the second section, the behaviour of the externally post-tensioned overpass should be accurately predicted. In this manner, a comparison of the designs should provide real insight into the difference resulting from the different structural systems.

1.3 Layout of Thesis

This thesis is laid out in paper format, in accordance with the "Faculty of Graduate Strudies and Research Manual of Regulations and Guidelines for Thesis Preparation". The introduction chapter and conclusions chapter are relevant to the whole thesis, while the remaining chapters have their own introduction and bibliography. The following list provides an overview of the Thesis and the order of the chapters.

Chapter 1: Introduction to the Thesis

Chapter 2: Presents a literature review on the factors affecting analysis of externally post-tensioned beams.

Chapter 3: Presents the results of an intensive material testing program on the concrete mix used in the 130th Avenue and Deerfoot Trail Overpass.

Chapter 4: Provides a comparison of accuracy between two structural analysis methods on the predition of time-dependent deformations of the 130th Avenue and Deerfoot Trail Overpass.

Chapter 5: Provides a comparison of estimated behaviours between an internally post-tensioned overpass and an externally post-tensioned overpass.

Chapter 6: Summary and Conclusions

2

Analysis of Externally Prestressed Beams A Literature Review

2.1 Introduction

Prestressed beams can be classified as one of three types depending on the relationship between the tendons and the concrete beam. They are: 1) beams with internal bonded tendons; 2) beams with internal unbonded tendons; and 3) beams with external tendons. While behaviour of the first two types of beams has been well understood for many years, the behaviour of beams with external tendons has received comparatively little attention.

Research has shown that the behaviour of the three types of beam is very similar prior to decompression of the section (Ramos and Aparicio 1995). However, after decompression, (i.e. when a portion of the section begins to experience tension) the behaviour can be substantially different, and so a prediction of ultimate capacity requires an understanding of the differences of the structural systems and of the parameters affecting ultimate behaviour.

In general, the ultimate moment capacity of beams with internal bonded prestressing is section-dependent. That is, the behaviour of one section is independent of the curvature of adjacent sections. This is due to the bond of the prestressing tendon with the surrounding concrete.

For a beam with internal unbonded tendons, the ultimate capacity is no longer section-dependent, but becomes dependent on the beam's geometry, and in particular, the collapse mechanism (Naaman and Alkhairi 1991a). The increase in tendon stress at the ultimate condition depends on the location and number of plastic hinges required to cause collapse. Because the tendons are internal to the section, they are obliged to deform with the structure. Prior to collapse, tendon strain changes are small, and depend on the overall change in length of the beam at the height of the tendon. At collapse, the tendon length increase is determined by what happens at the locations of the plastic hinges as illustrated in Figure 2.1. The rotation at the hinges affects the length of the unbonded tendon, and is used to determine the increase in tendon strain at ultimate. The prediction of tendon stress is required to predict the ultimate moment capacity of the member.

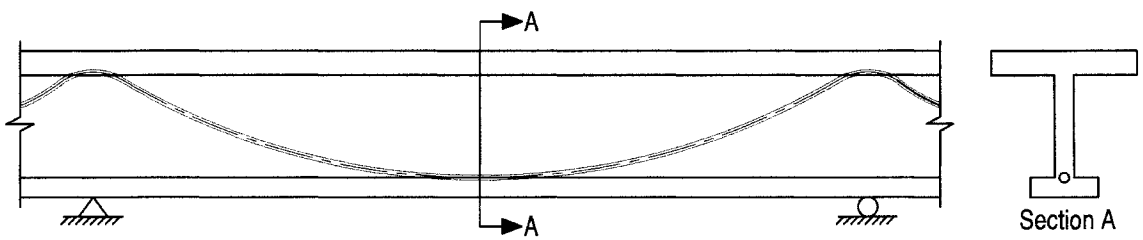

Figure 2.1a Undeformed Condition

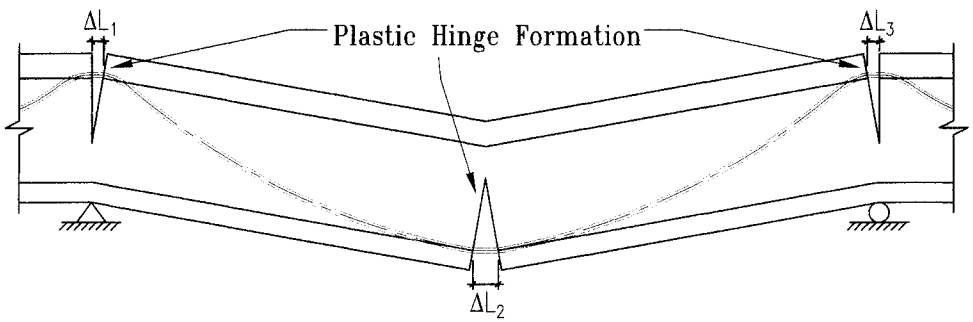

Figure 2.1b Ultimate Condition

Figure 2.1: Continuous Beam with Internal Unbonded Prestressing

For a beam with external tendons, the ultimate moment capacity is not strictly section-dependent, but also depends on the beam's geometry, the location of deviators, and the magnitude of friction at the deviator locations (Virlogeux 1988). Unlike beams with

internal unbonded tendons where the tendon takes the deformed shape of the beam, the tendon in externally prestressed beams is obliged to deform with the structure only at locations of deviators and anchors. Thus, the increase in tendon strain at the ultimate condition is highly dependent on the position of the deviators relative to the position of the hinges. Figure 2.2 illustrates the ultimate condition in a beam with external prestressing. The tendon takes a linear profile between deviators and anchors. As the structure deforms, the eccentricity of the tendon changes. This is referred to as a second-order effect.

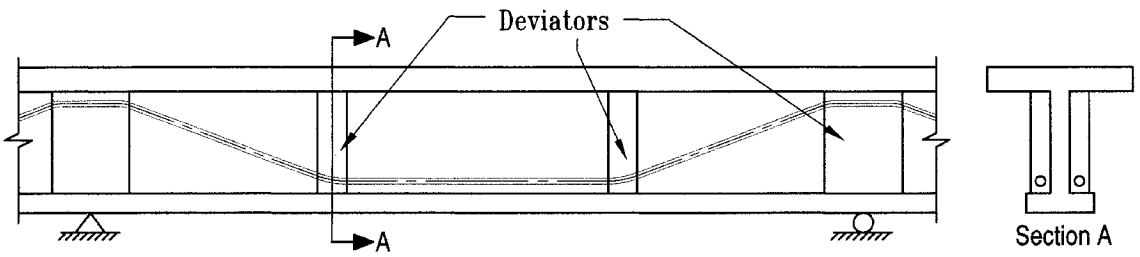

Figure 2.2a Undeformed Condition

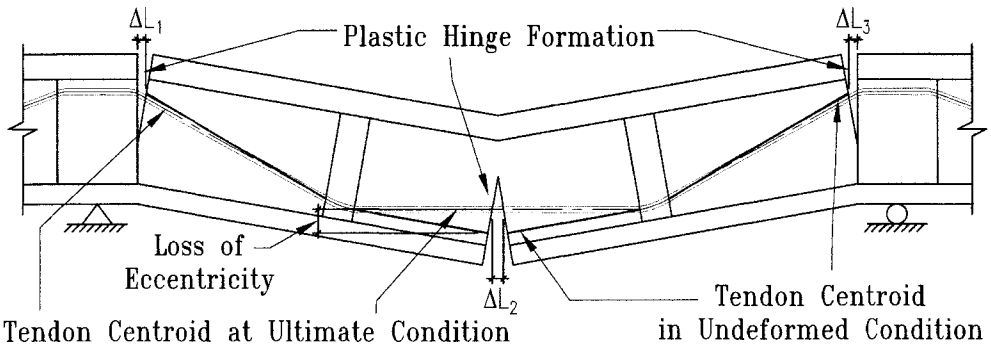

Figure 2.2b Ultimate Condition

Figure 2.2: Continuous Beam with External Prestressing

It will be seen that while the external prestressing system does have the effect of limiting the stress increase in external tendons at ultimate, good design decisions can effectively eliminate the second-order effects associated with loss of tendon eccentricity.

This chapter presents a review of recent and relevant research contributions on the analysis of externally prestressed beams. The goals of this chapter are to 1) understand the basic behaviour of externally prestressed beams, 2) examine how building codes treat externally prestressed beams, 3) determine how design parameters affect behaviour, and 4) present state-of-the-art analysis formulae that can be used in design. This chapter begins with a brief history of external prestressing.

2.2 History

The idea of externally prestressing structures is not new (Virlogeux 1990). External and internal prestressing were developed around the same time. In fact, the impetus to develop external prestressing was to by-pass Freyssinet's patents on the internal prestressing systems.

In the 1960's and 1970's external prestressing did not break through as a viable construction method, as did internal bonded prestressing. Bruggeling (1990) notes that the reasons for this are difficult to ascertain; however, several disadvantages exist.

Early bridges gave a poor picture of externally prestressed structures (Virlogeux 1990). Poor design allowed water to flow along the tendons, which were normally protected only with paint. As well, in some cases, smoke from locomotives, or the acid from bird droppings led to increased corrosion. Virlogeux notes that in all cases, the poor performance was due to corrosion problems and not poor mechanical behaviour of the structures.

The revival of external prestressing in the past three decades can be largely attributed to developments in two other areas of bridge engineering (Bruggeling 1990). The first was the introduction of internal unbonded strands. This required the development of methods of analysis to describe the behaviour of the unbonded strands in service and in ultimate conditions. Second was the development of cable-stayed bridges, where corrosion of the exterior cables and design of anchorage zones had to be considered.

Virlogeux (1990) also notes that in the rehabilitation of some under-strength conventionally prestressed bridges, the only viable option was external prestressing. The experience gained in strengthening these bridges made designers aware of some of the advantages of external prestressing, notably a simplification in layout and a reduction in prestress losses due to friction. Other advantages noted are the ability to replace tendons, and the ability to decrease section weight.

2.3 Analysis and Behaviour

At small deflections, the stress increase in the tendons of internal bonded prestressed beams, internal unbonded prestressed beams and externally prestressed beams is similar. When beam deformations are large enough to cause the decompression of a section, stress increases in the prestressed tendons will depend more on the structural system used.

One effective method of analysing a prestressed section at ultimate is to consider the prestressing tendon as an imposed load on the concrete. The prediction of the ultimate moment capacity is based upon plane-sections theory, strain compatibility of any bonded reinforcing steel in the section and the stress block assumptions used in flexural design of concrete sections. The magnitude and location of the load imposed on the section at ultimate by the prestressing tendon will depend on whether it is bonded or unbonded, and whether it is internal to the section or external.

Figure 2.3 shows a section and strain distribution at ultimate for a beam with internal bonded prestressing. To determine the ultimate moment capacity of the beam, the strain at ultimate in the prestressed tendon, $\varepsilon_{psu,}$ must be predicted. The bond between tendon and concrete allows for the use of strain compatibility to predict ε_{psu}.

In Figures 2.3 through 2.5, the ultimate strain distribution is contrasted with the reference strain distribution. The reference strain distribution represents the section under the

influence of sustained loads and prestress load after all prestress losses (relaxation, creep and shrinkage, etc.). The prestressing strain after all losses is called the effective prestress strain, ε_{pse}.

Figure 2.4 shows a section and strain distribution at ultimate for a beam with internal unbonded prestressing. As is illustrated in Figure 2.1, the strain increase at ultimate cannot be determined from strain compatibility because the tendon is not bonded to the surrounding concrete. To determine the moment capacity of a beam with internal unbonded prestressing, the strain in the tendon, ε_{psu} must be predicted.

Figure 2.5 shows a section and strain distribution at ultimate for a beam with external prestressing. Figure 2.2 illustrates that as an externally prestressed beam is loaded to failure, the tendons are only obliged to follow the deviators. Thus, to determine the ultimate moment capacity of an externally prestressed beam a prediction of both the tendon strain at ultimate, ε_{psu}, and the depth of the tendon at ultimate, d_{psu}, are necessary.

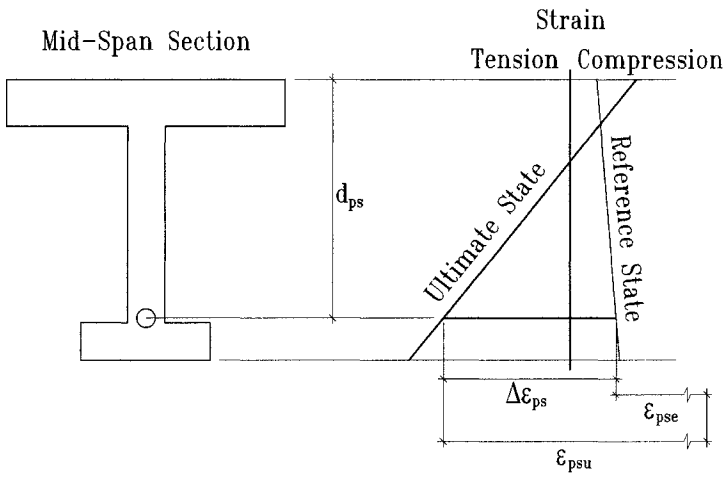

Figure 2.3: Strain Distribution at Mid-Span for an Internal Bonded Prestressed Beam at the Ultimate Moment Capacity

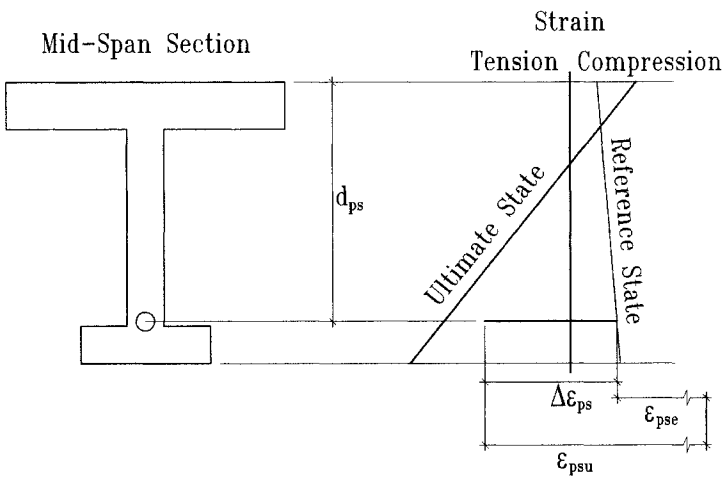

Figure 2.4: Strain Distribution at Mid-Span for an Internal Unbonded Prestressed Beam at the Ultimate Moment Capacity

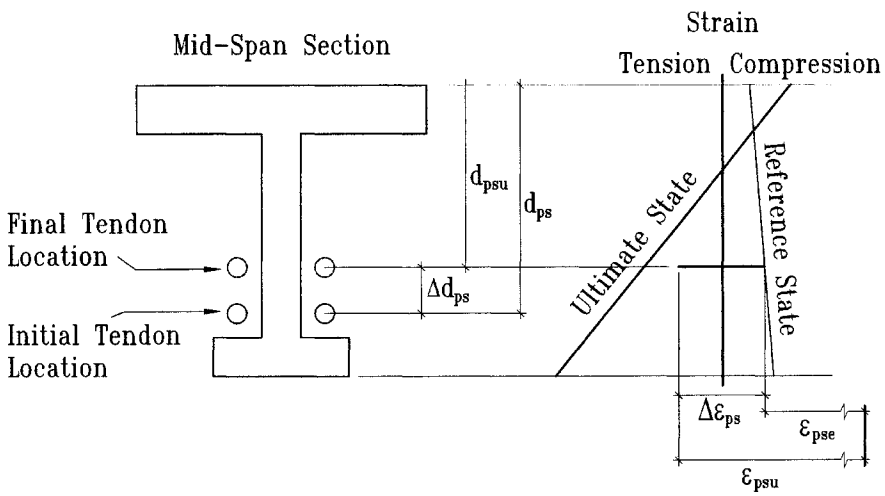

Figure 2.5: Strain Distribution at Mid-Span for an Externally Prestressed Beam at the Ultimate Moment Capacity

2.4 Code Specifications

The purpose of code formulae is to allow a simple and rational approach to predict ultimate and service behaviour in a conservative manner with sufficient accuracy.

Current codes simplify the analysis of beams with unbonded tendons, which is member dependent, to a pseudo-sectional analysis. The theory is that if the stress in the tendon at a particular section can be predicted, then this stress can be used in a sectional analysis. In general, the stress in a prestressed tendon can be represented by:

$$f_{ps} = f_{pe} + \Delta f_{ps} \tag{2.1}$$

where f_{pe} is the effective prestress (corresponding to the effective prestress strain, ε_{pse}), and Δf_{ps} is the stress increase in the tendon for any load increase past the reference state. At the ultimate moment capacity of the beam, the stress in the tendon will be f_{psu}, corresponding to the strain at ultimate, ε_{psu}, in Figures 2.3 through 2.5. If the value of Δf_{ps} at ultimate can be determined for an internal unbonded or external tendon, the prediction of the ultimate moment capacity of the beam will reduce to a plane-sections analysis.

The following sections summarise how various building and bridge codes treat internal unbonded and external prestressing in design. Formulae are all shown in standard metric units, where the tendon stress is in units of MPa.

2.4.1 CSA S6-00 - Canadian Highway Bridge Design Code

For structures with unbonded tendons, the current Canadian Bridge Code (CSA S6-00) allows one to ignore any increase in stress beyond the effective stress in service, i.e. Δf_{ps} = 0 MPa. The code does allow the use of a detailed analysis to determine the stress increase in the tendon at ultimate

The Canadian Bridge Code also specifies that external tendons be treated in the same manner as internal unbonded tendons. While ignoring the increase in tendon stress may be considered conservative, it may underestimate the magnitude of tendon forces acting on end anchorages.

2.4.2 CSA Standard A23.3 - Design of Concrete Structures

The Canadian Standard for the design of concrete structures does not mention external tendons, but does have provisions for predicting the stress increase in unbonded tendons. With some slight changes in nomenclature, A23.3 recommends the tendon stress be calculated according to the following equation:

$$f_{psu} = f_{pe} + \frac{8000}{l_e}(d_{psu} - c) \leq f_{py} \quad \text{(MPa)} \tag{2.2}$$

where l_e is the effective tendon length (mm) and is equal to the ratio of unbonded tendon length to number of plastic hinges required to form a collapse mechanism, d_{psu} is the depth of the prestressing tendon (mm), and c is the depth of the neutral axis (mm) at ultimate. Collapse is due to the formation of plastic hinges, and the unbonded tendon strains due to rotations at the hinges. The derivation of Equation 2.2 implies a deflection of δ=L/100 at failure of a single-span collapse mechanism. From the geometry of the beam at failure, the change in length of the tendon is determined, and is averaged over the length of the unbonded tendon. A modulus of elasticity of 200 GPa was assumed for prestressing steel to calculate stress increase. The limit on tendon stress is its yield strength, f_{py}.

2.4.3 AASHTO 2004 - LRFD Bridge Design Specifications

AASHTO does not provide an estimate of tendon stress for external tendons. For internal unbonded tendons, the equation is similar to the CSA A23.3 recommendation.

$$f_{psu} = f_{pe} + \frac{6300}{l_e}(d_{ps} - c) \leq f_{py} \quad \text{(MPa)} \tag{2.3}$$

Equation 2.3 was originally proposed by MacGregor (1989) for the prediction of tendon stress increase in external unbonded post-tensioned girders. This equation is based on a collapse mechanism resulting from the formation of plastic hinges, and the constant of 6300 is empirically derived from previous experimental studies and corresponds to a collapse mechanism deflection of δ=L/79. MacGregor investigated service and ultimate load behaviour of a segmentally precast box-girder bridge with external post-tensioning, and found good agreement between Equation 2.3 predictions of tendon stress increase and measured values.

2.4.4 ACI 318-99 - Building Code Requirements for Structural Concrete

ACI 318 specifies that external tendons be treated as unbonded tendons. To limit second-order effects, the external tendons are to be attached to the concrete member in a manner that maintains the desired eccentricity throughout the expected range of deflection.

For the prediction of stress in unbonded tendons, ACI 318 specifies the following equations:

For a span-to-depth ratio of 35 or less:

$$f_{psu} = f_{pe} + 68.9\text{MPa} + \frac{f_c'}{100\rho_p} \quad \text{(MPa)} \tag{2.4}$$

where the resultant prestressing stress is limited by:

$$f_{psu} \leq \begin{cases} f_{py} \\ f_{pe} + 414\text{MPa} \end{cases} \quad \text{(MPa)} \tag{2.5}$$

For a span-to-depth ratio greater than 35:

$$f_{psu} = f_{pe} + 68.9MPa + \frac{f'_c}{300\rho_p} \quad (MPa) \tag{2.6}$$

where the resultant prestressing stress is limited by:

$$f_{psu} \leq \begin{cases} f_{py} \\ f_{pe} + 207MPa \end{cases} \quad (MPa) \tag{2.7}$$

In these equations, f'_c is the specified strength of the concrete (MPa) and ρ_p is the prestressed steel ratio.

2.5 Recent Literature

The goal of most research in the field of external prestressing is to determine how to simplify analysis and design by identifying the parameters that have the largest effects on behaviour. For a complete prediction, the analyses are complicated by geometric nonlinearities, which in many cases, are coupled with material nonlinearities. This section discusses research on the most important parameters and their effects on behaviour. These parameters include the effects of friction at deviators, spacing and placement of deviators, external tendon profile, and overall geometry of the member.

2.5.1 Virlogeux (1988)

Virlogeux (1988) was one of the first to discuss the many aspects affecting the behaviour of externally prestressed structures. The aspects identified are the lack of strain compatibility between the external tendon and the concrete at a section, second-order effects, friction and tendon slip at deviators, and joint opening for segmental structures. In addition, an in-depth nonlinear analysis procedure is presented to predict the ultimate capacity of an externally post-tensioned structure based on plastic hinge formation. This procedure involves the complete computation of deformations, including second-order effects and tendon slip at deviators.

One interesting phenomena that is discussed is that tendon slip is non-reversible, and thus if tendon slip is considered in the model, so must the historical sequence of loading. The non-reversibility in tendon slip is a result of the one-way action of friction. Tendon slip always acts to bring tendon stresses on different sides of a frictional barrier closer to a uniform state.

2.5.2 Ramos and Aparicio (1995)

Ramos and Aparicio (1995) investigated the effect of deviator slip on the increase of tendon stress in externally prestressed beams up to ultimate through the use of a numerical model. This model accounts for geometric and material nonlinearities, boundary conditions, monolithic or segmental construction, external or internal tendons, and either no slip, or complete slip at the deviators. The model was compared against previously published data for internal bonded, unbonded and external prestressing beam tests, and the results were shown to be in good agreement.

Their study found that for simply supported bridges, external tendons showed an increase in stress beyond effective prestress that was not negligible. For continuous bridges, the assumption of free slip at deviators led to nearly no increase in stress, but for no slip, the tendons in the continuous bridge showed an increase of 208 MPa.

As well, for their model, failure was ductile, not in the sense of yielding of the tendons, but in large deformations. For continuous bridges large moment redistribution to the supports was predicted.

2.5.3 Rao and Mathew (1996)

Rao and Mathew (1996) investigated the effect of deviators on the increase of tendon stress. They tested eight externally prestressed and four internal unbonded prestressed beams loaded to collapse with 1/3 point loading. They proposed that at the ultimate load case, a tendon that had not slipped in service might slip, reducing the moment capacity. They then identified four cases of slipping at the deviators: 1) slip; 2) no slip; 3) no early slip but slip occurring later; and 4) early slip with no slip later.

For the beams they studied the introduction of a deviator at the section of maximum deflection increased the moment capacity by 11% and the prevention of slip at the deviator further increased moment capacity by 6% (when more than one deviator was used). The centre-deviator was shown to increase ductility.

2.5.4 Tan and Ng (1997)

Tan and Ng (1997) investigated the effects of deviators and tendon configuration on the behaviour of externally prestressed beams. Six beams with span-to-depth ratios of 15 were tested. Five of the beams had straight tendons with either one or two deviators while one beam had a draped tendon profile. The investigation found that a single deviator at the section of maximum deflection provided satisfactory behaviour in service and at ultimate. It was noticed that the beam with a draped tendon configuration exhibited larger ductility at failure than the beams with the straight tendons. They also used the method proposed by Naaman and Alkhairi (1991) to predict the response, and found good agreement, suggesting for this case the second-order effects were negligible.

2.5.5 Harajli et al. (1999)

Harajli et al. (1999) developed a nonlinear analysis model to investigate the second-order effects associated with externally prestressed beams. The model was compared against previously published test data and showed good agreement. Subsequently, a parametric study was performed to investigate the influence of deviators and tendon profile on response. They concluded that, everything else being constant, straight tendons without deviators produce a lower ultimate carrying capacity than straight tendons with deviators, however, the difference between either one or two deviators on a straight tendon was negligible. They also found that deviated tendons mobilised a larger stress increase than undeviated tendons. For all cases, the tendon stress levels remained below yield.

2.5.6 Aparicio et al. (2002)

Aparicio et al. (2002) investigated the effect of tendon length in continuous beams. They concluded that the external tendon length has a significant effect on the behaviour of

externally prestressed beams. Thus any prediction of prestressing steel stress increase at ultimate must consider the tendon length.

2.5.7 Ariyawardena and Ghali (2002)

In an investigation by Ariyawardena and Ghali (2002) a numerical study was performed to test the effect of bonding at deviators and the number of deviators. With two deviators at 1/3 points there was a maximum change in eccentricity of 10%, regardless of slipping at the deviator. As well, stress increases in the external tendons at ultimate were much greater than code predictions.

2.5.8 Harajli et al. (2002)

Harajli et al. (2002) performed numerical modelling and laboratory testing to further investigate the effects of external prestressing on continuous beams. They propose a model based on the concept of a plastic hinge length to predict ultimate behaviour. Testing showed failure occurred in flexure by the formation of a collapse mechanism. Plastic hinges would form initially at the interior supports, then at mid-span. All failures exhibited large ductility at ultimate with the tendon stresses being slightly below or at the yield point. By attaching the tendon to the concrete at the section of maximum deflection, it was found that second-order effects were essentially eliminated and could be analysed assuming internal unbonded prestressing.

2.5.9 Summary

Important factors affecting behaviour of externally prestressed beams were found to be deviator spacing, tendon profile, and span-to-depth ratio. The second-order effects can be minimised through the use of a deviator at the section of maximum deflection. As well, if measures are taken to bond the tendon to the deviators, greater capacity can be attained. Finally, failures were shown to be ductile, which is important for structural safety.

2.6 Development of Simplified Design Methods

The current model codes discussed in section 2.4 do not account for external tendons explicitly. Instead, they either specify that external tendons be treated as internal unbonded tendons, or are silent on the issue.

This portion of the literature review summarises developments in the code style formulae used to predict stress increase in prestressed tendons. It begins with the prediction of stress increase for internal unbonded prestressed beams. This is because the first predictions of the behaviour of beams with external tendons assumed the second-order effects of changing tendon eccentricity were negligible.

2.6.1 Naaman (1990) and Naaman and Alkhairi (1991b)

Naaman (1990) proposed the use of a coefficient, Ω, termed the strain reduction coefficient. This coefficient is defined as the ratio of strain in the perfectly unbonded tendon to the strain in the tendon if it were perfectly bonded. For beams that remain elastic the value of the strain reduction coefficient can be analytically derived.

In effect, this reduces the complex member-dependent analysis to a section analysis, with a stress of f_{psu} in the unbonded tendon. However, this method is limited to use in the elastic cracked and uncracked states. In the case of a strain reduction coefficient equal to 1, the formulae reduce to the case of a bonded tendon.

Naaman and Alkhairi (1991b) then expanded the use of the reduction coefficient to the ultimate strength limit state and termed it the bond reduction coefficient, Ω_u. They attempted to derive the bond reduction coefficient in a rational method, but were unsuccessful. Instead, it was proposed that the value of this coefficient should vary with the span to depth ratio, and be dependent upon the loading conditions. A value of Ω_u was then found by correlating predictions with a database of 143 beam tests. It was also observed that the number of spans loaded (for continuous beams), and the total length of

the tendon between anchors had a significant effect on tendon stress increases. The resultant equation proposed for the prediction of tendon stress was then expressed as:

$$f_{psu} = f_{pe} + \Omega_u E_{ps} \varepsilon_{cu} \left(\frac{d_{ps}}{c} - 1 \right) \frac{L_1}{L_2} \leq 0.94 f_{py} \tag{2.8}$$

where,

$$\Omega_u = \frac{1.5}{\left(L / d_{ps} \right)} \text{ for one-point loading} \tag{2.9}$$

$$\Omega_u = \frac{3.0}{\left(L / d_{ps} \right)} \text{ for third-point or uniform loading} \tag{2.10}$$

and E_{ps} is the modulus of elasticity of the prestressing strand, ε_{cu} is the strain in concrete top fibre at ultimate, L_1 is length or sum of lengths (mm) of loaded spans affected by the same tendon, and L_2 is the length of tendon between anchors (mm).

Equation 2.8 relates the stress in a prestressing tendon to the span-to-depth ratio (L/d_{ps}) through the bond reduction coefficient, and the ratio of depth of neutral axis to depth of prestressing (c/d_{ps}). To account for the effect of pattern loading in beams with tendons continuous over several spans the ratio of length of loaded spans to length of tendon is included as the ratio L_1/L_2.

2.6.2 Mutsuyoshi et al. (1995)

The first major attempt to incorporate the secondary effects of changing tendon eccentricity and deviator spacing into a simplified design method was made by Mutsuyoshi et al. (1995). It was observed that the ultimate load-carrying capacity could be 16% less for externally prestressed beams than for internal unbonded prestressed

beams. The reduction was attributed to the second-order effects, and so, Mutsuyoshi proposed a depth reduction factor, R_d, to account for the reduction of tendon eccentricity at ultimate. From the results of a parametric study, he proposed the following modifications to Equation 2.8:

$$f_{ps} = f_{pe} + \Omega_u E_{ps} \varepsilon_{cu} \left(\frac{d_{psu}}{c} - 1 \right) \leq f_{py} \tag{2.11}$$

where, d_{psu} represents the depth of the external tendon at ultimate. As well, it is noted that Equation 2.11 now limits the stress in the external tendon to its yield strength, rather than 94% of yield as was used by Naaman and Alkhairi.

It was noticed that the location of the deviators affects the magnitude of second-order effects. The following equation for the bond reduction coefficient then replaces Equations 2.9 and 2.10, and is representative for a beam subjected to two symmetrically applied loads:

$$\Omega_u = \frac{\left(1.47 + 10.3 \frac{L_q}{L} \right)}{\left(\frac{L}{d_{ps0}} \right)} - 0.29 \left(\frac{L_q}{L} \right) \left(\frac{S_d}{L} \right) \tag{2.12}$$

where L_q is the distance between the concentrated loads, L is the effective beam span, d_{ps0} is the initial tendon depth, and S_d is the distance between two deviators, placed symmetrically about the centreline of the beam. Refer to Figure 2.6 for the general configuration of an externally prestressed beam. The depth of the external tendon at ultimate is given by:

$$d_{psu} = R_d d_{ps0} \tag{2.13}$$

where the depth reduction factor is given by:

$$R_d = 1.0 - 0.022\left(\frac{L}{d_{ps0} - 5}\right)\left(\frac{S_d}{L} - 0.2\right) + 0.0186\left(\frac{L}{d_s}\right)P_m \tag{2.14}$$

$$P_m = \frac{A_s f_y}{b d_s f_c'} \tag{2.15}$$

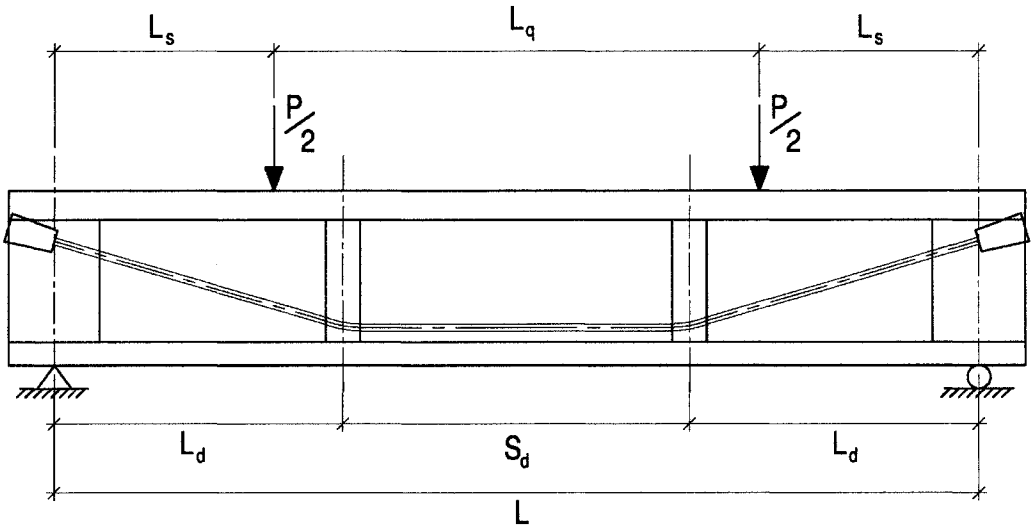

Figure 2.6: General Description of an Externally Prestressed Beam

2.6.3 Aravinthan et al. (1997)

It was noticed by Aravinthan et al. (1997) that the method proposed by Mutsuyoshi et al. (1995) was not applicable to beams with combinations of internal bonded and external tendons. A subsequent research program attempted to expand the use of Equation 2.11 by suggesting new strain reduction and depth reduction coefficients. Through an analytic parametric study, the following values were suggested for these coefficients.

$$\Omega_u = \frac{0.21}{\left(L/d_{ps}\right)} + 0.04\left(\frac{A_{ps,int}}{A_{ps,tot}}\right) + 0.04 \qquad \text{for one-point loading} \qquad (2.16)$$

$$\Omega_u = \frac{2.31}{\left(L/d_{ps}\right)} + 0.21\left(\frac{A_{ps,int}}{A_{ps,tot}}\right) + 0.06 \qquad \text{for third-point loading} \qquad (2.17)$$

$$R_d = 1.14 - 0.005\left(\frac{L}{d_{ps}}\right) - 0.19\left(\frac{S_d}{L}\right) \le 1.0 \qquad \text{for one-point loading} \qquad (2.18)$$

$$R_d = 1.25 - 0.010\left(\frac{L}{d_{ps}}\right) - 0.38\left(\frac{S_d}{L}\right) \le 1.0 \qquad \text{for third-point loading} \qquad (2.19)$$

2.6.4 Ng (2003)

In previous research, the development of simplified equations for analysis of externally prestressed beams was associated with internal unbonded prestressed beams. In unbonded prestressed beams the span-to-depth ratio has a significant effect on ultimate-capacity and tendon stress increase. An investigation by Ng (2003) showed theoretically and experimentally that the stress increase in external tendons is independent of the span-to-depth ratio.

Ng proposed a similar method to Mutsuyoshi et al. (1995) for determining tendon stress at ultimate, but noted that the parameter (S_d/L) is not appropriate for consideration of second-order effects. The reason is that two beams with the same (S_d/L) ratio, but different lengths will experience different magnitudes of second order effects. Instead Ng (2003) chose the deviator separation to initial prestress depth ratio (S_d/d_{ps0}) as the parameter to describe second-order effects. The final set of equations given by Ng

account for second-order effects and predict the stress increase in external tendons better than those given by Mutsuyoshi (1995).

To calculate the stress in an externally prestressed tendon at ultimate:

$$f_{ps} = f_{pe} + \Omega_u E_{ps} \varepsilon_{cu} \left(\frac{d_{ps0}}{c} - 1 \right) \leq f_{py} \tag{2.20}$$

where,

$$\Omega_u = \left[0.895 - 1.364 \left(\frac{L_s}{L} \right) \right] \left(\frac{d_{ps0}}{h} \right) - k_s \tag{2.21}$$

In Equation 2.21, L_s is the distance from beam support to the loading point (or the shear span length) and h is the overall beam depth. The equation for the bond reduction coefficient is then a function of loading and initial depth of prestressing. Second order effects are accounted for with the coefficient k_s:

$$k_s = 0.0096 \left(\frac{S_d}{d_{ps0}} \right) \quad \text{for} \quad \left(\frac{S_d}{d_{ps0}} \right) \leq 15 \tag{2.22}$$

$$k_s = 0.144 \quad \text{for} \quad \left(\frac{S_d}{d_{ps0}} \right) > 15 \tag{2.23}$$

The stress of the external tendon can thus be determined at ultimate include second-order effects of tendon eccentricity. However, as the beam deflects, the eccentricity of the tendon changes with respect to the concrete section (except at points of deviation). If at the critical section the concrete is not attached to the tendon by means of a deviator, the tendon depth at ultimate is not the same as initially. Ng (2003) suggests an iterative

procedure to be used to determine the ultimate moment capacity to a desired level of accuracy.

2.7 Summary

The review of current literature shows that model code formulae do not contain special provisions for external prestressing. In general, codes specify that beams with external tendons be treated in the same manner as beams with internal unbonded tendons.

In the analysis of beams with externally prestressed tendons, simple design-type equations are required to avoid rigorous numerical or analytical models. Research over the past two decades shows that factors specific to external tendons, like deviator spacing and tendon profile, have significant effects on behaviour. The equations for the analysis of internal unbonded prestressed beams are not applicable to externally prestressed beams, unless the factors differentiating the two are negligible. Thus in the case of minimal second-order effects and friction free deviators, unbonded formulae can be used.

Recently, steps have been made in developing simple design-type equations for analysis of externally prestressed beams. The proposed formulae reduce the nonlinear models to a set of equations that predict stress increase in the tendon. Parameters have been identified that include second-order effects, and the results have been shown to be reasonably accurate.

Good design decisions can effectively eliminate the second-order effects associated with loss of tendon eccentricity. A deviator placed at the section of maximum deflection has been shown to minimise second-order effects. For this case, the tendon is obliged to deform with the structure much in the same way as internal unbonded tendons and model code recommendations can be used.

If second-order effects are of concern, than the most recent method, proposed by Ng (2003) and presented in section 2.6.5 is recommended for use in predicting tendon stress increases at ultimate.

2.8 References

AASHTO. 2004. *LRFD Bridge Design Specifications - Second Edition*, American Association of State Highway and Transportation Officials, Washington, D.C.

ACI. 1999. *ACI 318, Building Code Requirements for Reinforced Concrete*, ACI, Detroit, Michigan, USA.

Aparicio, A.C., Ramos, G., and Casas, J.R. 2002. *Testing of Externally Prestressed Concrete Beams*, Engineering Structures, vol 24, no 1, pp. 73-84.

Aravinthan, T., Mutsuyoshi, H., Fujioka, A., and Hishiki, Y. 1997. *Prediction of the Ultimate Flexural Strength of Externally Prestressed PC Beams*, Transactions of the Japan Concrete Institute, vol. 19, pp 235-240.

Ariyawardena, N.D. and Ghali, A. 2002. *Design of Precast Prestressed Concrete Members Using External Prestressing*, PCI Journal, vol 47, no 2, pp 84-91.

Beaupre, R.J., Powell, L.C., Breen, J.E., and Kreger, M.E. 1990. *Deviator Behaviour and Design for Externally Post-Tensioned Bridges*, SP-120, American Concrete Institute, Detroit, MI, pp. 257-288.

Bruggeling, A.S.G. 1990. *External Prestressing – a State of the Art*, SP-120, American Concrete Institute, Detroit, MI, pp. 61-82.

CSA. 1994. *CSA Standard A23.3-M94, Design of Concrete Structures*, Canadian Standard Association, Toronto, Ontario, Canada.

CSA. 2000. *S6-00 Canadian Highway Bridge Design Code*, CSA International, Toronto, Ontario, Canada.

Harajli, M., Khairallah, N., and Nassif, H. 1999. *Externally Prestressed Members: Evaluation of Second-Order Effects*, Journal of Structural Engineering, vol 125, no 10, pp. 1151-1161.

Harajli, M.H., Mabsout, M.E., and Al-Hajj, J.A. 2002. *Response of Externally Post-Tensioned Continuous Members*, ACI Structural Journal, vol 99, no 5, pp. 671-680.

Mutsuyoshi, H., Tsuchida, K., Matupayont, S., and Machida, A. 1995. *Flexural Behaviour and Proposal of Design Equation for Flexural Strength of Externally Prestressed Concrete Members*, Proceedings of Japan Society of Civil Engineers, vol 26, no 508, pp 103-111.

MacGregor, R. J. G. 1989. *Evaluation of Strength and Ductility of a Three-Span Externally Post-Tensioned Box Girder Bridge Model*, Ph.D. Dissertation, The University of Texas at Austin, USA, 1989.

Naaman, A.E. and Alkhairi F.M. 1991a. *Stress at Ultimate in Unbonded Post-Tensioning Tendons: Part 1 – Evaluation of the State-of-the-Art*, ACI Structural Journal, vol 88, no 5, pp. 641-651.

Naaman, A.E., and Alkhairi, F.M. 1991b. *Stress at Ultimate in Unbonded Post-Tensioning Tendons: Part 2 – Proposed Methodology*, ACI Structural Journal, vol 88, no 6, pp. 683-692.

Naaman, A.E. 1990. *A New Method for the Analysis of Beams Prestressed with External or Unbonded Tendons*, SP-120, American Concrete Institute, Detroit, MI, pp. 339-354.

Ng, C.H. 2003. *Tendon Stress and Flexural Strength of Externally Prestressed Beams*, ACI Structural Journal, vol 100, no 5, pp. 644-653.

Ramos, G., and Aparicio, A.C. 1995. *Ultimate Behaviour of Externally Prestressed Concrete Bridges*, Journal of IABSE, Structural Engineering International, n 3, pp 172-177.

Rao, P.S., and Mathew, G. 1996. *Behaviour of Externally Prestressed Concrete Beams with Multiple Deviators*, ACI Structural Journal, vol 93, no 4, pp. 387-396.

Tan, K.H., and Ng, C.H. 1997. *Effects of Deviators and Tendon Configuration on Behaviour of Externally Prestressed Beams*, ACI Structural Journal, vol 94, no 1, pp. 13-22.

Virlogeux, M.P. 1988. *Non-Linear Analysis of Externally Prestressed Structures*, Proceedings of the FIP Symposium, Jerusalem, Israel, pp 318-340.

Virlogeux, M.P. 1990. *External Prestressing: from Construction History to Modern Technique and Technology*, SP-120, American Concrete Institute, Detroit, MI, pp. 1-60.

Characterizing the Time-Dependent Mechanical Properties of a HPC

3.1 Introduction

High-Performance Concrete (HPC) as a structural material is continually gaining in popularity. The construction of long-span bridges and other slender structures, along with the push for longer service lives are the main driving forces. The advantages of HPC can include a higher strength, a greater durability, and an increased ease of placement.

An accurate prediction of the time-dependent behaviour of concrete is necessary, especially for slender structures, to ensure that they remain serviceable. A failure in predicting the concrete's stiffness, shrinkage and creep can result in excessive camber, sag or shortening, joint separation, or cracking.

The problem is that many atypical concretes can be considered high-performance mixes, and thus, with continually new admixtures, mixing process and curing regimes, the prediction of HPC mechanical properties becomes difficult. As well, it is becoming more desirable to perform a probabilistic analysis on aspects of design to determine the

confidence of the performance of the structure. Unfortunately, most model codes do not include a detailed approach to include variability.

With these ideas in mind, a research program was designed to investigate the time-dependent properties of a particular high performance structural concrete mix. The objectives of this study were to 1) experimentally determine the mechanical properties of the HPC mix; 2) assess the predictive abilities of current model codes on the mechanical properties; 3) propose a straightforward statistical method to fit laboratory test data to a general model; and 4) propose a method of determining variability of the fitted model.

3.2 Background

3.2.1 Mechanical Properties

The calculation of time-dependent structure deformation requires an estimation of the mechanical properties of the concrete used, specifically those related to strength, stiffness, shrinkage and creep.

As opposed to ultimate design, where the compressive strength of concrete is directly used to predict ultimate capacity, with serviceability calculations the strength of concrete is only indirectly used. A measure of the concrete strength is required because other properties such as tensile strength or stiffness are usually correlated to the strength. Typically, it is the concrete's compressive strength as determined from concrete cylinders tested in accordance with ASTM C 39/C39M-01 (2002) that is needed.

The concrete's stiffness is used in the calculation of elastic deflection, transforming sections, or when computing prestress relaxation resulting from creep and shrinkage. The modulus of elasticity as determined by ASTM C 469-94e1 (2002) is a common measure of stiffness, and corresponds to the secant modulus calculated at 40 percent of the compressive strength.

Shrinkage is defined as the time-dependent volume change that is not associated with load or temperature. The primary source of shrinkage is moisture loss. To a lesser extent, chemical changes during hydration also lead to volumetric change. The ASTM standard for the testing of creep of concrete cylinders provides a measure of shrinkage that includes all non-load/temperature related strains.

Creep is the increase in strain associated with a sustained stress. It is arguably the most complex of the mechanical properties, and is of vital importance when deflections are of concern. Creep of concrete is nonlinear with respect to time and with respect to the magnitude of the sustained load. However, when the applied stress is less than 40 percent of the concrete compressive strength, a nearly linear relationship exists between sustained stress and creep strain. In design, building and bridge codes limit the magnitude of sustained stress in the concrete to the linear region. For this reason, ASTM C 512-87 (1994), the common standard for testing of creep in compression, specifies that the sustained stress in creep tests be less than 40 percent of the compressive strength.

The most common approach to incorporate creep into structural analysis equations is to describe it using the creep coefficient; however, two definitions exist. Equation 3.1 defines the creep coefficient as the ratio of creep strain to elastic strain at loading, while Equation 3.2 defines the creep coefficient as the ratio of creep strain to the elastic strain that would result if the concrete were loaded at 28 days.

$$\phi_0(t,t_0) = \varepsilon_{cc}(t,t_0) \cdot \frac{E_c(t_i)}{\sigma_0} \tag{3.1}$$

$$\phi_{28}(t,t_0) = \varepsilon_{cc}(t,t_0) \cdot \frac{E_c(28)}{\sigma_0} \tag{3.2}$$

3.2.2 Model Predictions

To predict these properties, four models will be considered. They are, AASHTO LRFD Design Specification (AASHTO, 2004), ACI 209 (1997), Comité Euro-International du

Béton Model Code 1990 (1993) (CEB MC-90) and the Canadian Highway Bridge Design Code (2000) (CSA S6-00). Table 3.1 shows a comparison between the models as to which parameters are taken into account.

Table 3.1: Model Code Comparison

Property	Parameter	Model			
		AASHTO	ACI 209	CEB MC-90	CSA S6-00
Strength	Specified Strength				
	Cement type				
	Curing Regime				
Stiffness	Compressive Strength				
	Concrete Density				
Shrinkage	Age at Drying				
	Relative Humidity				
	Shape				
	Compressive Strength				
	Cement type				
	Concrete Composition				
	Curing Regime				
Creep	Age at Loading				
	Relative Humidity				
	Shape				
	Compressive Strength				
	Cement type				
	Concrete Composition				
	Curing Regime				

Shaded cell indicates the associated parameter is taken into account

3.2.3 Variability

The aforementioned models provide an estimate of the mean behaviour. However, for service calculations, the use of extreme values of behaviour based on a small probability of exceedance provides a more rational approach. The issue of variability is covered by the separate codes with different degrees of sophistication.

AASHTO states, "Without physical tests or prior experience with the materials, the use of the empirical methods referenced in these Specifications cannot be expected to yield results with errors less than ± 50 percent."

ACI 209 recognises that the contributing factors to predicting time-dependent deformations have coefficients of variation in the order of 15 to 20 percent at best. To incorporate variability, it states that probabilistic methods are necessary to determine the random nature of the parameters involved.

CSA S6-00 states only that the data used to develop its recommendations exhibits a 30 percent scatter.

CEB MC-90 states values for the mean coefficient of variation of both the creep function and shrinkage strain. These values have been based on data banks of test results, and are 35 percent for shrinkage and 20 percent for the creep function. In addition, assuming a normal distribution, CEB MC-90 also provides 10 and 5 percent cut-off values for both the shrinkage strain and creep coefficient. For 5 percent cut-off, which is similar to the 95 percent confidence interval, the lower and upper values are $0.42\varepsilon_{cs}$ and $1.58\varepsilon_{cs}$, and $0.66\phi_{28}$ and $1.34\phi_{28}$ for shrinkage strain and creep respectively. Here ε_{cs} is the predicted shrinkage strain and ϕ_{28} is the predicted creep coefficient.

To assess the sensitivity of the concrete model to variations in input parameters, the uncertainty resulting from each parameter should be considered. The sources of uncertainty in the prediction of time-dependent effects in concrete can be classified as one of two types: external and internal. External or parametric uncertainties, such as environmental conditions or specimen shape, are those that result from variability of input parameters. Internal or model uncertainties result from inadequacies or inaccuracies inherent in the model. While a measure of the variation in external uncertainties can be fairly easily and accurately estimated, the internal uncertainty is rarely considered.

3.3 Experimental Program

3.3.1 High-Performance Concrete Mix

The concrete mix tested was made from a standard mix design used in the production of medium-span (30-60m) prestressed bridge girders in Alberta, Canada. This mix is designed to have the following characteristics: early high strength, ease of placement and high durability. High early strength is required to facilitate prestressing, ease of placement allows minimum vibration and thus minimum segregation during fabrication, and a high durability avoids deterioration issues throughout the service life. The high-performance concrete criteria are summarised in Table 3.2. The mix design used to meet these criteria is presented in Table 3.3.

Table 3.2: HPC Mix Requirements

Criteria	Specified Mix Design Requirement
High Early Strength	40 MPa at 12 hours (60 MPa at 28 days)
Ease of Placement	250 mm slump (50 mm slump before superplasticizing admixture)
Durability	w/c = 0.30 Steam Curing

Table 3.3: HPC Mix Design

Material	Quantity
Type 10 cement	500 kg/m^3
Silica fume	50 kg/m^3
Fine aggregate	646 kg/m^3
Coarse aggregate	950 kg/m^3
Water	165 kg/m^3
Superplasticizer admixture	6 L
Air entraining admixture	6%
Plastic Unit weight	2317 kg/m^3

3.3.2 Specimens and Curing Conditions

Testing was done using nominally 150 x 300 mm cylinders. During the production of concrete girders, the HPC mix is batched in volumes of 2.2 m^3. For this testing program concrete cylinders were made from two separate batches, with each batch being produced in the same manner as during production.

Two methods of curing were used. They are referred to as Method 1 and Method 2, and are shown graphically in Figure 3.1. The two methods have the same secondary curing regime but differ in their primary curing regime.

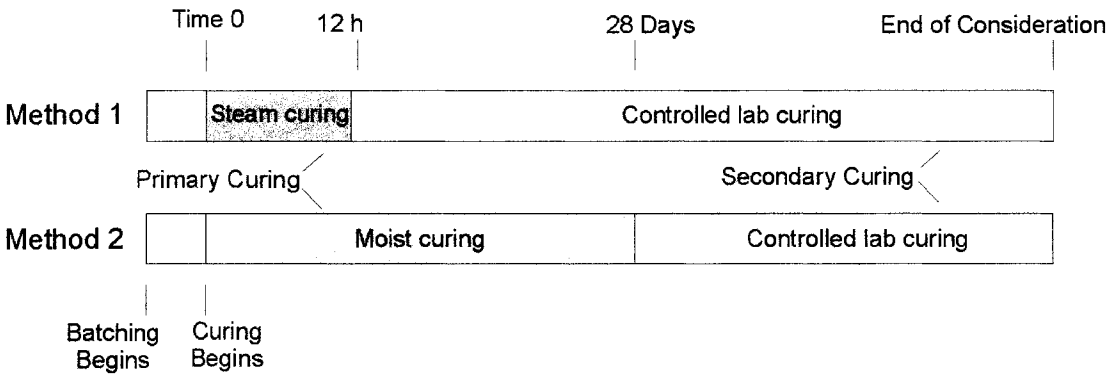

Figure 3.1: Curing Regime

For Method 1, the primary curing (Steam curing) simulates the actual curing conditions that this mix would experience when used in the fabrication of prestressed concrete elements. Specimens were exposed to direct steam, and draped with tarps.

For Method 2, standard moist curing was used as the primary curing regime, where the cylinders were kept in a moist room maintained at a relative humidity of 100% and temperature of $23 \pm 1.7^{\circ}C$.

The secondary curing (Controlled lab curing) follows standard environmental conditions as set out by ASTM C 512 for creep tests, where the relative humidity was maintained at $50 \pm 4\%$ and the temperature was maintained at $23 \pm 1.7^{\circ}C$.

The difference between curing regimes was also measured using thermocouples placed in the centre of the cylinders. One cylinder from each curing method was instrumented. Figure 3.2 shows the temperature reached at the centre of the cylinders for the first 21 hours of curing.

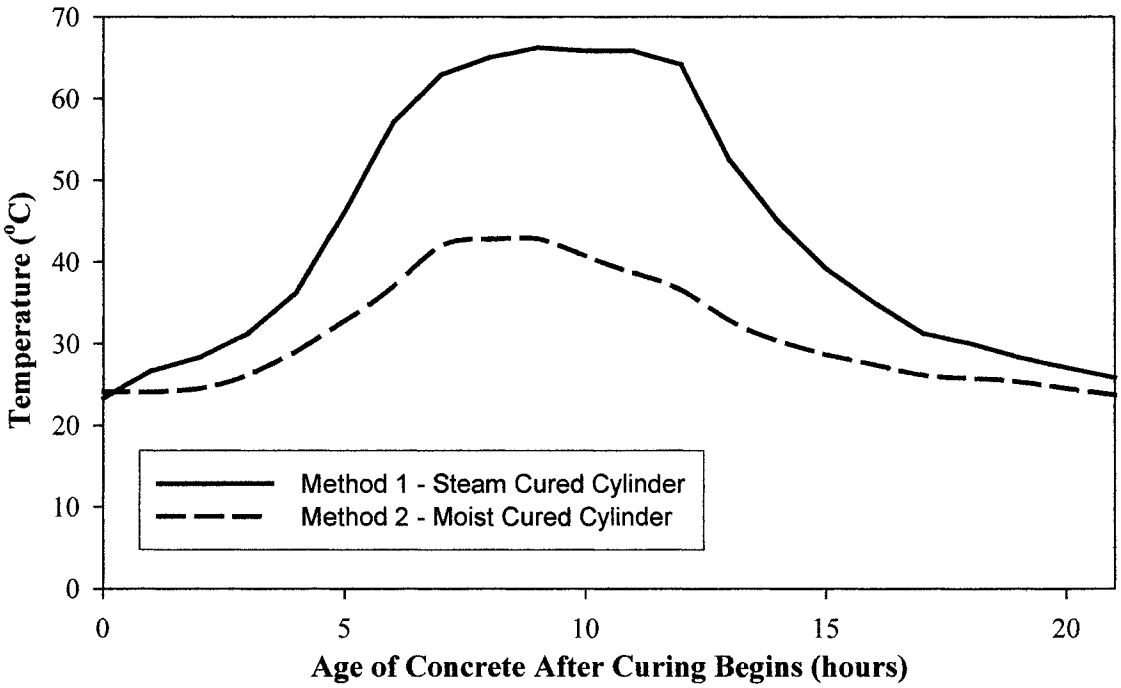

Figure 3.2: Thermal Profiles for Curing Regimes

3.3.3 Methodology

Laboratory testing was conducted to determine the mechanical properties of the HPC mix that include strength gain with time, modulus of elasticity, shrinkage and creep. The testing parameters are summarised in Table 3.4.

Table 3.4: Testing Parameters

Property	Testing Parameter	Parameter Values (Days)	
		Curing Method 1	Curing Method 2
Strength	Concrete Age	1, 2, 3, 8, 10, 15, 28, 84	3, 28
Stiffness	Concrete Age	1, 8, 10, 15, 28, 84	28
Shrinkage	Age Drying Commences	0.43, 8	28
Creep	Age at Loading	1, 8, 28, 84	28

Compressive strength testing was conducted in accordance with ASTM C 39 and stiffness testing was conducted in accordance with ASTM C 469.

For each shrinkage test series, three cylinders were instrumented and measured using demountable mechanical extensometers (DEMECs) to measure strains. Each test cylinder was instrumented with 3 sets of DEMECs placed longitudinally and at equal spacing around the cylinder. Nine readings of shrinkage strains were taken from each cylinder, making every data point the average of 27 readings.

Two shrinkage test series were conducted for curing Method 1. In both cases the drying began at 12 hours (after primary curing), but for test series 1, the initial reading was made at 0.43 days, while for series 2 the initial reading was made at 8 days. For the test series cured in accordance with Method 2, strain measurements were made at the initial onset of drying.

Creep tests were conducted in accordance with ASTM C 512-87(1994). For each age at loading three cylinders were instrumented and measured in the same manner as with the shrinkage cylinders. The magnitude of the constant load applied to the cylinders was 203 kN which corresponds to an average stress of 11.2 MPa.

3.4 Experimental Results

The results for strength testing are shown in Figure 3.3. As well, the predictions made by ACI 209-92 and CEB MC-90 are shown for comparison. Neither CSA S6-00 nor AASHTO provide Equations for the prediction of strength gain with time.

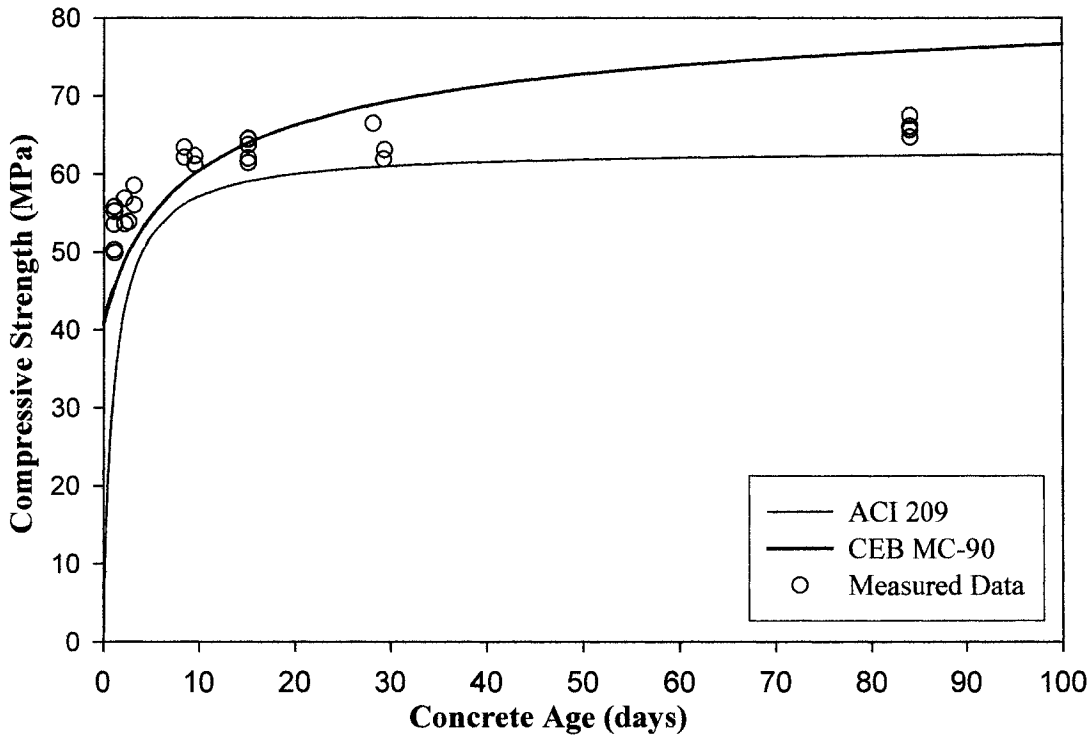

Figure 3.3a: Accelerated Cured (Method 1)

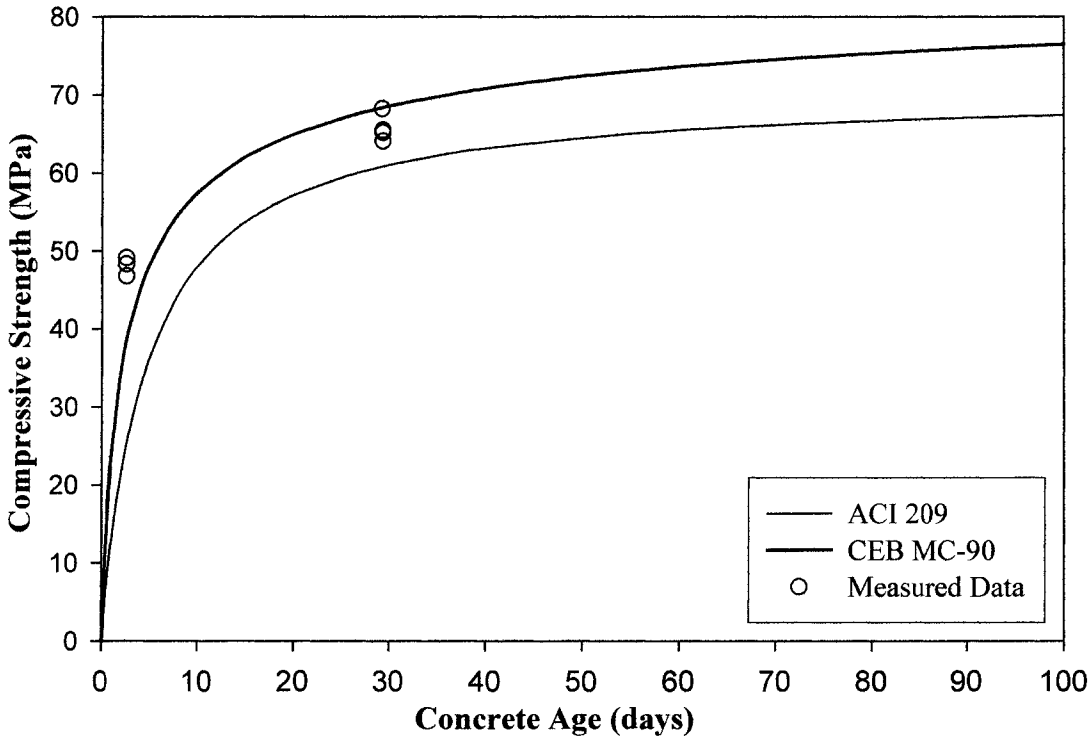

Figure 3.3b: Moist Cured (Method 2)

Figure 3.3: Compressive Strength Gain with Time

The results for stiffness testing are shown in Figure 3.4. The measured modulus of elasticity is shown as a function of stiffness, along with code predictions. The predictions are the same regardless of the curing method allowing both test series to be plotted on the same figure. Both ACI 209 and AASHTO give the same prediction for modulus of elasticity.

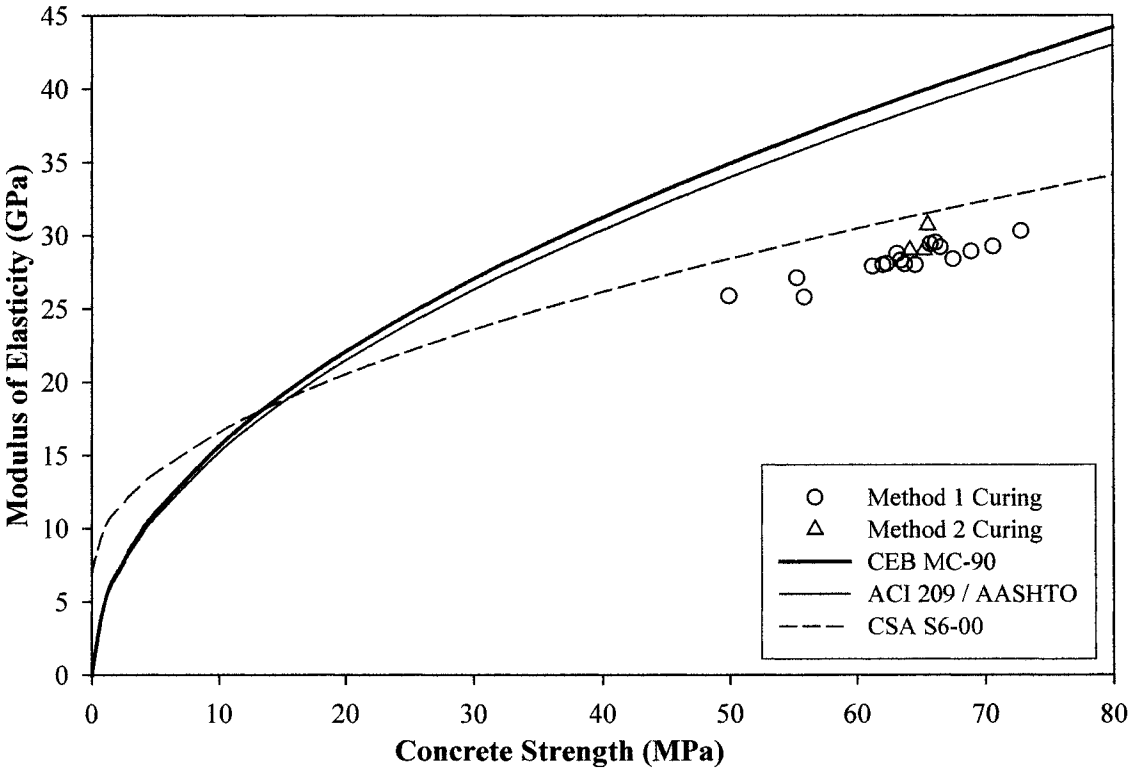

Figure 3.4: Modulus of Elasticity

The results from the shrinkage testing are shown in Figures 3.5 and 3.6. The prediction equations used only consider the shrinkage occurring after the primary curing phase is complete. This is also the shrinkage strain that is measured using the standard test method. Figure 3.5 shows the predictions for the cylinders cured in accordance with Method 1. The initial readings are 0.43 days and 7.9 days, and model predictions have been zeroed accordingly. Figure 3.6 shows the measured shrinkage and predictions for shrinkage occurring after 28 days of primary (moist) curing.

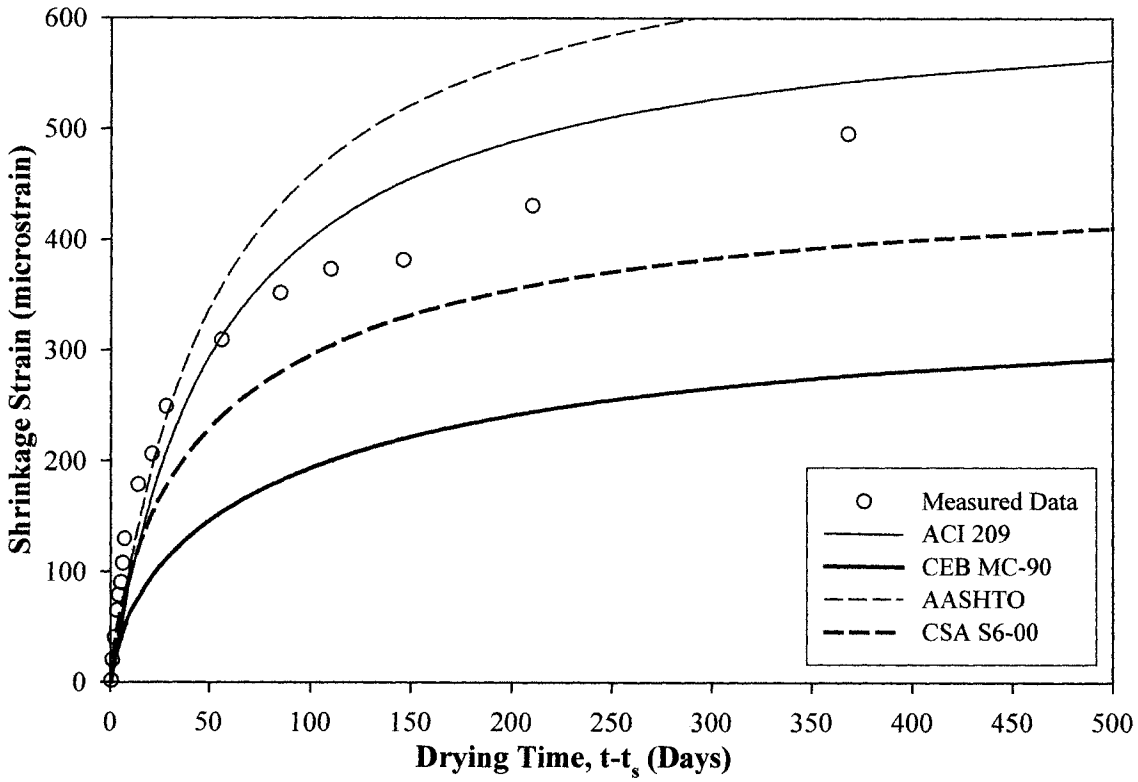

Figure 3.5a: Shrinkage with First Measurement at 0.43 Days

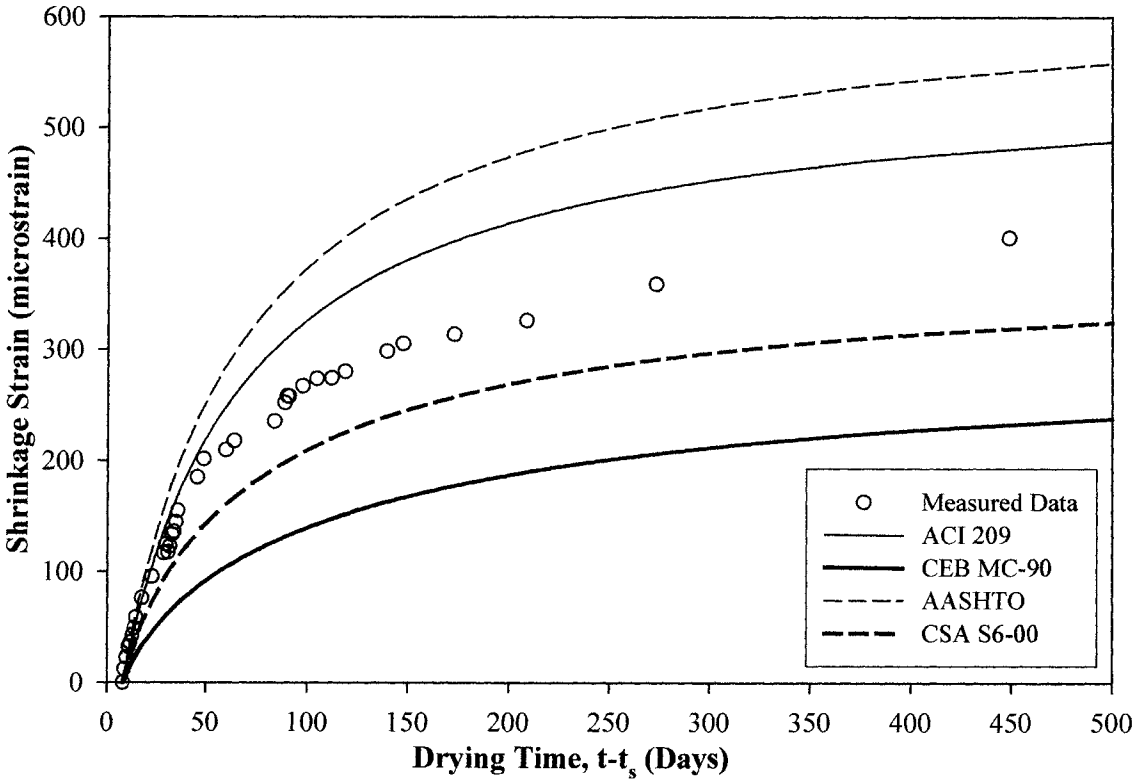

Figure 3.5b: Shrinkage with First Measurement at 7.91 Days

Figure 3.5: Shrinkage of Accelerated (Method 1) Cured Cylinders

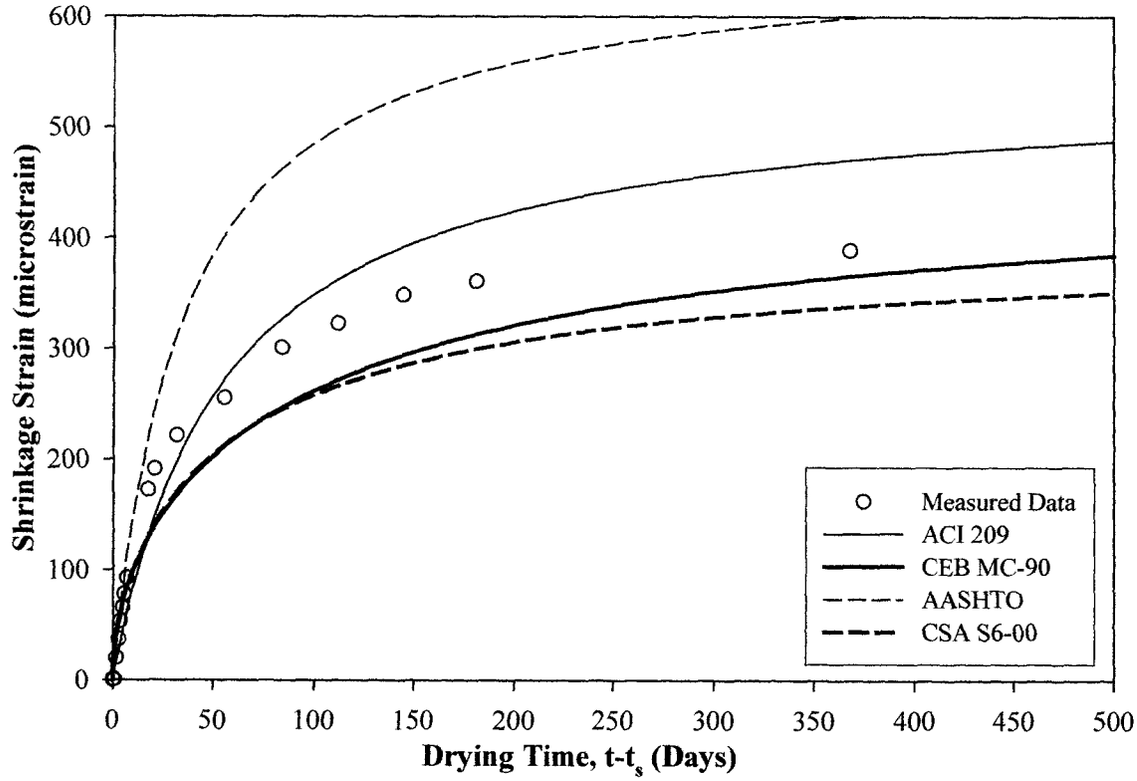

Figure 3.6: Shrinkage of Moist (Method 2) Cured Cylinders

The results from the creep tests are shown in Figures 3.7 and 3.8. These figures show creep as characterised by the creep function, which is expressed in units of strain per unit stress, and gives the total load-related strain resulting from an applied unit stress. This allows for a direct comparison of predictive abilities of the four models considered. ACI 209 uses the definition of Equation 3.1 for the creep coefficient while CEB MC-90 uses the definition of Equation 3.2. And because both AASHTO and CSA S6-00 only use the specified 28-day strength to characterise the mix, both definitions of the creep coefficient are equivalent. The definition of the creep function is shown in Equation 3.3.

$$J(t,t_0)=\frac{1}{E_c(t_0)}+\frac{\phi_0(t,t_0)}{E_c(t_0)}=\frac{1}{E_c(t_0)}+\frac{\phi_{28}(t,t_0)}{E_c(28)} \tag{3.3}$$

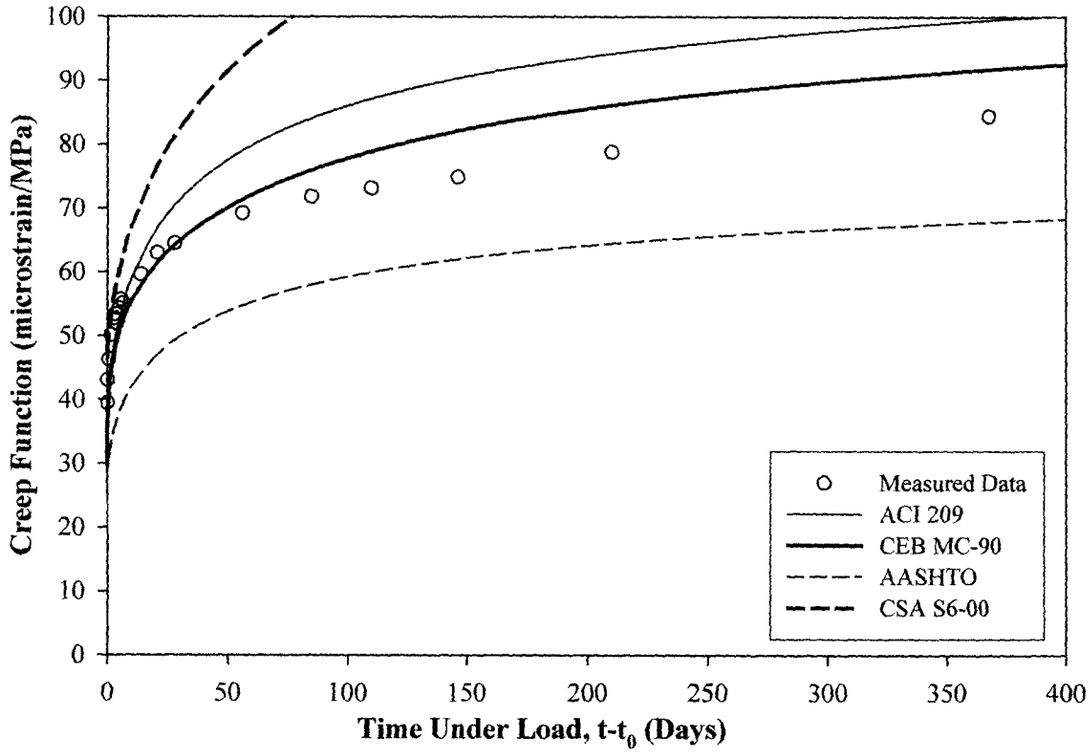

Figure 3.7a: Creep Function for 1.3 day Age at Loading

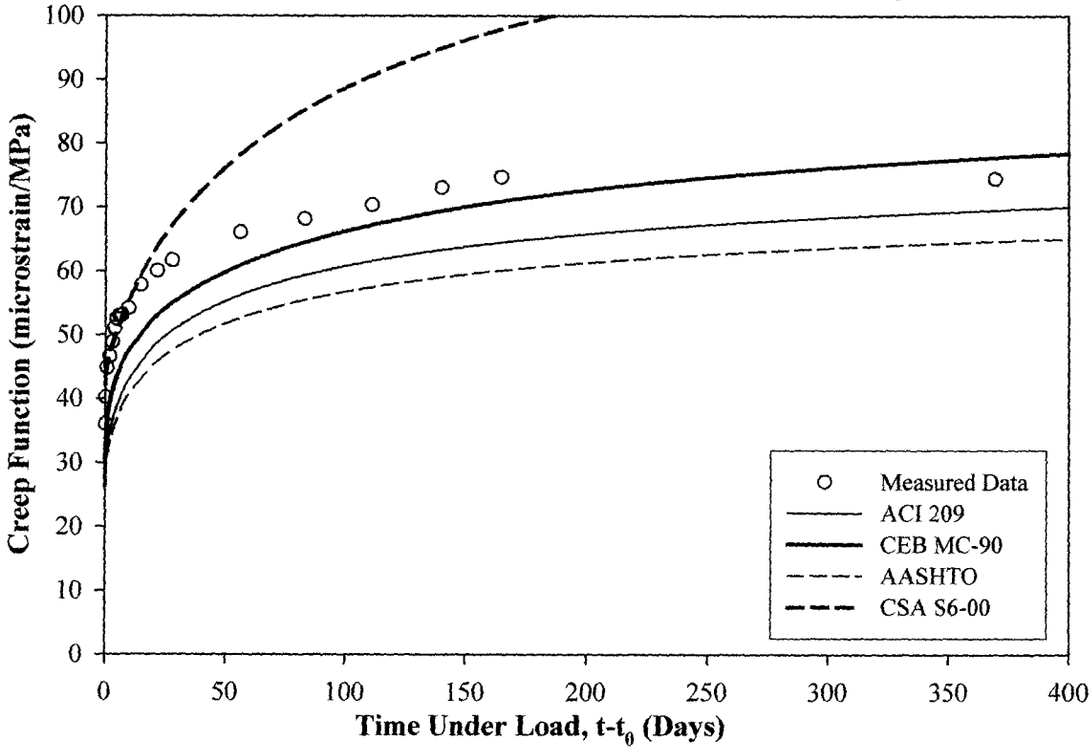

Figure 3.7b: Creep Function for 8.4 day Age at Loading

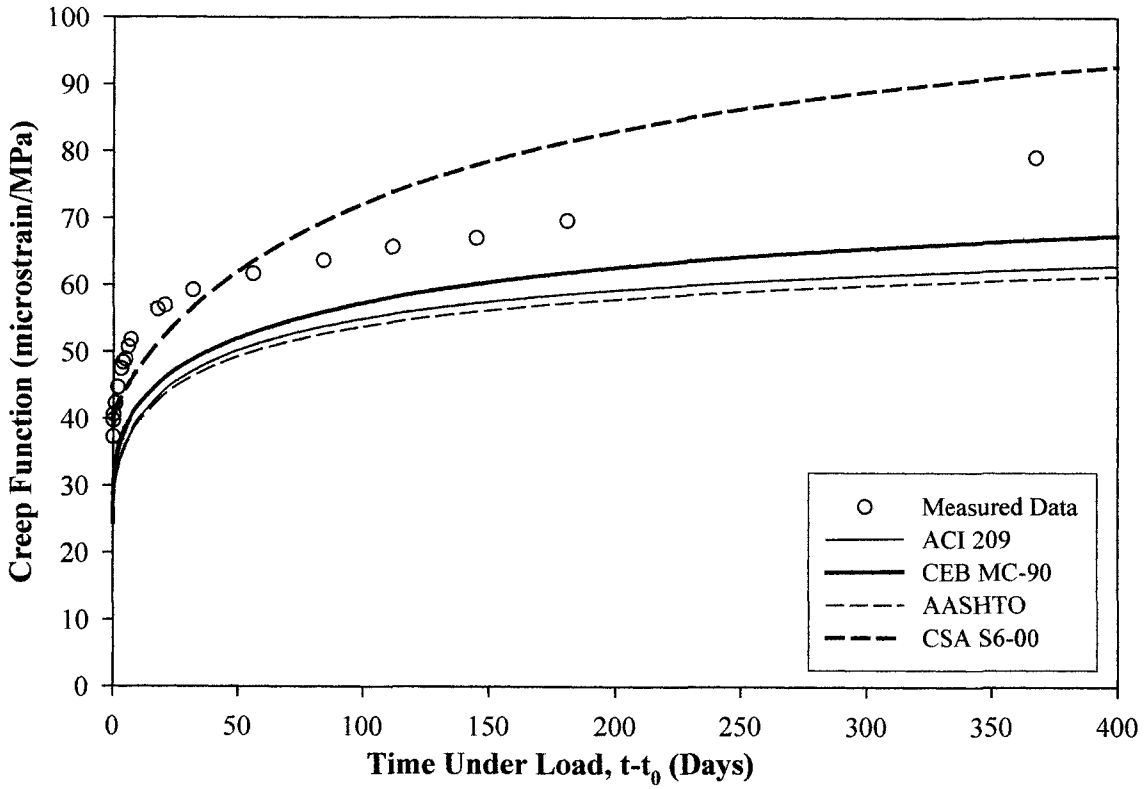

Figure 3.7c: Creep Function for 28 day Age at Loading

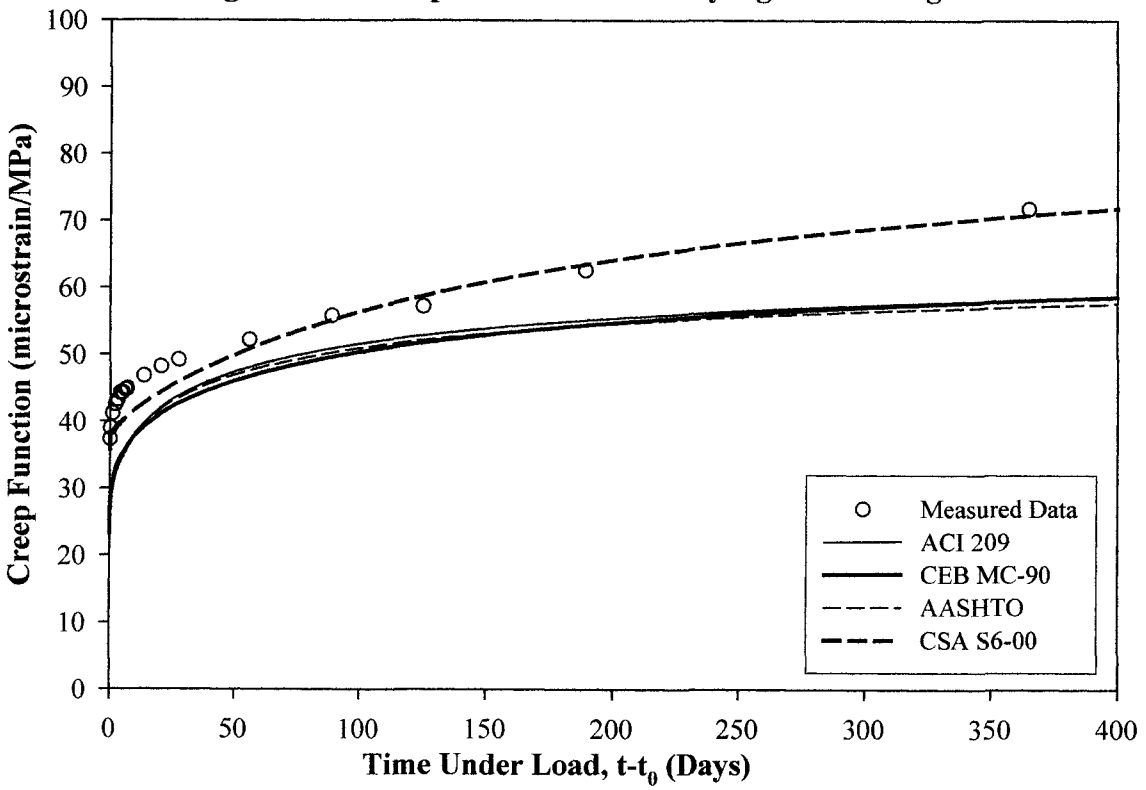

Figure 3.7d: Creep Function for 84 day Age at Loading

Figure 3.7: Creep Functions of Accelerated (Method 1) Cured Cylinders

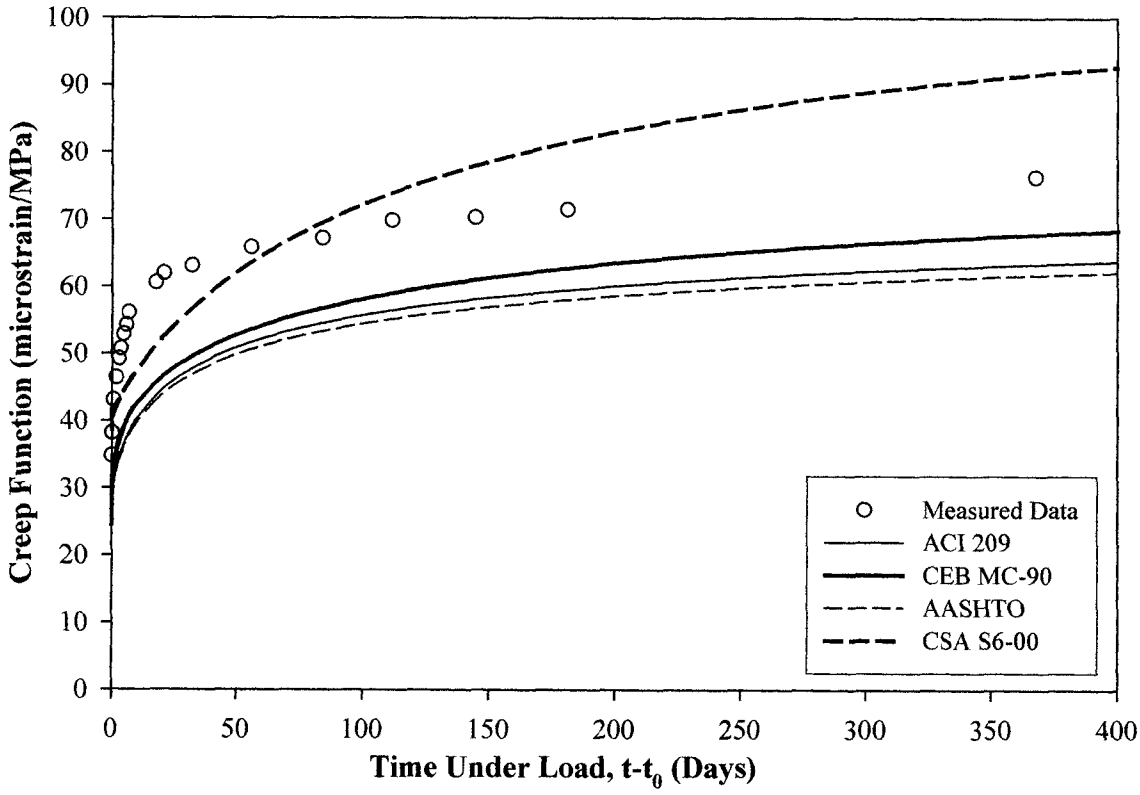

Figure 3.8: Creep Function of Moist (Method 2) Cured Cylinders for 28 day Age at Loading

3.5 Mix-Specific Model Fitting

3.5.1 Criteria for a suitable model template

The third objective of this study is to propose a method to fit laboratory test data to a general model. A set of criteria for an optimal model follows, along with a comparison of the four models thus far considered.

1. The model must be compatible with accepted structural analysis methods.

The four models considered herein, AASHTO, ACI 209, CEB MC-90 and CSA S6-00, are all formulated to allow ease of use in structural analysis.

2. The model must predict all material properties required for analysis and design, regardless if testing was done on that material property.

The second criterion eliminates the AASHTO and CSA S6-00 models, as they do not provide predictive equations for strength gain. For an optimal model, the prediction of strength gain is required because, for one, tensile strength is considered a function of strength gain, and in prestressed concrete design, cracking at the time of prestress transfer can often govern design.

3. The model should provide reasonable predictions if default values are used.

The third criterion would favour the use of either the ACI 209 or CEB MC-90 models, as they are the most consistently accurate models for the prediction of material properties (see Section 3.4). Therefore, the model chosen for fitting should revert to the original code equations when default values are chosen for the fitted parameters.

4. The model must be suited for regression analysis.

The fourth criterion favours the use of the CEB MC-90 over the ACI 209 model. In a generalized format, the ACI 209 model requires non-linear regression for the shrinkage and creep prediction functions, while CEB MC-90 can be linearised and fitted using standard multiple linear regression. It is true that non-linear regression does not take significantly more computing power than linear regression, but, as it will be shown, linear regression has added benefits when considering variability.

3.5.2 Generalised Form of CEB MC-90 Model

The CEB MC-90 format has been adopted for the fitting procedure. Outlined below is the generalised form of this model.

Strength Gain with Time

The following equation is used to describe compressive strength gain with time:

$$f_{cm}(t) = f_{cm} \cdot \exp\left\{\zeta_1\left[1-\left(\frac{28}{t/t_1}\right)^{1/2}\right]\right\} \tag{3.4}$$

where, $f_{cm}(t)$ is the strength gain with time, f_{cm} is the 28 day mean strength and can be predicted from Equation 3.5, t is the age of the concrete as adjusted from Equation 3.12, t_1 is 1 day, and ζ_1 is a fitted parameter.

CEB MC-90 recommends that the mean strength be estimated from the specified strength by the following equation:

$$f'_c = f_{cm} + 8\text{MPa} \tag{3.5}$$

Stiffness

The following equation is used to describe the modulus of elasticity as a function of compressive strength:

$$E_c(f_{cm}) = \left[\frac{f_{cm}(t)}{f_{cm}}\right]^{1/2} \cdot E_{ci} \tag{3.6}$$

where, $E_c(f_{cm})$ is the modulus of elasticity as a function of compressive strength and E_{ci} is the modulus of elasticity at an age of 28 days, and is determined from the following equation:

$$E_{ci} = \zeta_2\left[\frac{f_{cm}}{f_{cmo}}\right]^{1/3} \tag{3.7}$$

where f_{cmo} is 10 MPa, and ζ_2 is a fitted parameter.

Shrinkage

The following equation is used to describe shrinkage:

$$\varepsilon_{cs}(t,t_s)=\zeta_3\left[1-\left(\frac{RH}{RH_o}\right)^3\right]\left[160+10\beta_{sc}\left(9-\frac{f_{cm}}{f_{cmo}}\right)\right]\left[\frac{(t-t_s)/t_1}{350\left(h/h_0\right)^2+(t-t_s)/t_1}\right]^{\zeta_4}\times10^{-6} \tag{3.8}$$

where RH is the relative humidity, RH_0 is 100%, β_{sc} is a factor depending on cement type, and is taken as 5 for normal cement, t_s is the age of concrete at the beginning of shrinkage, ζ_3 and ζ_4 are fitted coefficients, h_0 is 100 mm and h is the notional thickness and is defined as follows:

$$h=\frac{2A_c}{u} \tag{3.9}$$

where A_c is the cross-sectional area and u is the perimeter in contact with the atmosphere.

Creep

The following equation is used to predict the creep coefficient:

$$\phi_{28}(t,t_0)=\zeta_5\left(1+\frac{1-RH/RH_0}{0.46\left(h/h_0\right)^{1/3}}\right)\left(\frac{f_{cmo}}{f_{cm}}\right)^{0.5}\left(\frac{1}{0.1+\left(t_{0,Adj}/t_1\right)^{0.2}}\right)^{\zeta_6}\left(\frac{(t-t_0)/t_1}{\beta_H+(t-t_0)/t_1}\right)^{\zeta_7} \tag{3.10}$$

where $t-t_0$ is the time under load, $t_{0,Adj}$ is the age at loading adjusted according to Equation 3.15, ζ_5, ζ_6 and ζ_7 are the fitted parameters and β_H is defined as follows:

$$\beta_H = 150\left\{1+\left(1.2\frac{RH}{RH_0}\right)^{18}\right\}\frac{h}{h_0}+250 \le 1500 \tag{3.11}$$

Maturity

To account for varying curing regimes, the age of concrete, t, in Equation 3.4 and the age at loading, $t_{0,Adj}$, in Equation 3.10 are adjusted according to Equation 3.12. In the CEB MC-90 model code, the age is also adjusted for different cement types, but these adjustments have no effect when normal type 10 cement is used.

$$t_k = \sum_{i=1}^{n} \Delta t_i \exp\left[13.65 - \frac{4000}{273 + T(\Delta t_i)/T_0}\right] \tag{3.12}$$

where t_k is the temperature adjusted concrete age, T_0 is 1°C, $T(\Delta t_i)$ is the temperature (°C) during the time period Δt_i, and Δt_i is the time (days) where temperature $T(\Delta t_i)$ prevails.

3.5.3 Fitting Procedure

To fit the equations describing strength gain, modulus of elasticity, shrinkage and creep to the measured lab data, multiple linear regression is used. This method is adapted from a similar method used by Ghali et al. (1999). To begin, the equation is put into a linear form:

$$\{y\} = [X]\{\zeta\} + \{e\} \tag{3.13}$$

where $\{y\}$ is a vector containing the measured data, $[X]$ is a matrix of coefficients, $\{\zeta\}$ is a vector containing the parameters which are to be fitted, and $\{e\}$ is a vector representing the residual error. The set of parameters that minimise the sum of the square of the residual error is represented by the vector $\{Z\}$, and is determined by:

$$\{Z\} = \left([X]^T[X]\right)^{-1}[X]^T\{y\} \tag{3.14}$$

Then the best-fit solution is:

$$\{\hat{y}\} = [X]\{Z\} \tag{3.15}$$

Table 3.5 summarises the equations for predicting strength gain, modulus of elasticity, shrinkage and creep in their linear forms.

3.5.4 Model Uncertainty

The model is described by a set of linear equations, with a mean behaviour described by the parameters giving the least-squares solution. However, there is still error in the predictions made using this model. By associating this error to the model, an estimate of the internal uncertainty can be made.

The variance-covariance matrix of the estimated regression parameters, {Z}, is represented by:

$$\sigma^2\left([X]^T[X]\right)^{-1} = \sigma^2\begin{bmatrix} c_{00} & c_{01} & \cdots & c_{0k} \\ c_{10} & c_{11} & \cdots & \cdots \\ \cdots & \cdots & \cdots & \cdots \\ c_{k0} & c_{k1} & \cdots & c_{kk} \end{bmatrix} \tag{3.16}$$

where σ^2 is the population variance and k is the number of degrees of freedom associated with the sum of the squares of the residual. An unbiased estimate of the population estimate is the residual mean square, and is expressed as:

$$s^2 = \frac{\sum_{1=1}^{n} e_i^2}{n-k-1} = \frac{\sum_{1=1}^{n} (y_i - \hat{y}_i)^2}{n-k-1} \tag{3.17}$$

where s^2 is the estimate of the population variance and n is the sample size (the number of test readings).

Table 3.5: Multiple Linear Regression Terms for Fitting Laboratory Data

Property	$\{y\}$	$[X]$	Coefficient a_n	Coefficient b_n	$\{\zeta\}$
Strength Gain Eqn 3.4	$\ln\left[\frac{f_{cm}(t)}{f_{cm}}\right]$	$\begin{bmatrix} a_1 \\ a_2 \\ \cdots \\ a_n \end{bmatrix}$	$1-\left(\frac{28}{t}\right)^{1/2}$		$\{\zeta_1\}$
Modulus of Elasticity Eqn 3.6, 3.7	$E_c(f_{cm})$	$\begin{bmatrix} a_1 \\ a_2 \\ \cdots \\ a_n \end{bmatrix}$	$\left(\frac{f_{cm}(t)}{f_{cm}}\right)^{1/2}\left(\frac{f_{cm}}{f_{cmo}}\right)^{1/3}$		$\{\zeta_2\}$
Shrinkage Eqn 3.8	$\ln[\varepsilon_{cs}(t,t_s)]-\ln\left[1-\left(\frac{RH}{RH_0}\right)^3\right]-\ln\left[160+10\beta_{sc}\left(9-\frac{f_{cm}}{f_{cmo}}\right)\right]$	$\begin{bmatrix} 1 & a_1 \\ 1 & a_2 \\ \cdots & \cdots \\ 1 & a_n \end{bmatrix}$	$\ln\left[\frac{(t-t_s)/t_1}{350\left(\frac{h}{h_0}\right)^2+(t-t_s)/t_1}\right]$		$\begin{Bmatrix} \ln[\zeta_3] \\ \zeta_4 \end{Bmatrix}$
Creep Eqn 3.10	$\ln[\phi_{28}(t,t_0)]-\ln\left[1+\frac{1-RH/RH_0}{0.46\left(h/h_0\right)^{1/3}}\right]-0.5\ln\left[\frac{f_{cm}}{f_{cmo}}\right]$	$\begin{bmatrix} 1 & a_1 & b_1 \\ 1 & a_2 & b_2 \\ \cdots & \cdots & \cdots \\ 1 & a_n & b_n \end{bmatrix}$	$\ln\left[\frac{1}{0.1+\left(t_{0,Adj}/t_1\right)^{0.2}}\right]$	$\ln\left[\frac{(t-t_0)/t_1}{\beta_H+(t-t_0)/t_1}\right]$	$\begin{Bmatrix} \ln[\zeta_5] \\ \zeta_6 \\ \zeta_7 \end{Bmatrix}$

The variance of the fitted parameters can then be directly determined by multiplying the estimate of the population variance by the associated coefficient from the variance-covariance matrix:

$$\sigma_{Zi}^2 = c_{ii} s^2 \tag{3.18}$$

As well, a confidence interval on the estimate $\{\hat{y}\}$ can be created. For any particular estimate, $\hat{y}_j$, a confidence interval of $(1-\alpha)100\%$ can be created by adding and subtracting the product of the t score and the standard error from the estimate.

$$\hat{y}_j \pm t_{\alpha/2} s \sqrt{\{x_j\}^T \left([X]^T [X]\right)^{-1} \{x_j\}} \tag{3.19}$$

where $t_{\alpha/2}$ is the t score, and is a function of α and the number of degrees of freedom of the data set. The vector $\{x_j\}^T$ takes the coefficients from a row of [X] (refer to Table 3.5), but with the coefficient terms calculated from the data used to make the estimate $\hat{y}_j$. For example, in creating a confidence interval on a creep coefficient, $\{x_j\}^T=\{1, a_j, b_j\}$.

3.5.5 Mix-Specific Model

The procedure outlined above was performed on the measured laboratory data. To account for maturity of concrete, the half-day of steam curing was taken equivalent to 3 days of moist curing. This was determined through the use of Equation 3.12 and Figure 3.2. Table 3.6 summarises the results from the data fitting procedure performed on the laboratory data from accelerated-cured samples only.

Table 3.6: Material Model Parameter Summary

Mechanical Property	Parameter ζ_i	Default (Code) Value	Fitted Value	Coefficient of Variation
Strength	ζ_1	0.25	0.11	6.5%
Stiffness	ζ_2	21500	15370	0.6%
Shrinkage	ζ_3	1.55	2.96	1.8%
	ζ_4	0.5	0.38	1.5%
Creep	ζ_5	5.3	2.74	3.6%
	ζ_6	1.0	0.83	5.8%
	ζ_7	0.3	0.27	1.9%

The variance of the above model works well for all properties except strength gain. This is due to the fact that the [X] matrix becomes singular for an age of 28 days. The model assumes a known value for the 28-day compressive strength, and results in an estimated zero variance at this age. The calculated variance of the compressive strength describes the internal error associated with the model, but not the error associated with a variable 28-day strength. Figure 3.9 shows the strength gain as predicted using Model A, and a standard deviation of 1.5 MPa for the 28-day compressive strength, while Figure 3.10 shows the modulus of elasticity as predicted using Model A.

As mention, CEB MC-90 provides cut-off values of 10 and 5 percent for shrinkage strain and the creep coefficient, which is similar to 90 and 95 percent confidence intervals. Figures 3.11 and 3.12 show the prediction of shrinkage strain and prediction of the creep function using Model A and CEB MC-90 with the 95% confidence interval for Model A and 5% cut-off value CEB MC-90. For prediction of the shrinkage strain, the set where measurements began at 0.43 days is shown, while for prediction of the creep function, only the 1.3 day age at loading set is shown, and variance in the stiffness is ignored.

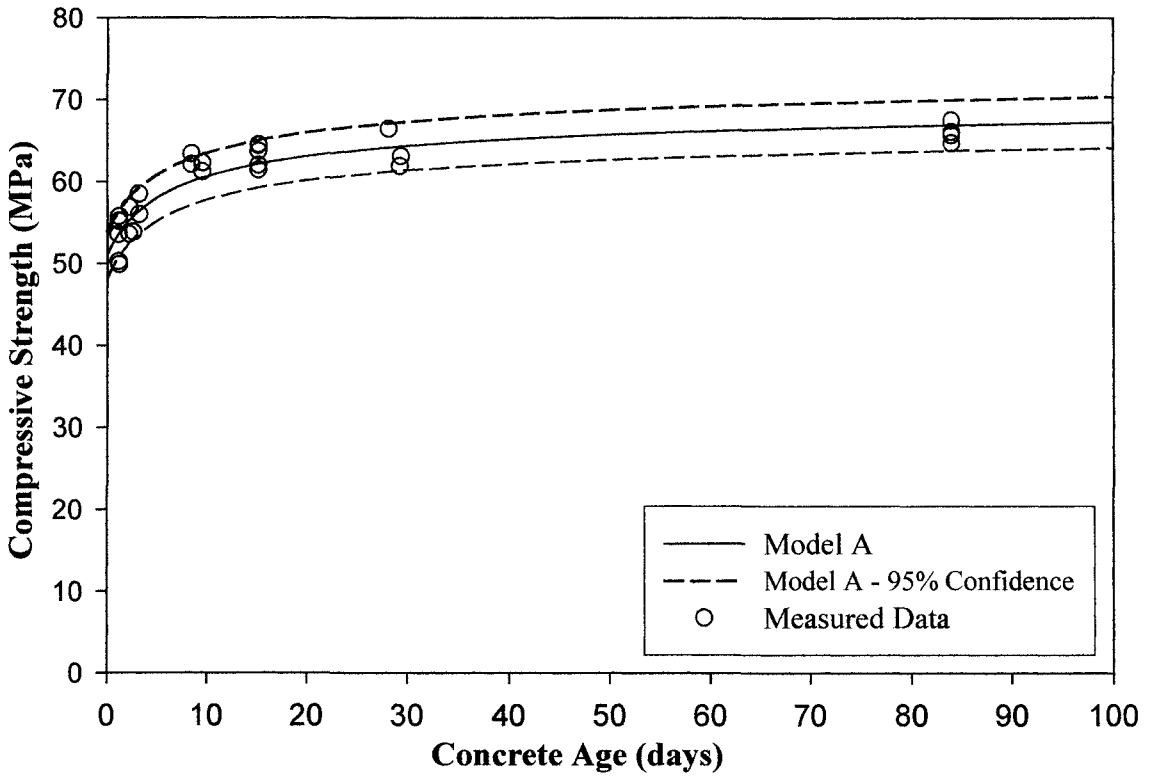

Figure 3.9: Model A Prediction and Confidence Intervals - Strength Gain with Time

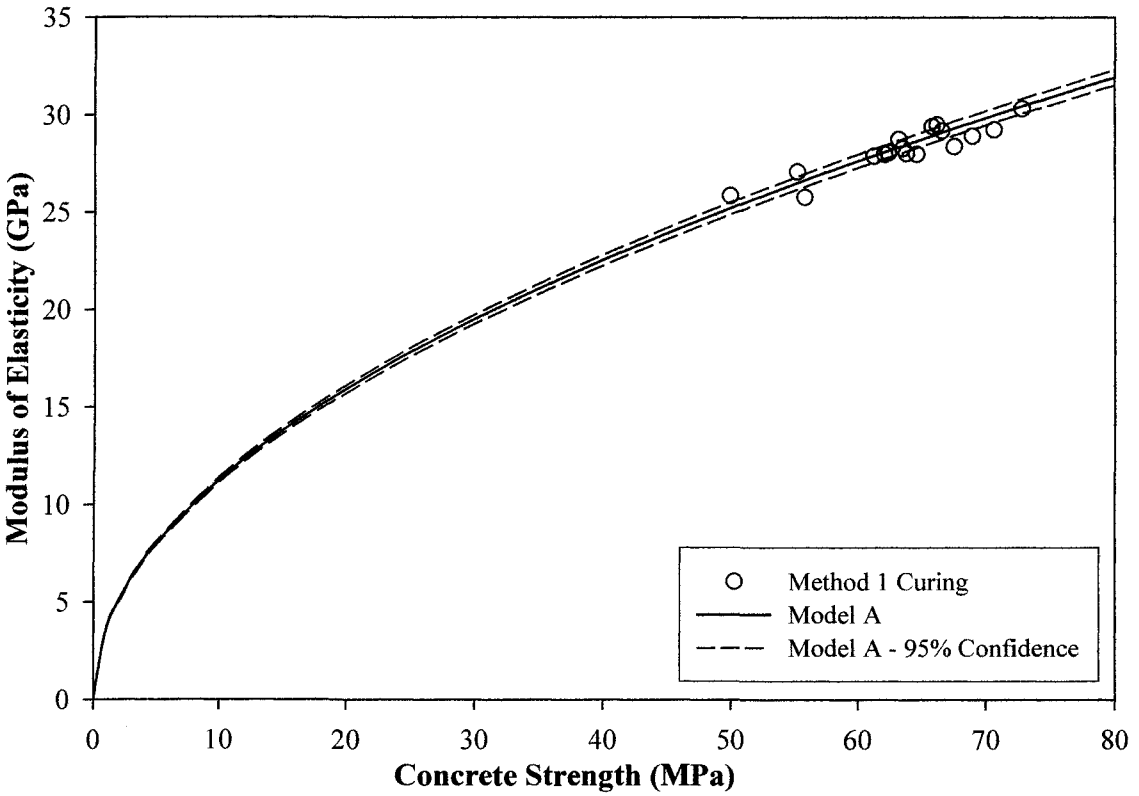

Figure 3.10: Model A Prediction and Confidence Intervals – Modulus of Elasticity

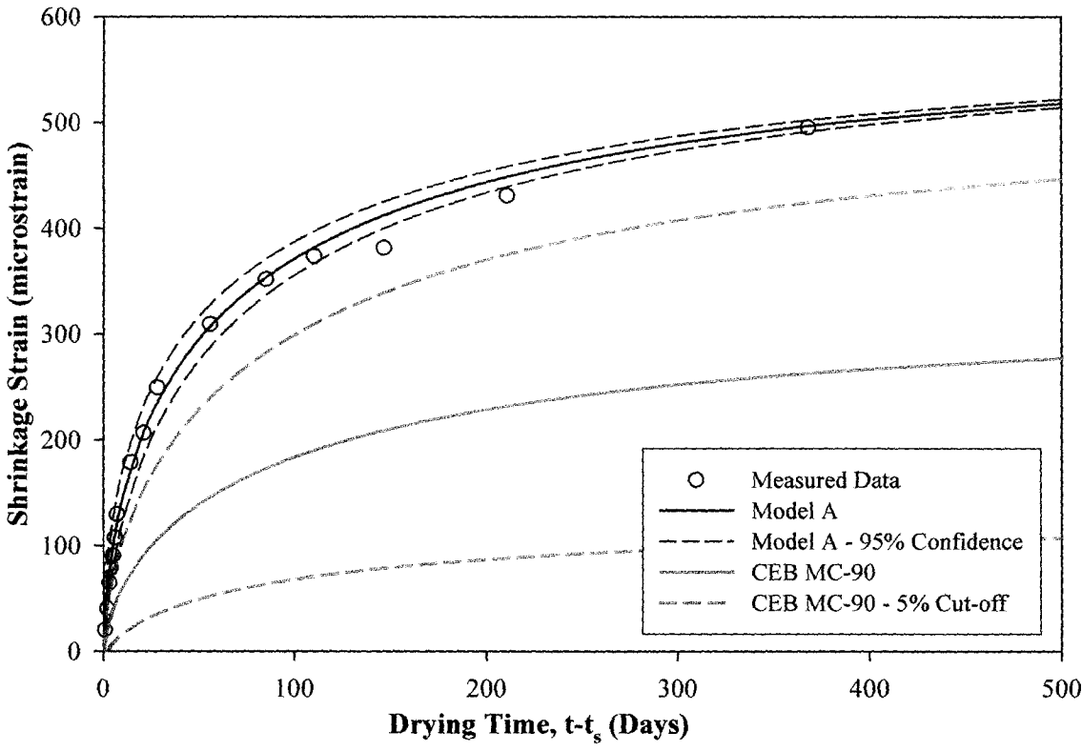

Figure 3.11: Model A and CEB MC-90 Predictions and Confidence Intervals for Shrinkage Strain

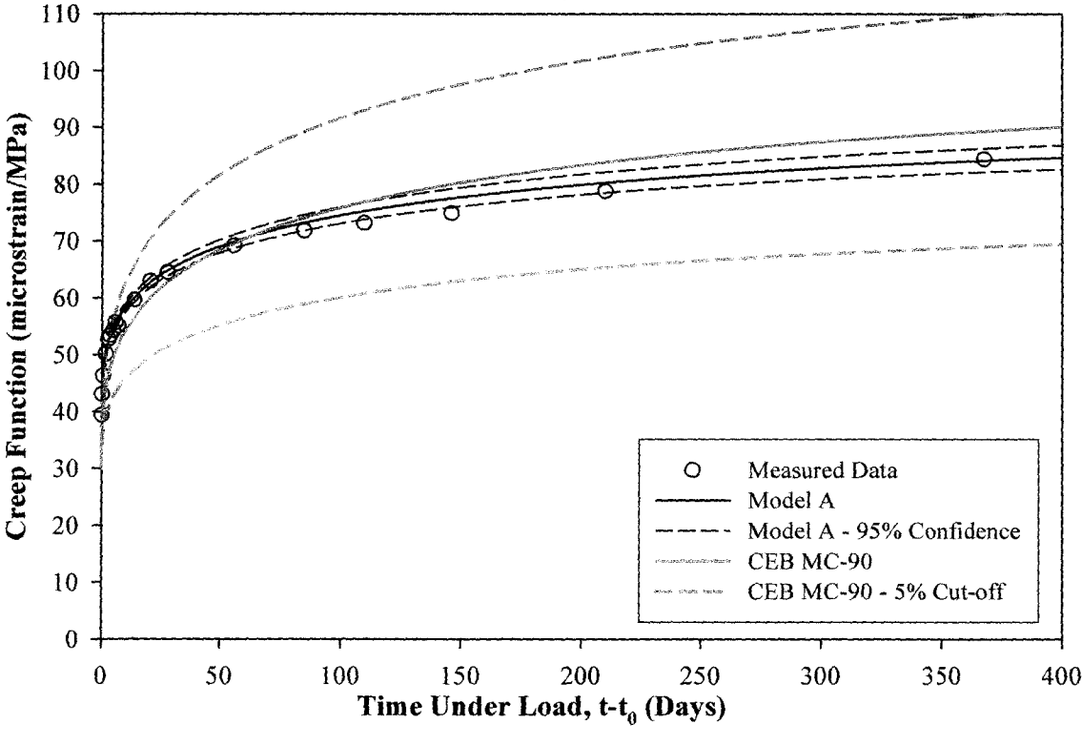

Figure 3.12: Model A and CEB MC-90 Predictions and Confidence Intervals for Creep Function, 1.3 day Age at Loading

3.6 Discussion of Results

Strength gain with time is shown in Figure 3.3 and predicted using ACI 209 and CEB MC-90. Both models provide reasonable predictions for both the accelerated and moist cured samples. In both cases ACI 209 underestimates the strength of the mix. CEB MC-90 overestimates long-term strength for accelerated cured samples, and gives an accurate prediction for moist cured samples. Neither AASHTO nor CSA S6-00 provide predictive equations for strength gain with time.

Modulus of elasticity predictions are shown in Figure 3.4. Here it is seen that CSA S6-00 provides the best prediction of stiffness, while AASHTO, ACI 209 and CEB MC-90 all overestimate the stiffness by between 30 and 40 percent. One explanation is that the CSA S6-00 formulation has been fitted to Canadian test data. Thus, if Canadian concrete tends to be less stiff than American or European concrete, CSA S6-00 would be more likely to account for this.

Shrinkage predictions are shown in Figure 3.5. For both accelerated cured samples and moist cured samples ACI 209 provides the best predictions. The measured data also shows that for this mix, the measured shrinkages are greater than the predicted using either CEB MC-90 or CSA S6-00, while AASHTO highly overestimates the magnitude of shrinkage strains.

Creep effects are shown in terms of the creep function, which describes the total load-related strain. For ages of loading less than 28 days the predictions from the different models are more spread, while for predictions greater than and equal to an age of loading of 28 days the predictions are more closely spaced. For early ages of loading, CEB MC-90 gives the best predictions while CSA S6-00 highly overestimates the response and AASHTO underestimates response. But for ages of loading of 28 days and 84 days, CSA S6-00 gives the best predictions. It can also be seen that the shape function used to describe creep with time seems generally correct for AASHTO, ACI 209, and CEB MC-

90, while the shape function used by CSA S6-00 does not fit the shape of the measured data well. The most consistently accurate predictions are obtained using CEB MC-90.

Figures 3.9 through 3.12 show the predictions made using the fitted model, Model A. It is evident that this model provides accurate descriptions of behaviour, as would be expected by the fitting procedure used.

Figures 3.9 and 3.10 show confidence intervals on the predictions of strength gain and modulus of elasticity. The spread of the measured data requires a larger interval to provide 95 percent confidence on strength measurements than for stiffness measurements. This indicates that either the equation predicting modulus of elasticity describes the observed test results better than the equation predicting strength gain or that that there is less inherent variation in the test results for modulus of elasticity than for strength gain. These results suggest that predictions of the modulus of elasticity can be confidently extrapolated from few experimental test results by fitting these results to the general model presented. A minimum of three tests is recommended to identify outliers, but only one age of testing is required and the test results can be averaged, because the equation describing modulus of elasticity has only one parameter for fitting. The one parameter is sufficient for characterising the modulus of elasticity.

The prediction of strength gain with time cannot be accurately predicted from few test results. The experimental results obtained suggest that tests should be conducted at more than one age, and that multiple tests be conducted at each age to the increase confidence of the mean strength. For the general model presented, two parameters are required for characterising strength gain with time.

The CEB MC-90 model code provides 10 and 5 percent cut-off values for shrinkage and creep based on estimated coefficients of variation from the measured data that the models were based upon. Figures 3.11 and 3.12 show the CEB MC-90 predictions with 5 percent cut-off ranges along with the predictions made using Model A. Figure 3.11 shows that even with a large interval on probable behaviour, the actual behaviour is still

missed. This is compared to the confidence of Model A, which is significantly better. Figure 3.12 shows that while CEB MC-90 can fairly accurately predict the creep function for the mix, its prediction has little confidence. It can be seen that probabilistic analyses using CEB MC-90 would result in overly conservative behaviours in regards to load-related strains, and non-conservative estimates of shrinkage. The benefit of using Model A would be an increase in confidence in the design.

One problem of using the fitting procedure as indicated is that all data points receive the same weighting of importance. Because the testing procedures for creep and shrinkage require many reading in the early ages, decreasing with time, the early age behaviour actually gets more weighting than the long-term behaviour. If this is of concern, judgment should be used in either using a more even sampling time during testing, or selectively removing recorded data to make the existent data set more evenly distributed.

3.7 Summary and Conclusions

A comprehensive material testing program was conducted on a high-performance concrete mix to determine its mechanical properties, specifically strength, stiffness, shrinkage and creep properties. AASHTO, ACI 209, CEB MC-90 and CSA S6-00 were used to predict mechanical properties. As well, a material model was fit to the measured data, and its variability was assessed. From the results of the experimental program and analyses, the following conclusions can be drawn:

1. The CEB MC-90 model code provided the best prediction of concrete behaviour; ACI 209 provided the second best prediction of behaviour. Both codes provide complete descriptions of behaviour, including strength gain with time, which is necessary to accurately assess serviceability limits for structures exposed to early age loadings.

2. An accurate prediction of the modulus of elasticity can be confidently extrapolated from minimal test results. This suggests that single-age testing of stiffness is adequate in

characterising the concrete mix stiffness. This is opposed to the compressive strength of the concrete mix where multiple ages of testing are required to characterise behaviour.

3. The method proposed to fit measured lab data to a material model was simple, straightforward, and provides an accurate description of the concrete's mechanical behaviour. The model chosen can be easily incorporated into structural design, and can also provide confidence intervals on the predicted behaviour.

4. In the case that a probabilistic analysis is warranted, the certainty in predictions of the fitted model is much greater than that of CEB MC-90. The range of extreme behaviour for CEB MC-90 was nearly 10 times greater than that of the fitted model, Model A when predicting creep, and was over 20 times greater when predicting shrinkage.

3.8 References

AASHTO. 1998. *LRFD Bridge Design Specifications - Second Edition*, American Association of State Highway and Transportation Officials, Washington, D.C.

ACI Committee 209. 1997. *Prediction of Creep, Shrinkage, and Temperature Effects in Concrete Structures, (ACI 209R-92),* American Concrete Institute, Farmington Hills, MI.

ASTM C 39/C39M-01. 2002. *Standard Test Method for Compressive Strength of Cylindrical Concrete Specimens*, American Society for Testing and Materials, West Conshohoken, PA

ASTM C 469-94e1. 2002. *Standard Test Method for Static Modulus of Elasticity and Poisson's Ratio of Concrete in Compression*, American Society for Testing and Materials, West Conshohoken, PA

ASTM C 512-87. 1994. *Standard Test Method for Creep of Concrete in Compression*, American Society for Testing and Materials, Philadelphia, PA

Comité Euro-International du Béton. 1993. *CEB-FIP Model Code 1990*, Redwood Books, Trowbridge, Great Britain.

CSA. 2000. *S6-00 Canadian Highway Bridge Design Code*, CSA International, Toronto, Ontario, Canada.

Ghali, A. Megally, S. and Azarnejad, A. 1999. *Monitoring of Concrete Creep and Shrinkage of the Confederation Bridge*, Annual Conference of the Canadian Society for Civil Engineers, June 2-5, Regina, Saskatchewan, Canada.

Predicting the Time-Dependent Deformations of Prestressed Elements A Case Study

4.1 Introduction

Fully continuous medium span concrete bridges are usually governed by serviceability criteria rather than ultimate limit states. These serviceability criteria are deflections and crack control. The prediction of deflections requires an accurate estimate of the internal strain distribution while the control of crack formation requires an estimate of the internal stress distribution in the concrete. However, due to creep, shrinkage and steel relaxation, the results of analysis predictions become dependent on the age of the concrete, the age of the structure, and the load history.

The prediction of time-dependent response requires two components. The first is a material model to describe the time-dependent properties and the second is an analysis capable of incorporating the material model. Material models may be taken directly from codes or developed from extensive material testing, while analysis methods vary from the approximate to the highly refined.

A case study was performed to measure the behaviour of a fully continuous highway overpass. Two precast, prestressed girders were instrumented and monitored for strains and deflections from fabrication to service. To determine the behaviour of the concrete used in the girders, laboratory tests were conducted to measure compressive strength, modulus of elasticity, creep and shrinkage.

There are three objectives to this chapter. The first is to present, in detail, two structural analysis methodologies capable of incorporating the time-dependent properties of concrete and prestressing steel. As well, it is shown how to apply these methods to changes in loading conditions, changes in boundary conditions, and changes in sectional properties.

The second objective of this chapter is to determine how changing the structural analysis methodology affects the accuracy of predicted behaviour.

The third is to investigate how the material model chosen to describe the concrete mechanical properties affects the prediction of time-dependent behaviour.

4.2 Experimental Work

In September 2003, an instrumentation program began to measure strain distributions and vertical deflections on two prestressed girders used in the 130th Avenue and Deerfoot Trail Overpass in Calgary Alberta, Canada. The girders were monitored from the time of fabrication until after longitudinal post-tensioning. Also, samples of the concrete mix used were obtained for a material testing program.

4.2.1 Structure Description

The overpass chosen for study was designed to be completely continuous in service. Figure 4.1 shows the profile of the overpass and a typical section. A total of 12 precast girders were fabricated for this bridge. The construction sequence of the overpass is summarized as follows: 1) Erect pre-cast girders on piers (2 Spans), 2) Place deck and

diaphragms to create continuity, 3) Post-tension longitudinally, 4) Make integral bridge/abutment connection.

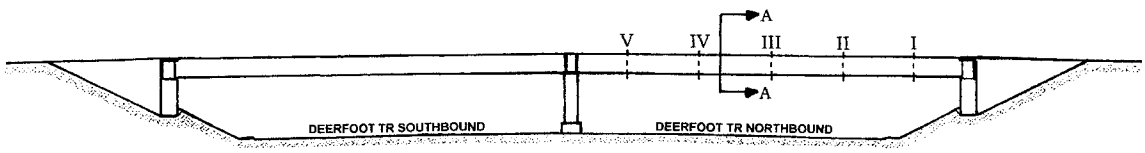

(a) Overpass Profile and Locations of Instrumented Stations

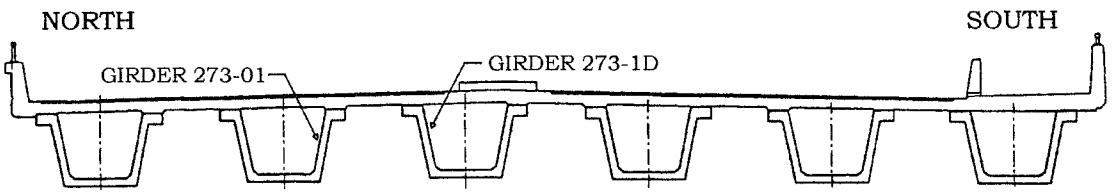

(b) Section A-A of Overpass and Instrumented Girders

Figure 4. 1: 130th Avenue and Deerfoot Trail Overpass

The girders are 38 metres long, 1.65 metres deep and cast with a high-performance concrete. Each is prestressed with 56 - 15.2 mm low-relaxation strands (tensile strength, f_{pu} = 1860 MPa) and contains a combination of welded-wire mesh and deformed bars for passive reinforcement. To avoid cracking at release, some of the prestressing strands are debonded.

The deck is 225 mm thick and has a tributary width of 4250 mm for the interior girders. A normal concrete mix is used with deformed bars for passive reinforcement. The haunch depth varies, but on average is taken as 40 mm. The deck also has a 2% slope, which was not considered in the model.

Figure 4.2 shows a typical girder and deck cross-section, while Table 4.1 lists sectional and material properties of the girder and deck for the concrete, the steel reinforcement and the prestressed reinforcement.

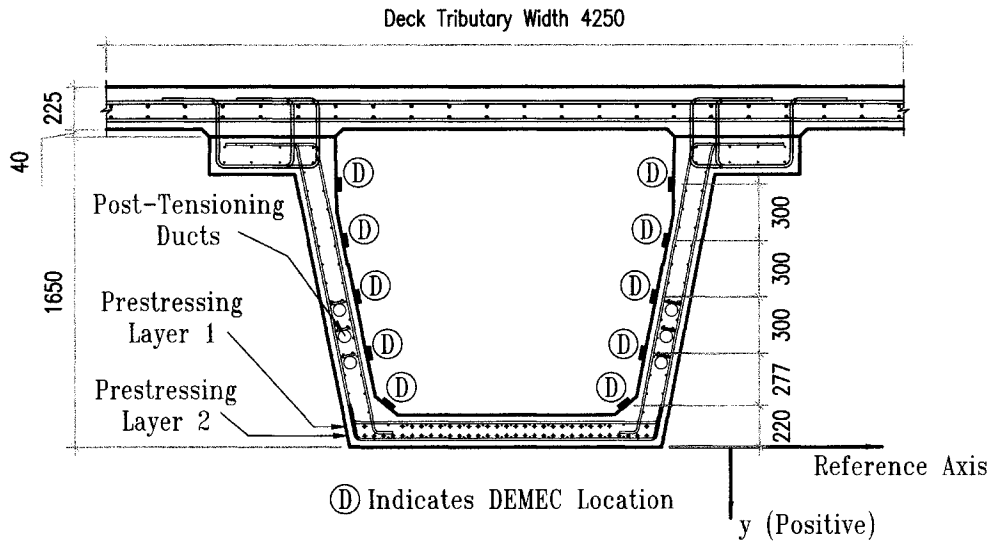

Figure 4.2: Girder and Deck Cross-Section

Table 4.1: Girder and Deck Sectional and Material Properties

	Part	A (mm^2)	*B (mm^3)	*I (mm^4)	**y (mm)	Strength (MPa)	E (MPa)	Number of Strands	Debonded At 4500mm	Debonded At 9000mm
GIRDER	Concrete	1.03×10^6	-823×10^6	1.02×10^{12}	-802	$f'_c = 60$	Chapter 3			
	Nonprestressed Reinforcement	8.72×10^3	-8.25×10^6	10.7×10^9	-946	$f_y = 400$	200×10^3			
	Prestressed Steel Layer 1	3.50×10^3	-385×10^3	65.5×10^3	-110	$f_{pu} = 1650$	190×10^3	25	2	7
	Prestressed Steel Layer 2	4.34×10^3	-260×10^3	81.2×10^3	-60	$f_{pu} = 1650$	190×10^3	31	8	9
DECK	Concrete	948×10^3	-1.71×10^9	3.08×10^{12}	-1803	$f'_c = 40$	Chapter 3			
	Nonprestressed Reinforcement	8.50×10^3	-15.2×10^6	27.8×10^9	-1783	$f_y = 400$	200×10^3			

* Calculated about reference axis in Figure 4.2 **y indicates distance from centroid of component to reference axis

After the deck and diaphragm reach the specified strength, the system is longitudinally post-tensioned. The tendon profile is parabolic with a single inflection point, and is horizontal at the midpoint of the centre diaphragm, as depicted in Figure 4.3. Each tendon contains 9 strands of the same size and strength as the prestressing strands. The jacking stress is 0.8 f_{pu}, which is equivalent to 1875 kN per tendon. Jacking is done from both ends simultaneously.

In design, the load history would be based upon an optimized construction schedule and a conservative construction schedule giving an envelope on possible behaviour. For the purposes of this testing program, the actual load history was measured, and is summarised in Table 4.2. The effect of the integral abutment was not considered because no measurements were made in this phase construction

Table 4.2: Girder Load History

Event	Description	Girder Age (days)		Construction Phase	Support Reactions*			
					Girder 273-01		Girder 273-1D	
		Girder 273-01	Girder 273-1D		a (mm)	b (mm)	a (mm)	b (mm)
t_0	Concrete Cast	0	0	A	N/A	N/A	N/A	N/A
t_1	Prestress Transfer	1	1	B	0	0	0	0
t_2	Moved to Storage	2.75	1.1	C	1000	1000	1000	1000
t_3	Loaded on Truck	144	138	D	1700	2300	1900	3000
t_4	Erected On-Site	147	141	E	0	0	0	0
t_5	Deck and Diaphragm Pour	225	220	F	0	0	0	0
t_6	Longitudinally Post-Tensioned	231	226	G	0	0	0	0

* Location of Support Reactions

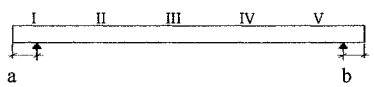

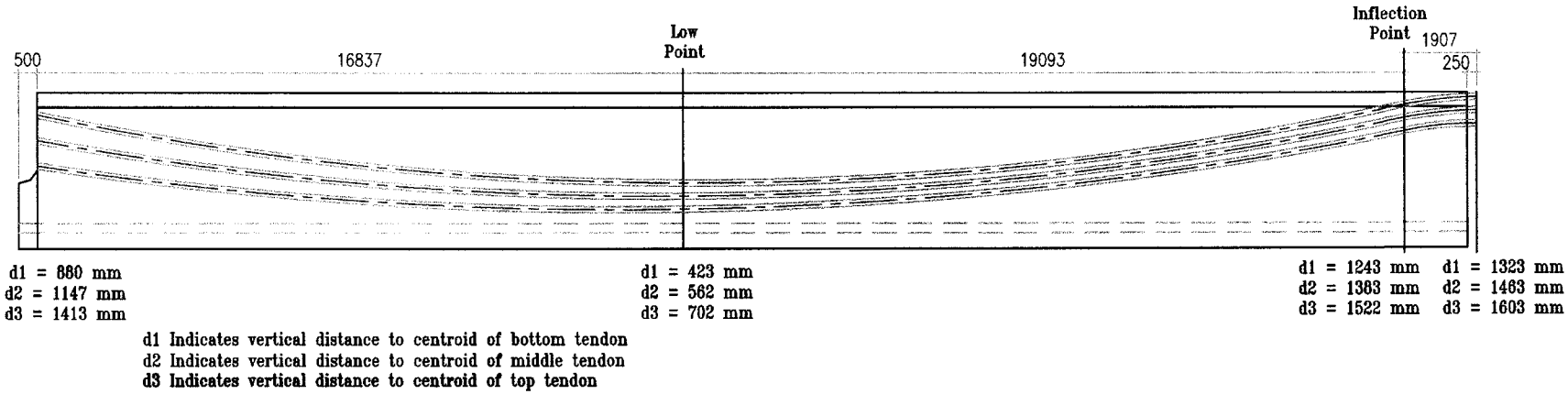

Figure 4.3: Post-Tensioning Profile

Concrete Mix Testing

The mechanical properties of the concrete mix used in the fabrication of the overpass girders were experimentally found. The characterisation program is the subject of Chapter 3. The purpose of Chapter 3 is to assess the ability of different models to predict the mechanical properties of the concrete mix used, and as well to provide a tuned model that can provide an accurate prediction of the concrete's mechanical behaviour. The tuned model is referred to as Model A, and is considered the best representation of the concrete mix's behaviour.

The properties of the deck concrete were not tested. The specified design strength of the girder concrete and deck concrete is 60 MPa and 45 MPa respectively.

4.2.2 Instrumentation, Measurements and Sampling Times

The instrumentation plan focused on monitoring curvatures. Five sets of DEMECs were placed on each web of the girder, as shown in Figure 4.2. Five sections (marked I through V in Figure 1) were instrumented with DEMECs on each girder.

DEMECs are used to measure strain, and were positioned to measure longitudinal strains. DEMEC readings were performed a minimum of two times per set to ensure reproducibility of the measured value, and were typically performed three times. This was to done to reduce the probability of clerical errors and increase the confidence in mean values.

Plane sections theory was assumed, and is confirmed from section strain readings. This allowed a curvature to be calculated at each section for each measurement period. The curvature at a section was estimated from the 10 readings by finding the best-fit plane section. Figure 4.4 shows the measured strain distributions and the best-fit plane section at station III of Girder 273-01 immediately after prestress transfer. Compressive strains are taken as negative.

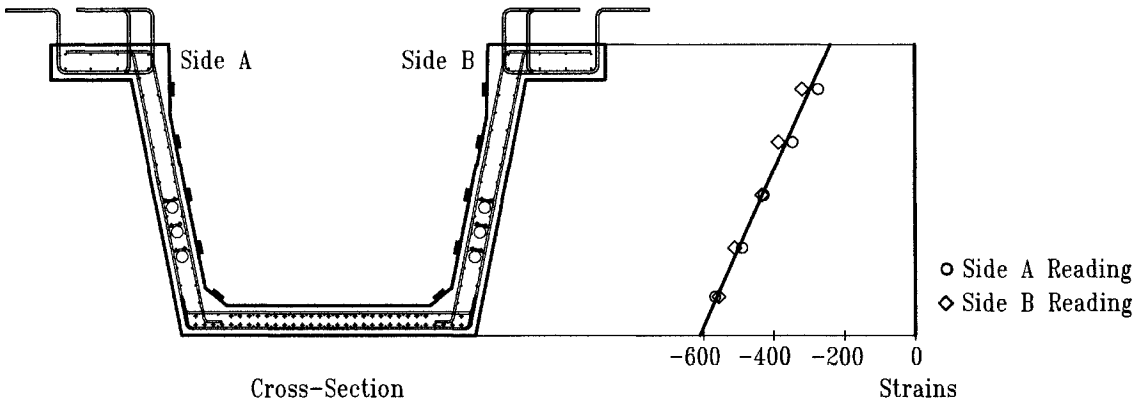

Figure 4.4: Strain Distribution of Station III of Girder 273-01 after Prestress Transfer

As a secondary measurement, deflections of the girders were measured using a survey rod and level.

Measurements were taken periodically through the monitoring time of the structure. A minimum of one set of measurements was taken at each construction stage, except between on-site erection and deck pour. Measurements taken and sampling times are summarised in Table 4.3. To reduce thermal effects, measurements were taken at times when thermal gradients were expected to be minimal. In most cases, measurements were made in the morning and on relatively overcast days.

Table 4.3: Sampling Times

Measurement Set	Girder Age (days)		Construction Phase	Measurement Taken	
	Girder 273-01	Girder 271-1D		Strains	Camber
Zero Reading	0.9	0.9	A	Yes	No
1	1	1	B	Yes	Yes
2	24	19	C	Yes	No
3	67	62	C	Yes	Yes
4	95	90	C	Yes	Yes
5	145	140	D	Yes	Yes
6	228	223	F	Yes	No
7	275	271	G	Yes	Yes

4.3 Methods of Analysis

Two methodologies are used to predict the sectional responses with time. Both are accepted structural analysis methods, and are presented in a format so that differences may be noted. In both cases, plane-sections theory for uncracked elements provides the compatibility requirements. The differences arise in how the time-dependent effects of creep, shrinkage and prestress loss are included.

4.3.1 Elastic Response of a Section

The section forces considered are the normal force N acting at the reference point and the bending moment M, taken with respect to the reference axis. A positive normal force causes tension and a positive bending moment causes tension on the bottom fibre. The resulting strain distribution is considered positive, as illustrated in Figure 4.5.

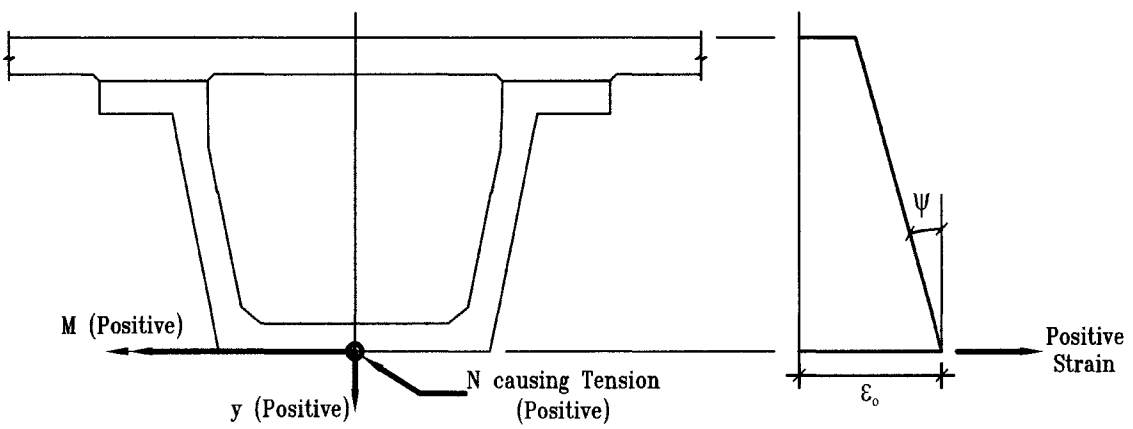

Figure 4.5: Positive Sign Convention

The first set of section forces considered are those due to self-weight, and are termed N_0 and M_0. In the case that the beam is horizontal and statically determinate, the self-weight will not produce an axial load.

The next set of forces to consider is due to the prestressing. Since the prestressing strands are located in one or more layers, it is convenient to define a prestressing force, P_j, for each layer, j (Note, the notation used herein does not represent standard indicial

summation notation typically associated with the subscripts used). The prestressing strands remain linear-elastic through the stressing process, and so the force P_j can be expressed as:

$$P_j = n_j A_{ps} E_{ps} \varepsilon_j \tag{4.1}$$

where n_j is the number of strands in layer j, A_{ps} is the area of one strand, E_{ps} is the elastic modulus of the prestressing and ε_j is the strain in the prestressing strand of layer j.

For the elastic case with only self-weight and prestress acting, the section forces can be written as:

$$\begin{Bmatrix} N \\ M \end{Bmatrix} = \begin{Bmatrix} N_0 \\ M_0 \end{Bmatrix} + \begin{Bmatrix} N \\ M \end{Bmatrix}_{prestress} \tag{4.2}$$

where,

$$\begin{Bmatrix} N \\ M \end{Bmatrix}_{prestress} = \begin{Bmatrix} -\sum P_j \\ -\sum P_j y_{psj} \end{Bmatrix} \tag{4.3}$$

and y_{psj} is the distance to the centroid of the prestressing force for layer j.

The response of a section to the loading defined by Equations 4.1 to 4.3 can be described by its strain distribution. For a plane section the strain distribution is linear, and herein is described by the strain at the reference axis, ε_o, and curvature, ψ. The strain distribution for the section is calculated as:

$$\varepsilon = \varepsilon_0 + \psi y \tag{4.4}$$

while the strain in the prestressing layer j is calculated as:

$$\varepsilon_j = \varepsilon_{psj} + \varepsilon_0 + \psi y_{psj} \tag{4.5}$$

Then, for a section under a normal axial force, N and moment M, the elastic response at time t is given by:

$$\begin{Bmatrix} \varepsilon_0 \\ \psi \end{Bmatrix} = \frac{1}{E_{ref}\left(\tilde{A}\tilde{I} - \tilde{B}^2\right)} \begin{bmatrix} \tilde{I} & -\tilde{B} \\ -\tilde{B} & \tilde{A} \end{bmatrix} \begin{Bmatrix} N \\ M \end{Bmatrix} \tag{4.6}$$

where $\tilde{A}$, $\tilde{B}$ and $\tilde{I}$ are the transformed sectional properties calculated with respect to the reference modulus, E_{ref}. In general the concrete's modulus is taken as the reference modulus. The solution to Equation 4.6 requires iteration until the strain compatibility defined by Equations 4.4 and 4.5 is met.

4.3.2 Time-Dependent Response

The response of prestressed concrete sections is time-dependent because properties of the materials used vary with time. Specifically, concrete under a sustained load will experience creep, concrete exposed to a drying environment will shrink, and prestressed steel under a sustained tensile load will relax. The behaviour of these phenomena are complex and non-linear in nature. However, in general, the use of linear approximations results in little loss of accuracy, and the added complexity of solving non-linear systems is rarely warranted. This is evident in design code development, where linear material models are nearly always used.

For concrete, creep strains are assumed to be linearly related to stress for stress levels in the range of 0.5 f_{cm} where f_{cm} is the mean concrete strength. This assumption of linearity allows the principle of superposition to be used, and a constitutive relationship can be written as:

$$\varepsilon_c(t) = \sigma_c(t_i)\cdot\frac{1+\phi(t,t_i)}{E_c(t_i)} + \int_0^{\Delta\sigma_c(t)} \frac{1+\phi(t,\tau)}{E_c(\tau)} d\sigma_c(\tau) + \varepsilon_{cs}(t,t_s) \tag{4.7}$$

The variation in stress with time and the resultant strain are shown graphically in Figure 4.6. Here, $\varepsilon_c(t)$ is the concrete strain at time t, $\sigma_c(t_i)$ and $\sigma_c(\tau)$ are the stresses at times t_i and τ respectively, $\phi(t,t_i)$ and $\phi(t,\tau)$ are the creep coefficients at time t for ages of loading of t_i and τ respectively, $E_c(t_i)$ and $E_c(\tau)$ are the concrete modulus of elasticity at ages t_i and τ respectively, and $\varepsilon_{cs}(t,t_s)$ is the shrinkage strain at time t where t_s is the time shrinkage begins. Here the creep coefficient is defined as the ratio of creep strain to initial elastic strain, which is consistent with the definition from ACI 209.

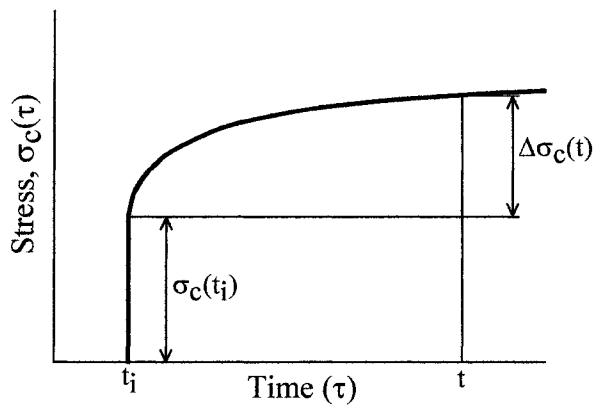

Figure 4.6a Applied Stress Varying in Time

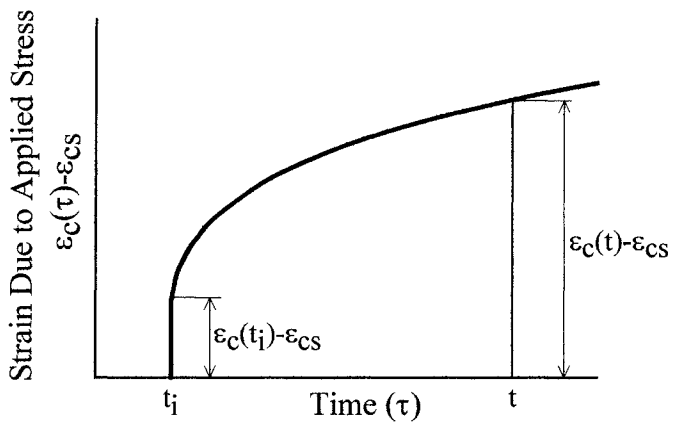

Figure 4.6b Stress Related Strain as a Function of Time

Figure 4.6 Stress and Strain of a Concrete Member in Uniaxial Compression

In Equation 4.7, $\Delta\sigma_c(t)$ is a stress increment (or decrement) which begins at zero at time t_i and gradually increases to it's full value at time t. A simplified solution to the above equation was originally proposed by Trost (1967) and formalised by Bazant (1972), where the introduction of the aging coefficient, χ, replaces the integral with an algebraic expression. The aging coefficient is a function of both the stress history and concrete aging properties, but can generally be taken constant with little loss in accuracy.

$$\varepsilon_c(t) = \sigma_c(t_i)\cdot\frac{1+\phi(t,t_i)}{E_c(t_i)} + \Delta\sigma_c(t)\cdot\frac{1+\chi\phi(t,t_i)}{E_c(t_i)} + \varepsilon_{cs}(t,t_s) \tag{4.8}$$

The benefit of the aging coefficient is that the deformation of concrete can be written in a linear system of equations, even if stresses are applied or removed gradually. In essence, the varying stress is treated as if its full magnitude was applied at time t_i, but its effects are reduced by the aging coefficient to account for its gradual development. The aging coefficient assumes the rate at which stress is applied.

4.3.2.1 Prestress Loss

Losses in the prestress levels can be classified as immediate and long-term. Immediate losses include everything up to and including transfer, while long-term losses occur thereafter.

With prestressed concrete, immediate losses include anchor seating, shortening of the stressing bed, thermal relaxation due to differences in temperature between the time of stressing and transfer, and intrinsic relaxation prior to transfer. These are normally accounted for by the fabricator to ensure a specified stress level in the strands at transfer. At transfer shortening of the girder results in elastic shortening of the strands. Ensuring that equilibrium and the compatibility requirements of Equations 4.4 and 4.5 are met includes the effect of elastic prestress loss, assuming linear-elastic behaviour of the prestressing strand.

Following transfer, concrete creep and shrinkage and strand relaxation result in further prestress loss. Creep and shrinkage cause a shortening of the girder, and resultant losses of prestress are calculated considering equilibrium and compatibility. Loss due to relaxation is determined in accordance with the Canadian Prestressed Concrete Institute (1996) recommendations. Here the intrinsic relaxation, Δf_{pr}, is calculated as:

$$\Delta f_{pr} = \frac{\log(24t)}{45}\left[\frac{f_{pi}}{f_{py}} - 0.55\right] f_{pi} \tag{4.9}$$

where t is the age in days, f_{pi} is the stress in the steel at time zero and f_{py} is the yield strength of the prestressing steel. The yield strength of the steel is normally taken as $0.9f_{pu}$, where f_{pu} is the ultimate strength of the steel.

Intrinsic relaxation is based on a test where the strand is held at a constant length. To account for decreased effects due to a shortening of the prestressed beam, the intrinsic relaxation is reduced by the reduction coefficient χ_r as described by Ghali et al (2002) to give the reduced relaxation, $\Delta \bar{f}_{pr}$.

$$\Delta \bar{f}_{pr} = \chi_r \Delta f_{pr} \tag{4.10}$$

4.3.2.2 Effective Modulus Method

The first of the methods considered is the simpler, and uses the effective modulus to calculate stress related strains. The use of this method assumes that any stresses applied on a section are done so instantaneously. The effect of creep on the section is considered directly proportional to the creep function $J(t,t_0)$ with free shrinkage and prestress relaxation being effectively treated as forces on the section. The procedure is adapted from Collins and Mitchell (1987) and is summarised as follows. First the load vector is calculated as the sum of applied loads, shrinkage effects and prestressing.

$$\begin{Bmatrix} N(t,t_i) \\ M(t,t_i) \end{Bmatrix} = \begin{Bmatrix} N_0 \\ M_0 \end{Bmatrix} + \begin{Bmatrix} N(t,t_i) \\ M(t,t_i) \end{Bmatrix}_{shrinkage} + \begin{Bmatrix} N(t,t_i) \\ M(t,t_i) \end{Bmatrix}_{prestress} \tag{4.11}$$

where,

$$\begin{Bmatrix} N(t,t_i) \\ M(t,t_i) \end{Bmatrix}_{shrinkage} = E_{c,eff}(t,t_i)\varepsilon_{cs}(t,t_s)\begin{bmatrix} A_c \\ B_c \end{bmatrix} \tag{4.12}$$

$$\begin{Bmatrix} N(t,t_i) \\ M(t,t_i) \end{Bmatrix}_{prestress} = \begin{Bmatrix} -\sum n_j A_{ps} E_{p,eff} \varepsilon_{psj} \\ -\sum n_j A_{ps} E_{p,eff} \varepsilon_{psj} y_{psj} \end{Bmatrix} \tag{4.13}$$

The effective modulus of the prestressing, $E_{p,eff}$, accounts for relaxation by reducing the elastic modulus of the prestressing steel. It is calculated as:

$$E_{p,eff} = E_p - \frac{\Delta \bar{f}_{pr}}{\varepsilon_{psj}} \tag{4.14}$$

The strain distribution at any time t, after loading at t_i is then calculated as:

$$\begin{Bmatrix} \varepsilon_0(t,t_i) \\ \psi(t,t_i) \end{Bmatrix} = \frac{1}{E_{c,eff}(t,t_i)(A'I' - B'^2)} \begin{bmatrix} I' & -B' \\ -B' & A' \end{bmatrix} \begin{Bmatrix} N \\ M \end{Bmatrix} \tag{4.15}$$

where the prime symbol denotes an effective sectional property and is calculated as the transformed section property with respect to the effective modulus of the concrete, $E_{c,eff}(t,t_i)$. The effective Modulus is equal to the inverse of the creep function.

$$E_{c,eff}(t,t_i) = \frac{1}{J(t,t_i)} = \frac{E_c(t,t_i)}{1+\phi(t,t_i)} \tag{4.16}$$

4.3.2.3 Age-Adjusted Elastic Modulus Method

The second method follows the procedure described by Ghali et al (2002). In this method the time-dependent effects on a section are expressed by a change in strain, $\Delta\varepsilon_o$, and curvature, $\Delta\psi$, that occur over the time period considered. This is done by first calculating the forces required to prevent unrestrained creep, unrestrained shrinkage and strand relaxation, then applying these forces to the age-adjusted transformed section. The restraining force is:

$$\begin{Bmatrix}\Delta N(t,t_i)\\ \Delta M(t,t_i)\end{Bmatrix} = \begin{Bmatrix}\Delta N(t,t_i)\\ \Delta M(t,t_i)\end{Bmatrix}_{creep} + \begin{Bmatrix}\Delta N(t,t_i)\\ \Delta M(t,t_i)\end{Bmatrix}_{shrinkage} + \begin{Bmatrix}\Delta N(t,t_i)\\ \Delta M(t,t_i)\end{Bmatrix}_{relaxation} \tag{4.17}$$

where the restraining forces for creep, shrinkage and relaxation are determined as follows:

$$\begin{Bmatrix}\Delta N(t,t_i)\\ \Delta M(t,t_i)\end{Bmatrix}_{creep} = -E_{c,aa}(t,t_i)\phi(t,t_i)\begin{bmatrix}A_c & B_c\\ B_c & I_c\end{bmatrix}\begin{Bmatrix}\varepsilon_0(t_i)\\ \psi(t_i)\end{Bmatrix} \tag{4.18}$$

$$\begin{Bmatrix}\Delta N(t,t_i)\\ \Delta M(t,t_i)\end{Bmatrix}_{shrinkage} = -E_{c,aa}(t,t_i)\varepsilon_{cs}(t,t_i)\begin{bmatrix}A_c\\ B_c\end{bmatrix} \tag{4.19}$$

$$\begin{Bmatrix}\Delta N(t,t_i)\\ \Delta M(t,t_i)\end{Bmatrix}_{relaxation} = \begin{Bmatrix}\sum A_{ps}\Delta\bar{f}_{pr}\\ \sum A_{ps}y_{ps}\Delta\bar{f}_{pr}\end{Bmatrix} \tag{4.20}$$

where $E_{c,aa}(t,t_i)$ is the age-adjusted elastic modulus, and is defined as:

$$E_{c,aa}(t,t_i) = \frac{E_c(t,t_i)}{1+\chi\phi(t,t_i)} \tag{4.21}$$

The change in the sections strain distribution is calculated as follows:

$$\begin{Bmatrix} \Delta\varepsilon_0(t,t_i) \\ \Delta\psi(t,t_i) \end{Bmatrix} = \frac{1}{E_{c,aa}(t,t_i)(\bar{A}\bar{I}-\bar{B}^2)} \begin{bmatrix} \bar{I} & -\bar{B} \\ -\bar{B} & \bar{A} \end{bmatrix} \begin{Bmatrix} -\Delta N(t,t_i) \\ -\Delta M(t,t_i) \end{Bmatrix} \tag{4.22}$$

where $\bar{A}$, $\bar{B}$ and $\bar{I}$ are the age-adjusted transformed section properties. Thus the total strain distribution at time t after an age at loading of t_i is the sum of Equations 4.6 and 4.22.

4.3.3 Response with Changes in Boundary or Loading Conditions

Changes in boundary and loading conditions can, in general, be incorporated by satisfying the requirements of static equilibrium and compatibility, and by using the principle of superposition. This is illustrated in Figure 4.7, where a prestressed concrete girder is subjected to load case 1 at t_1, and load case 2 at t_2. At t_1, the load causes an upward deflection, which increases with time. At t_2, this load is removed, and its load effects with time are removed. Also at t_2, load case 2 is added. The summation of the separate cases produces a system that meets the requirements of static equilibrium and compatibility, while accounting for time-dependent effects. This method of superposition includes the effects of creep recovery under the assumption that creep recovery is proportional to creep.

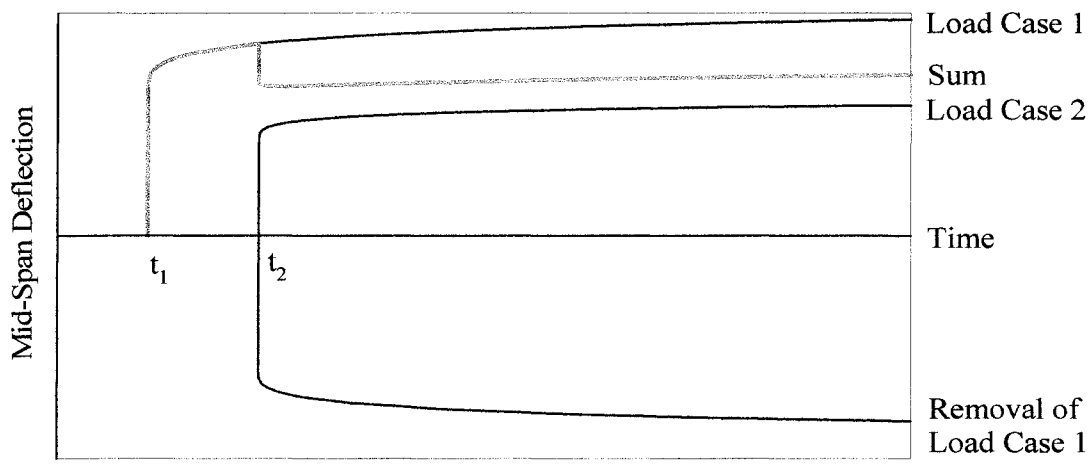

Figure 4.7: Linear Superposition of Load Effects

In using the method of superposition, events are characterised by discrete times, and at these times, the previous load case is removed while the new load case is applied. The response of the structure becomes a sum of the separate responses, whether it be strain distribution, mid-span deflection, or some other desired response.

However, in some cases special care must be given in the way that the requirements are met. For the structure considered, two such cases arise; the first is addition of the deck, which produces composite action and differential shrinkage between the deck and girder, and the second is the formation of a continuity diaphragm.

4.3.4 Concrete Deck and Composite Action

Composite action can be incorporated into either analysis method previously stated. In such cases where loads are applied to a composite section, the section properties and material properties are transformed with respect to a chosen reference modulus, and the analysis is performed as outlined. Problems arise when loads are applied at times when materials have no definable properties. This is because the methods outlined determine response over time with respect to initial properties. Both the effective and age-adjusted elastic moduli are based on the elastic modulus at the time of loading. Thus, because a deck has zero stiffness when poured, its transformed sectional properties are zero, and the problem becomes ill conditioned. One way to solve this problem is to choose a time, t_c, when composite action is considered to begin. Then load effects after this date are determined based on the age of the deck when composite action begins.

Thus, when the deck is poured, its stiffness is neglected until composite action begins. The load is fully carried by the girder, and the deck is free to shrink. At t_c the system is considered to become instantaneously composite. Differential shrinkage between the deck and girder now results in a positive moment acting on the section which begins at zero and gradually increases. This effect is handled differently by each method.

4.3.4.1 Effective Modulus Method

In this method, the deck shrinkage is treated as a set of forces acting on the composite section, and is added to the other restraining forces of Equation 4.11. Then the forces acting on the composite section are:

$$\begin{Bmatrix} N(t,t_c) \\ M(t,t_c) \end{Bmatrix} = \begin{Bmatrix} N_0 \\ M_0 \end{Bmatrix} + \begin{Bmatrix} N(t,t_c) \\ M(t,t_c) \end{Bmatrix}_{shrinkage} + \begin{Bmatrix} N(t,t_c) \\ M(t,t_c) \end{Bmatrix}_{prestress} + \begin{Bmatrix} N(t,t_c) \\ M(t,t_c) \end{Bmatrix}_{shrinkage,D} \tag{4.23}$$

where,

$$\begin{Bmatrix} N(t,t_c) \\ M(t,t_c) \end{Bmatrix}_{shrinkage,D} = E_{c,eff,D}(t,t_i)\varepsilon_{cs,D}(t,t_c)\begin{bmatrix} A_{c,D} \\ B_{c,D} \end{bmatrix} \tag{4.24}$$

Here the subscript D denotes that the property is associated with the deck. The strain distribution at any time t can then be determined from Equation 4.15, where the effective transformed section properties of the girder become the effective transformed section properties of the composite section.

4.3.4.2 Age-Adjusted Elastic Modulus Method

For the application of this method two steps are needed. First the elastic response of the section must be calculated at the time composite action takes place, where the girder resists all applied loads. From this point in time the restraint forces required to restrain free girder creep, shrinkage, prestress relaxation, and deck shrinkage are calculated. To restore static equilibrium, the restraint forces are applied to the composite section in an equal and opposite manner. The result is the change in strain distribution over the time interval considered.

The elastic response is calculated from Equation 4.6 for all loads applied (self-weight, prestressing and deck weight) and resisted by the girder only.

The restraining force required to restrain deck shrinkage is added to the other restraining forces of Equation 4.17 to give a total restraining force:

$$\begin{Bmatrix}\Delta N(t,t_c)\\ \Delta M(t,t_c)\end{Bmatrix} = \begin{Bmatrix}\Delta N(t,t_c)\\ \Delta M(t,t_c)\end{Bmatrix}_{creep} + \begin{Bmatrix}\Delta N(t,t_c)\\ \Delta M(t,t_c)\end{Bmatrix}_{shrinkage} + \begin{Bmatrix}\Delta N(t,t_c)\\ \Delta M(t,t_c)\end{Bmatrix}_{relaxation} + \begin{Bmatrix}\Delta N(t,t_c)\\ \Delta M(t,t_c)\end{Bmatrix}_{shrinkage,D} \tag{4.25}$$

where,

$$\begin{Bmatrix}\Delta N(t,t_c)\\ \Delta M(t,t_c)\end{Bmatrix}_{shrinkage,D} = -E_{c,aa,D}(t,t_c)\varepsilon_{cs,D}(t,t_c)\begin{bmatrix}A_{c,D}\\ B_{c,D}\end{bmatrix} \tag{4.26}$$

Then Equation 4.22 is used to calculate the change in strain of the section over the time period considered, where the age-adjusted transformed section properties are replaced by the age-adjusted transformed section properties of the composite section. Then the strain distribution at the end of the time period becomes the sum of the elastic and time-dependent strain distributions.

4.3.5 Continuity Diaphragm

The creation of a diaphragm at centre-span, creating continuity, has the effect of restricting end rotation. As a result, the system becomes statically indeterminate with a restraining moment developing over the centre pier to maintain continuity. Both methods use the same procedure outlined below.

The force method is used to determine the magnitude of the restraint moment, where the system is first freed of its rotational restraint making the system determinate. Over the time period considered, the amount of end rotation of the freed system is calculated. Then the restraint moment required to restore compatibility is determined, and applied to the structure, restoring compatibility. In the calculation of the restraint moment, the age-adjusted properties of the structure are used.

To incorporate the gradual increase in the restraint moment, Equation 4.8 is decomposed, such that only the change in stress over the time period is considered. The change in stress is due to the development of the restrain moment.

$$\varepsilon_{cc}(t) = \Delta\sigma_c(t)\cdot\frac{1+\chi\phi(t,t_c)}{E_c(t_c)} \tag{4.27}$$

By its definition, Equation 4.27 implies that a stress increasing from zero to $\Delta\sigma_c$ at time t produces a strain $[1+\chi\phi(t,t_c)]$ times the instantaneous strain that would occur if the stress were introduced at time t_c. Then, the strain distribution resulting from the restraint load case can be determined as:

$$\begin{Bmatrix}\varepsilon_0(t,t_c)\\ \psi(t,t_c)\end{Bmatrix}_{\text{Re stra int}} = \frac{1}{E_{c,aa}(t,t_c)(\overline{A}\overline{I}-\overline{B}^2)}\begin{bmatrix}\overline{I} & -\overline{B}\\ -\overline{B} & \overline{A}\end{bmatrix}\begin{Bmatrix}-N(t,t_c)\\ -M(t,t_c)\end{Bmatrix}_{\text{Re stra int}} \tag{4.28}$$

Because the structure is no longer determinate, the compatibility condition of end rotation must be invoked to solve for the magnitude of the restraint moment. For convenience, the diaphragm is considered to be rigid, and the condition is that, at t_c, end rotation of the composite section at the centre pier becomes fixed. Numerical integration of curvature can be used to provide slope of the section. Then for times greater than t_c, the free rotation is calculated. Iteration can be used to determine the value of the restraint moment required to restore compatibility.

If the other system is considered free to deform axially, no axial load develops at the diaphragm. The restraint moment can be termed $M_R(t,t_c)$, and the load vector for the load case of the restraint moment can be written for convenience as:

$$\begin{Bmatrix}-N(t,t_c)\\ -M(t,t_c)\end{Bmatrix}_{\text{Re stra int}} = \begin{Bmatrix}0\\ -M_R(t,t_c)\end{Bmatrix}_{\text{Re stra int}} \tag{4.29}$$

4.3.6 Thermal Considerations

In the preceding methods, and in the following sections thermal strains are not considered. The consideration of thermal effects can be incorporated into the analysis performed (see Ghali et al. (2002)), however, in the analysis of real structures, assessing the magnitude of locked in thermal strain profiles is not trivial. For example, the thermal profile at continuity would impact the strain distribution locked into the system, but considering that the age at continuity is not certain, the results of this would be highly variable. In other words, it is difficult to assess the point when thermal strains become locked into the system and equally difficult to accurately predict the thermal profile of the cross-section at that moment. To reduce thermal effects, measurements were taken at times when thermal gradients were expected to be minimal.

4.4 Results and Analyses

Measurements were made at times indicated in Table 4.3. Due to the large amount of information obtained, only selected data will be presented. As well, because no measurements were taken after integral-abutment connection, this change in boundary condition is not considered in the predicted results.

Analyses were made using the methods presented. Material properties were predicted using ACI 209, CEB MC-90 and Model A as indicated, using an average annual relative humidity in Calgary, Alberta of 55%. The self-weight of the girder and deck were taken the same as used in the original design as 24.8 kN/m and 24.5 kN/m^3 respectively.

The recommendation from Canadian Prestressed Concrete Institute (1996) were used to predict transfer lengths for prestressing strands. The transfer length is estimated to be approximately 50 times the diameter of the strand. For 15.2 mm strands, this amounts to a transfer length of 760 mm. In the case that the prestressing strand is partially debonded, the transfer length is doubled to 1520 mm.

The recommendations from Bulletin d'Information 215 (1993) were used to estimate the aging coefficient. The recommended equation is:

$$\chi = \frac{t_i^{0.5}}{1 + t_i^{0.5}} \tag{4.30}$$

It was found, however, that the maximum range on predictions due to varying χ between it limits was 3.4 mm of mid-span deflection. This indicates that χ has a relatively negligible effect on the prediction.

4.4.1 Elastic Response

The measured elastic response of the two girders is shown in Figures 4.8 and 4.9, along with predicted behaviour. Figure 4.8 shows curvature along the length, while Figure 4.9 shows the deflected shape. At the time of prestress transfer, the two girders share identical load-histories, and thus have identical predictions of behaviour. Concrete properties were predicted using Model A.

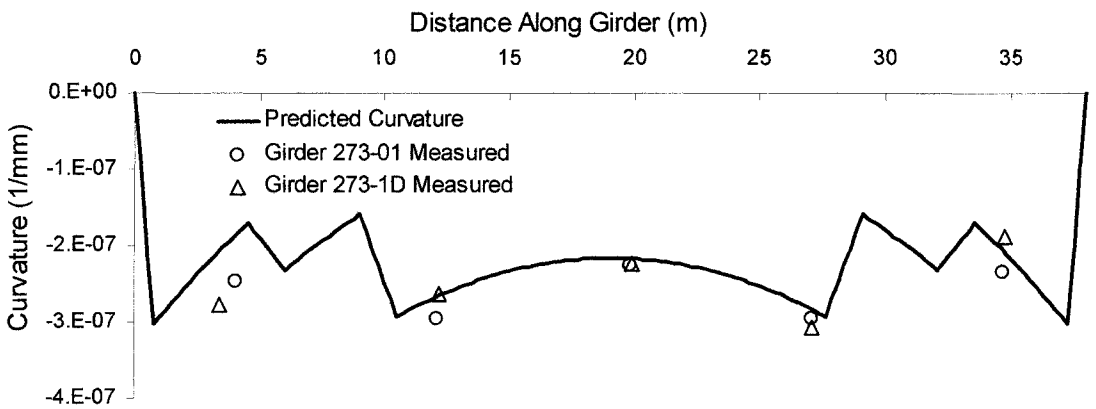

Figure 4.8: Curvature Distribution Immediately After Prestress Transfer

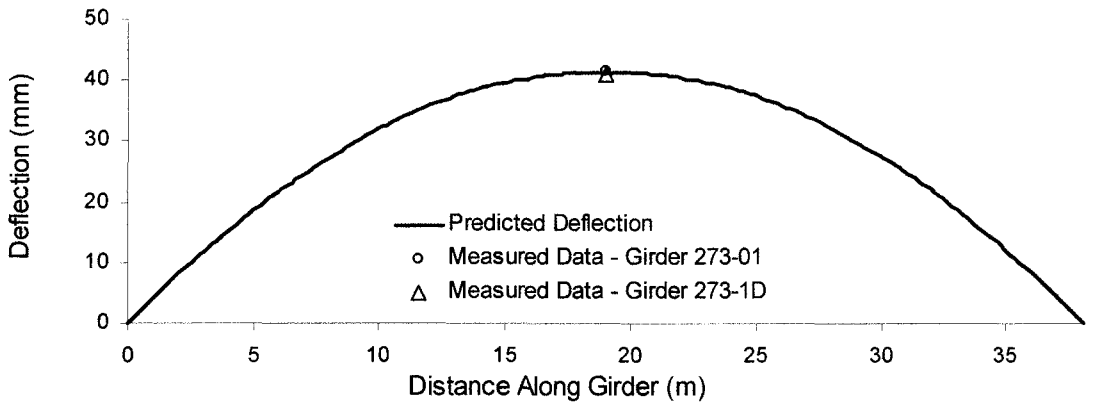

Figure 4.9: Deflected Shape Immediately After Prestress Transfer

4.4.2 Time-Dependent Response

Figure 4.10 shows the mid-span deflection for girder 273-01 for the first 300 days after prestressing. Predictions from the two different methods for predicting time-dependent effects are shown along with the measured camber readings. Table 4.4 summarises measured and predicted values for all methods of predicting for both girders.

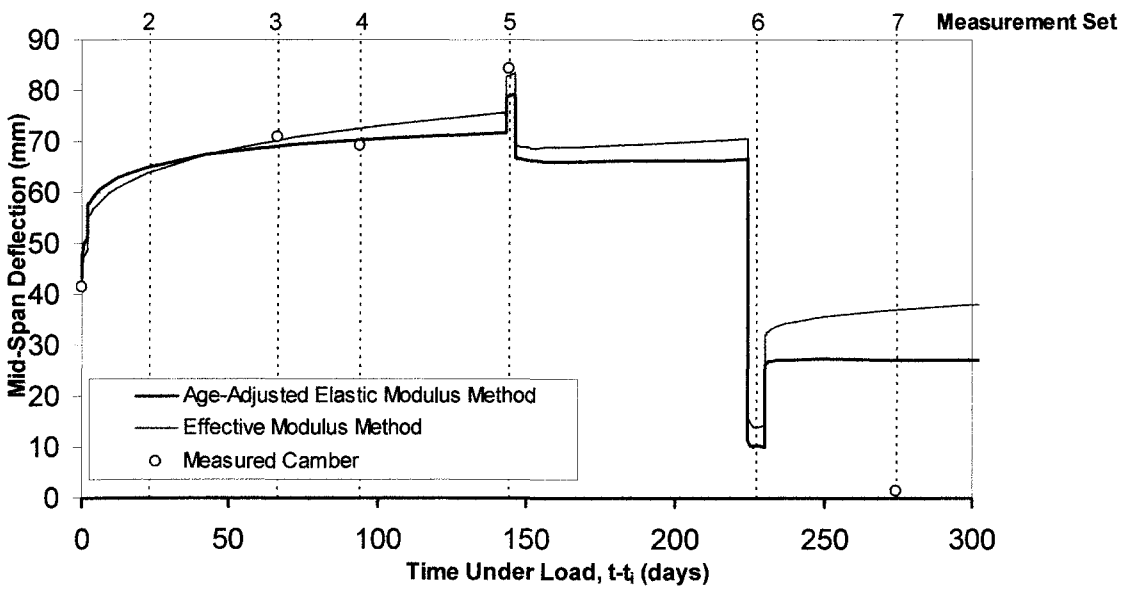

Figure 4.10: Effect of Analysis Method on Predicted Mid-Span Deflection Growth for Girder 273-01

Table 4.4: Measured and Predicted Mid-Span Camber

Girder 273-01			Effective Modulus Method		Age-Adjusted Elastic Modulus Method					
Measurement Set	Girder Age (days)	Measured Camber Δ_{MEAS} (mm)	Model A		Model A		ACI 209		CEB MC-90	
			Δ_{PRED} (mm)	$\Delta_{MEAS} - \Delta_{PRED}$	Δ_{PRED} (mm)	$\Delta_{MEAS} - \Delta_{PRED}$	Δ_{PRED} (mm)	$\Delta_{MEAS} - \Delta_{PRED}$	Δ_{PRED} (mm)	$\Delta_{MEAS} - \Delta_{PRED}$
1	1	41.5	41.3	0.2	41.3	0.2	42.0	-0.5	35.1	6.4
3	67	70.8	70.1	0.7	68.9	1.9	76.9	-6.1	76.8	-6.0
4	95	69.2	72.7	-3.5	70.1	-0.9	79.2	-10.0	80.2	-11.0
5	145	84.3	82.3	2.0	78.2	6.1	86.6	-2.3	87.7	-3.4
7	275	1.5	37.0	-35.5	27.2	-25.7	43.3	-41.8	51.4	-49.9

Girder 273-1D			Effective Modulus Method		Age-Adjusted Elastic Modulus Method					
Measurement Set	Girder Age (days)	Measured Camber Δ_{MEAS} (mm)	Model A		Model A		ACI 209		CEB MC-90	
			Δ_{PRED} (mm)	$\Delta_{MEAS} - \Delta_{PRED}$	Δ_{PRED} (mm)	$\Delta_{MEAS} - \Delta_{PRED}$	Δ_{PRED} (mm)	$\Delta_{MEAS} - \Delta_{PRED}$	Δ_{PRED} (mm)	$\Delta_{MEAS} - \Delta_{PRED}$
1	1	41.0	41.2	-0.2	41.2	-0.2	41.8	-0.8	34.9	6.1
3	62	70.8	69.9	0.9	68.6	2.2	78.1	-7.3	76.4	-5.6
4	90	67.5	72.5	-5.0	70.0	-2.5	80.1	-12.6	79.9	-12.4
5	140	76.9	82.9	-6.0	80.7	-3.8	89.8	-12.9	89.7	-12.8
7	271	5.0	36.3	-31.3	24.9	-19.9	46.1	-41.1	49.6	-44.6

Figure 4.11 shows the curvature distribution for selected times as predicted using the two analysis methods along with measured curvatures.

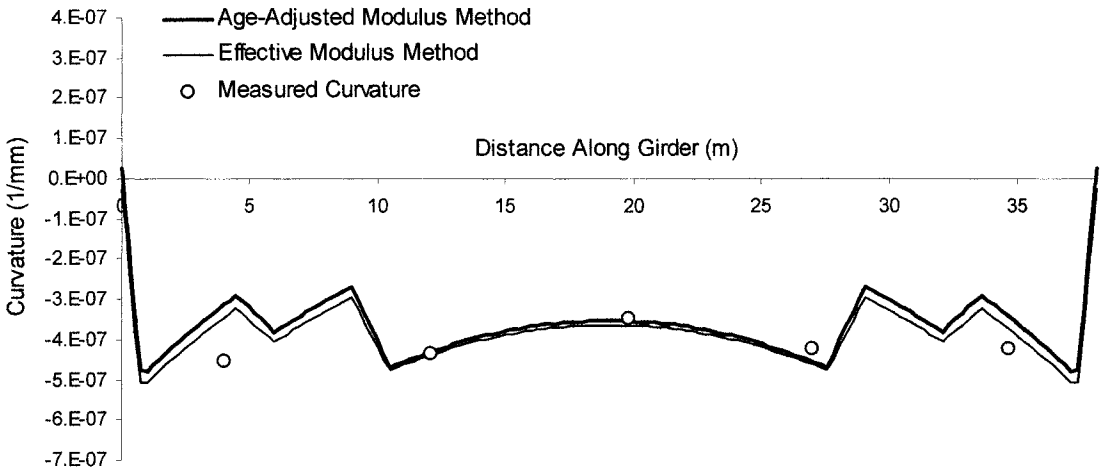

Figure 4.11a: Measurement Set 3, 67 Days Under Load

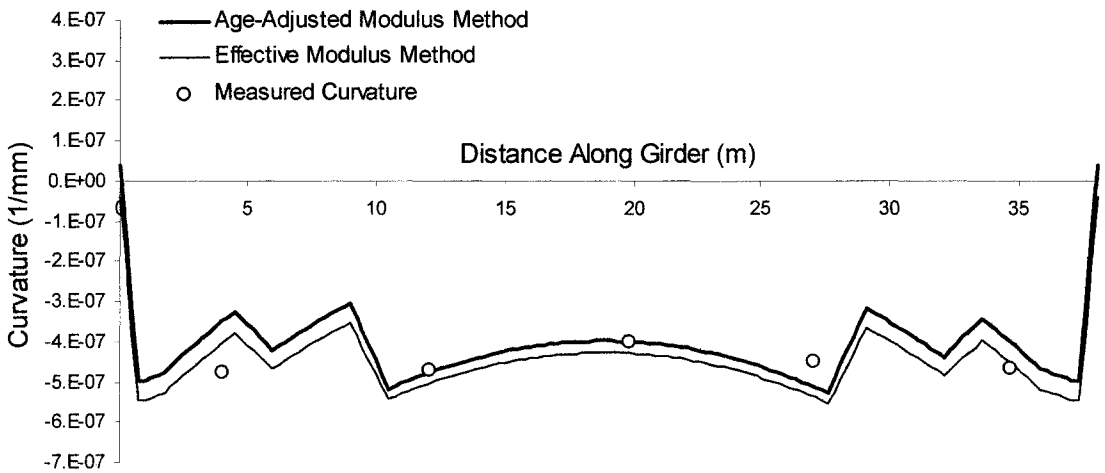

Figure 4.11b: Measurement Set 5, 144 Days Under Load

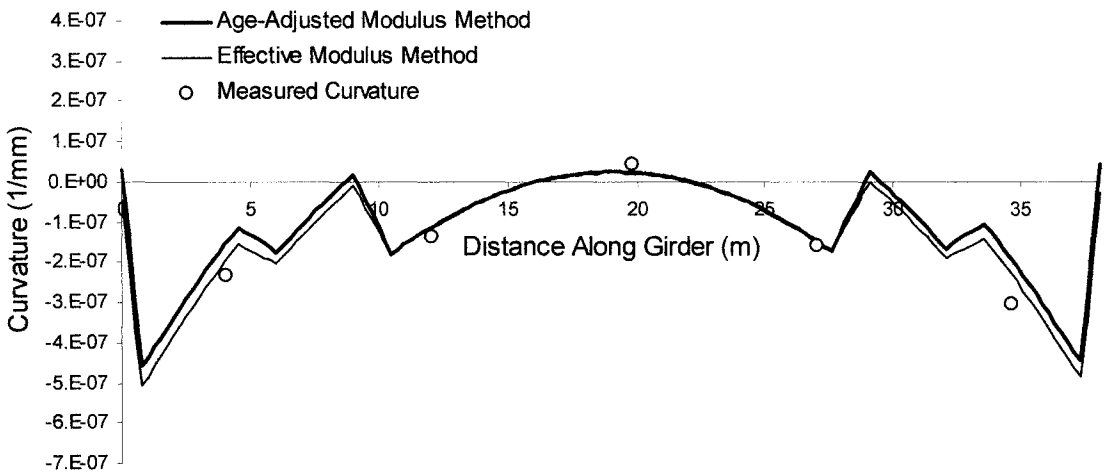

Figure 4.11c: Measurement Set 6, 228 Days Under Load

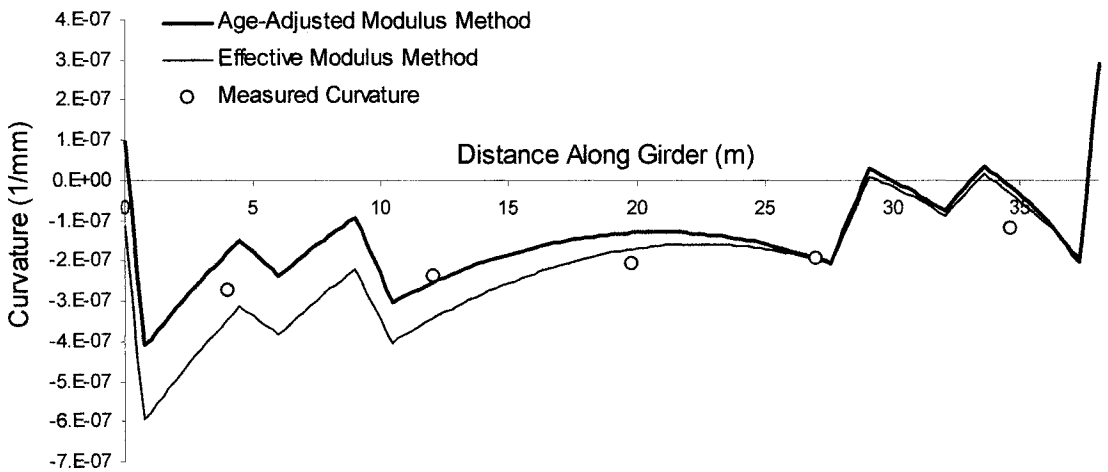

Figure 4.11d: Measurement Set 7, 275 Days Under Load

Figure 4.11: Effect of Analysis Method on Predicted Curvature for Girder 273-01

Figure 4.12 shows the effect of material model on the predicted mid-span deflection growth while Figure 4.13 shows the effect of material model on the predicted curvature distribution at 271 days under load for Girder 273-1D. The analyses were made using the age-adjusted elastic modulus method. In each case the specified model code is used to predict the properties of both the girder and the deck.

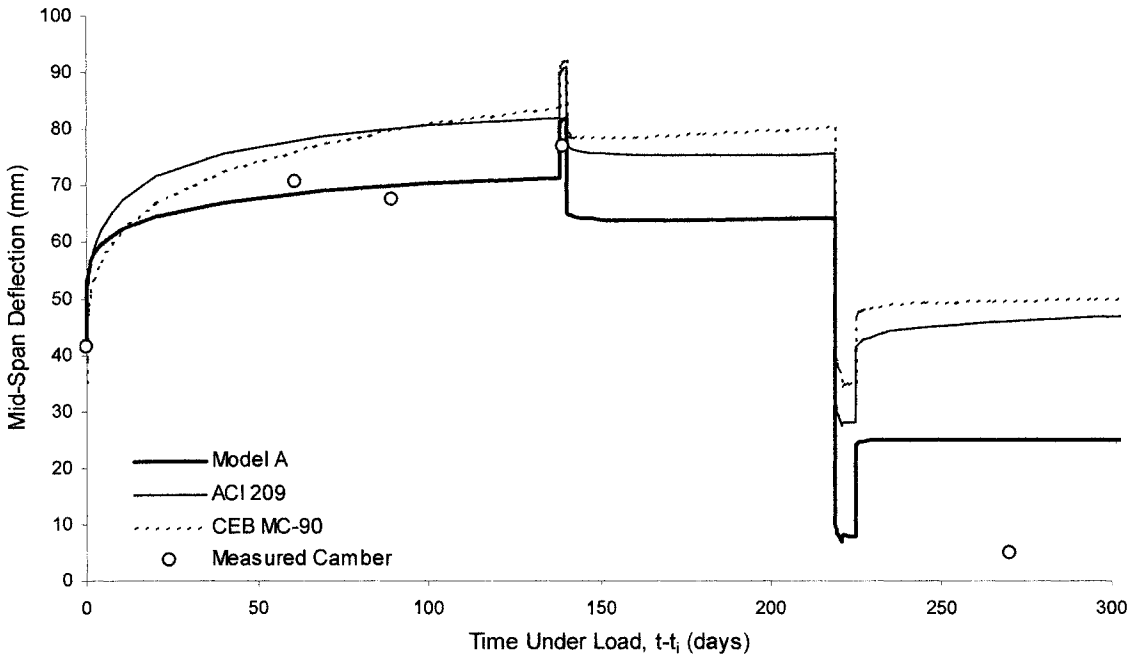

Figure 4.12: Effect of Material Model on Predicted Mid-Span Deflection Growth for Girder 273-1D Using Age-Adjusted Elastic Modulus Method of Analysis

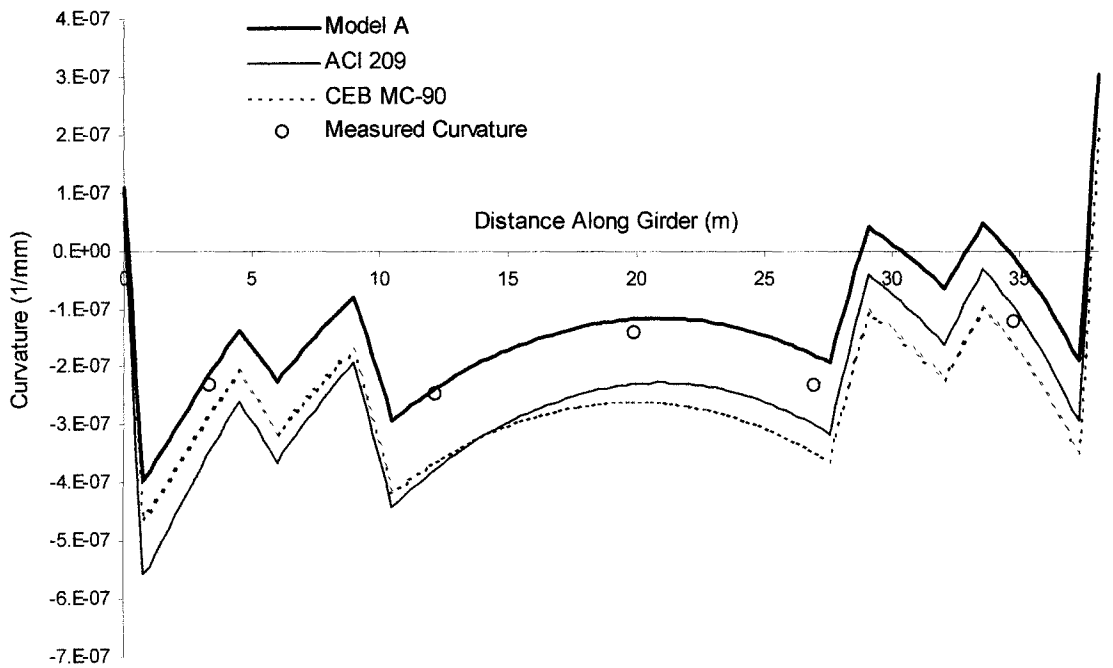

Figure 4.13: Effect of Material Model on Predicted Curvature Distribution for Girder 273-1D Using Age-Adjusted Elastic Modulus Method of Analysis

4.5 Discussion

Figure 4.9 shows the elastic response of the structure at the time of prestress transfer. The components required to attain an accurate prediction of elastic behaviour are an accurate model of the structure, and a sufficient structural analysis method. The structural model includes concrete stiffness, steel stiffness, prestress levels and transfer lengths, and sectional properties. The predicted curvature distribution agrees well with the five measured sections along the length. This gives confidence to the model of the structure used, namely those properties that have uncertainty associated with them, and can highly affect response, like the prestress transfer length.

Two types of measurements of behaviour were taken; the mid-span camber and sectional strain distributions which were converted into curvatures.

Figure 4.10 shows the mid-span camber growth with time for the structure. The various events that occur can be traced through the history of the structure, resulting in sudden jumps in the predicted mid-span camber. Table 4.4 shows that the predicted response using either analysis method with Model A agree within 6 mm of measured camber for the readings taken prior to erection. However, for measurement set 7, which occurs after post-tensioning there is a 20 mm to 30 mm difference between measured camber and predicted camber.

Figure 4.11 shows the curvature distribution for the structure at several selected times. At all sampling times, the predicted curvature distribution is very close to the measured curvatures, including at measurement set 7 (at 275 days).

Thus, there is some disagreement between the two methods of measuring deformations at measurement 7. While the measured camber is significantly lower than the predicted camber, the measured curvature is very close to the predicted curvature. There are several factors that may have influenced the camber readings, including ice on the surface of the girders, and cramped dark conditions after deck pour that required a change in

survey rod and sighting 38 m in the dark. As well, marks indicating survey stations were removed during the construction process, decreasing reliability from one set of readings to the next. The primary method of measurement was the sectional strain readings, which were reproducible and not affect by construction (e.g. formwork). For these reasons, there is a higher confidence in the curvature readings used for determining the accuracy of predictions.

Figures 4.10 and 4.11 show time-dependent behaviour as predicted by the two analysis methods considered. It is seen that the same elastic response at prestress transfer is obtained using either method, but as the time under load increases, the predictions of mid-span camber diverge. Prior to the deck pour at 225 days, there is a difference of 4.2 mm in the prediction of mid-span camber. After composite action, and post-tensioning, the predictions in mid-span deflection continue to diverge, and reach 12.9 mm by an age of 350 days.

Figure 4.11 shows the same comparison of methodologies in terms of curvature distributions. For most times considered, both predictions give very similar predictions. The biggest difference between predicted curvature distributions is seen in Figure 4.11d, where both methods provide reasonable predictions. Interestingly, the two methods of prediction nearly encompass the measured curvatures. While the Age-Adjusted Elastic Modulus Method can be considered the more theoretically sound method, for this case it cannot be said to give a more accurate prediction of behaviour than the Effective Modulus Method.

The effect of material model code on predictions of behaviour is shown in Figures 4.12 and 4.13 and summarised in Table 4.4. In Figure 4.12 it is seen that the difference in predictions between ACI 209, CEB MC-90 and Model A increase with the age of the structure. For all measured times, Model A provides the best prediction, being within 6 mm for all measurements except for the reading at 271 days where it was within 19.9 mm. The use of CEB MC-90 produced predictions within 13 mm for early ages, and

44.6 mm at 271 days, compared the use of ACI 209 that produced results within 13 mm for early ages and 41.1 mm at 271 days.

Figure 4.13 shows the predictions of curvature at 271 days using ACI 209, CEB MC-90 and Model A. This figure shows that the prediction made using Model A is the most accurate, while the prediction made using either ACI 209 or CEB MC-90 result in a significant overestimate.

4.6 Conclusions

Based on the investigation presented, the following conclusions can be drawn.

1. The use of either the Effective Modulus Method or the Age-Adjusted Elastic Modulus Method with a material model that can accurately describe the concrete's mechanical properties, and a sufficient structural model will give accurate results. As well, the procedures outlined provide the consideration of changes in loading and boundary conditions, and changes in section properties.

2. For the case study considered, the Age-Adjusted Elastic Modulus Method and the Effective Modulus Method produce predictions that diverge from one another. However, based on the measured field data, neither method can be considered to give more accurate predictions than the other.

3. In this study, the use of either ACI 209 or CEB MC-90 to predict the material properties of the girder and deck result in an overestimate of the magnitude of curvature and deflection.

4. Compared to the predictions made using ACI 209 and CEB MC-90, the use of the material model that was tuned to measured laboratory data resulted in an increase in accuracy. This increase in accuracy was evident in the prediction of both mid-span deflection and curvature.

4.7 References

ACI Committee 209. 1997. *Prediction of Creep, Shrinkage, and Temperature Effects in Concrete Structures, (ACI 209R-92),* American Concrete Institute, Farmington Hills, MI.

Bazant, Z.P. 1972. *Prediction of Concrete Creep Effects Using Age-Adjusted Effective Modulus Method*, ACI Journal, V. 69, No. 4, pp. 212-217.

Bulletin d'Information 215. 1993. *Structural Effects of Time-Dependent Behaviour of Concrete*, Comité Euro-International du Béton, Laussane, Switzerland.

Canadian Prestressed Concrete Institute. 1996. *CPCI Design Manual 3rd Edition*, Canadian Prestressed Concrete Institute, Ottawa, Ontario, Canada.

Collins, M.P. and Mitchell, D. 1987. *Prestressed Concrete Basics*, Canadian Prestressed Concrete Institute, Ottawa, Ontario, Canada.

Comité Euro-International du Béton. 1993. *CEB-FIP Model Code 1990*, Redwood Books, Trowbridge, Great Britain.

Ghali, A., Favre, R. and Elbadry, M. 2002. *Concrete Structures: Stresses and Deformations 3rd Edition*, Spon Press, New York, NY.

Trost, H. 1967. *Implications of the Superposition Principle in Creep and Relaxation Problems for Concrete and Prestressed Concrete*, Beton-und Stahlbetonbau (Berlin-Wilmersdorf), N. 10, pp. 230-238, 261-269.

5

Comparative Design

5.1 Introduction

The main objective of this chapter is to investigate the implications of changing the structural system of the 130th Avenue and Deerfoot Trail Overpass, a "typical" structure, from internal post-tensioning to external post-tensioning. This includes a comparison of concrete stresses at applicable limit states and a comparison of ultimate capacities between the two designs. It also includes an investigation into the effects that external tendon loss has on concrete stresses and ultimate capacity. The differences in required concrete, ordinary reinforcement, and post-tensioned reinforcement are of particular interest.

To predict the ultimate capacity of externally post-tensioned beams, an estimate of tendon stress at ultimate is required. As a secondary objective, the effect of changing the method of estimating tendon stress on ultimate moment capacity is investigated.

To obtain meaningful results requires confidence in the prediction of behaviour of the structure. The study presented in Chapter 4 shows that an accurate prediction of the service behaviour of this structure is obtained using a representative concrete model with an appropriate analysis method.

5.2 Background

The construction of the 130th Avenue and Deerfoot Trail Overpass uses 38 metre long precast-prestressed trapezoidal concrete girders as the main structural elements. The construction sequence for the super structure is: 1) Erect pre-cast girders on piers; 2) Place deck and diaphragms to create continuity; 3) Post-tension longitudinally (from both ends simultaneously); and 4) Make integral bridge/abutment connection. For this investigation, integral abutments were substituted with sliding bearings.

5.3 Design Criteria

5.3.1 Code

In this study, the overpasses are designed using the current Canadian Highway Bridge Design Code (CSA S6-00). In cases where better information exists, it is used to supplement CSA S6-00, with these exceptions noted where appropriate.

5.3.2 Applicable Limit States

CSA S6-00 lists 11 load combinations, which cover fatigue, serviceability, and ultimate limit states. Two of these are used for serviceability and ultimate limit states, with two additional combinations for temporary stress states during construction.

Table 5.1 lists the load combinations for the applicable limit states. In this Table, D represents dead load, P represents secondary prestress effects, L represents the vehicular live load, and C represents the construction live load.

5.3.2.1 Serviceability Limit State

Serviceability Limit State 1 (SLS 1) is used to check girder and deck concrete stresses in service.

5.3.2.2 Ultimate Limit State

Ultimate Limit State 1 (ULS 1) is used for ultimate flexural and shear capacity.

5.3.2.3 Temporary Stresses

Temporary Limit State 1 (TLS 1) is used to check girder concrete stresses at prestress transfer and erection, where the dead load consists of the self-weight of the girder.

Temporary Limit State 2 (TLS 2) is used to check girder concrete stresses at deck pour. The dead load is comprised of the girder self-weight, the wet deck and formwork. A construction live load is also applied.

Table 5.1: Load Combinations

	Permanent Loads		Transitory Loads	
Limit State	D	P	L	C
SLS 1	1	1	0.9	0
ULS 1	α_d	α_p	1.7	0
TLS 1	1	0	0	0
TLS 2	1	0	0	1

α_d = Load Factor for Dead Loads
α_p = Load Factor for Secondary Prestressing Effects
Load Factors as per CSA S6-00

5.3.3 Loads

5.3.3.1 Dead Loads

The specified dead loads used throughout the design are summarised in Table 5.2. For simplicity it is assumed the deck formwork is removed at the same time the asphalt pavement is applied.

Table 5.2: Dead Loads

Part	Load
Girder - Design 1	25.7 kN/m
Girder - Design 2	21.8 kN/m
Haunch	1.2 kN/m per girder
Deck	5.4 kN/m^2
Asphalt	1.2 kN/m^2
Deck Forms	1.0 kN/m^2

5.3.3.2 Live Loads

The vehicular live load is based on a CL-800 load. Refer to Appendix A for calculation of the load effects. The construction live load is taken as 1.0 kPa.

5.3.4 Materials

The specified material properties are summarised in Table 5.3.

Table 5.3: Material Properties

Material	Strength
Girder Concrete	$f'_{cRELEASE}$ = 40 MPa f'_{c28DAY} = 60 MPa
Deck Concrete	f'_{c7DAY} = 40 MPa f'_{c28DAY} = 45 MPa
Ordinary Reinforcing Steel	f_y = 400 MPa
Prestressing Strands	f_{pu} = 1860 MPa

A comprehensive testing program was performed on the concrete used in the girders of the 130th Avenue and Deerfoot Trail Overpass (see Chapter 3). From the testing results, a mix-specific model, termed Model A, was developed to describe strength gain, stiffness, shrinkage and creep. Model A is used here for the prediction of time-dependent effects and concrete stress calculations relating to the girder concrete. Deck concrete properties are predicted using the recommendations from ACI Committee 209 (1997).

All prestressing strands are 15.2 mm diameter low-relaxation strands with an area of 140 mm^2. The constitutive properties and relaxation properties were taken from the Canadian Prestressed Concrete Institute (1996).

Ordinary reinforcing steel has a modulus of elasticity of 200 GPa, and is assumed to be linear elastic-perfectly plastic without strain hardening for strains past yield.

5.3.5 Schedule

Time-dependent behaviour is considered in this design. The construction schedule is summarised in Table 5.4.

Table 5.4: Construction Schedule

Event	Time from Girder Casting
Prestress Transfer	12 Hours
Erection	40 Days
Deck Pour	47 Days
Post-Tensioning	54 Days
End of Service Life	75 Years

5.3.6 Overall Geometry

Figure 5.1 shows the profile of the overpass and a typical section.

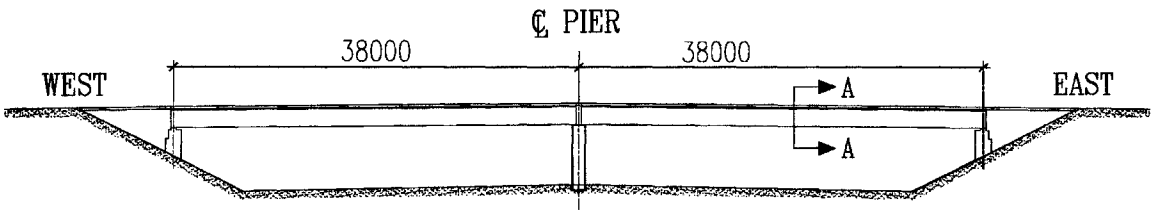

(a) Overpass Profile

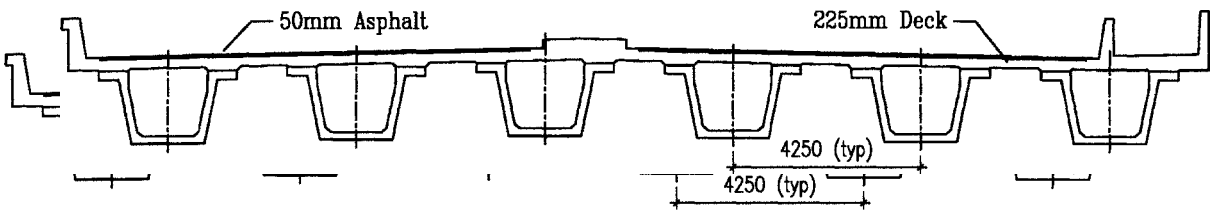

(b) Section A-A of Overpass

Figure 5.1: Overpass Geometry

5.4 Design Details

In the designs presented, only a typical interior girder was considered. For this overpass the governing load cases are for interior girders. As well, it is typical for highway overpasses to have identically designed girders, rather than using girders with less capacity on the edges. This is done to accommodate future changes in traffic volumes and possible widening of the driving surface.

5.4.1 Cross-Section

Design 1 of the 130th Avenue overpass uses the original girder cross-section with internal post-tensioning, while Design 2 uses an altered cross-section with external post-tensioning. Cover requirements of the internal post-tensioning ducts and reinforcing steel govern the web-thickness in Design 1. With the same cover requirements, removal of the internal ducts and replacement of the two layers of shear reinforcement with a single layer results in a minimum web-thickness of 102.4 mm. Following discussions with the precaster, a web-thickness of 125 mm was chosen for Design 2. Figures 5.2 and 5.3 show the geometry of the girder cross-sections. Note that the actual construction of the 130th Avenue overpass used a design similar to Design 1.

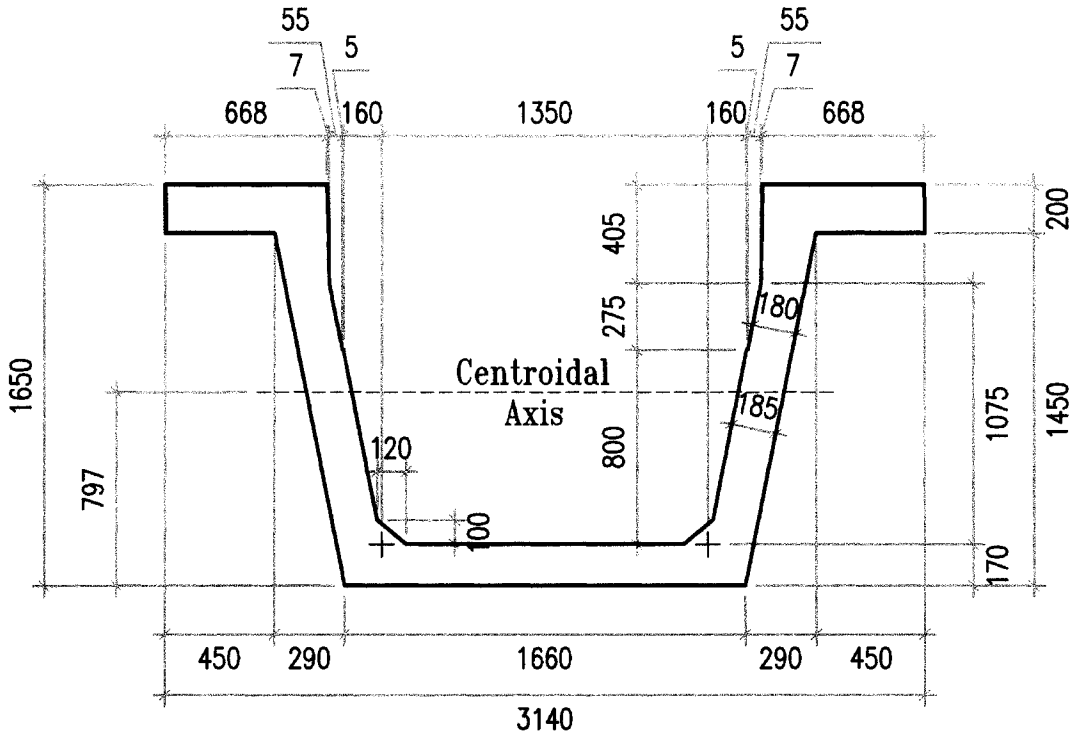

Figure 5.2: Girder Cross-Section – Design 1 with Internal Post-Tensioning

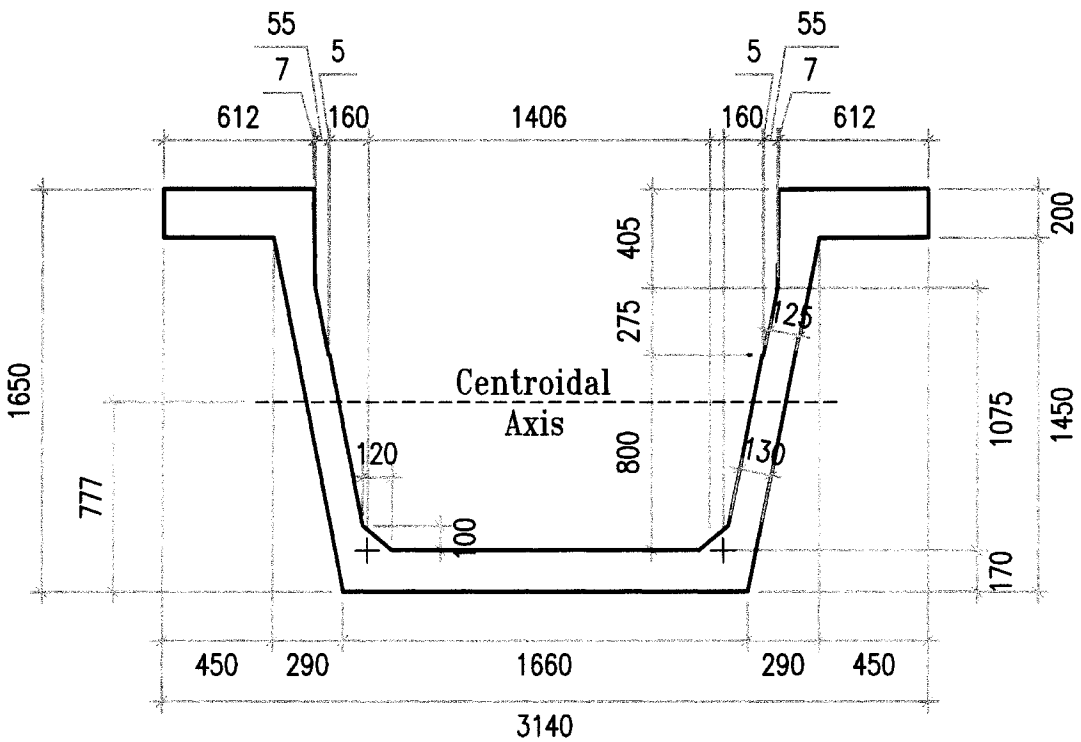

Figure 5.3: Girder Cross-Section – Design 2 with External Post-Tensioning

5.4.2 Longitudinal Flexural Reinforcement

Both designs contain the same quantity of ordinary flexural reinforcement, which is summarised in Table 5.5. The reinforcing steel in the deck was proportioned using the empirical design method in CSA S6-00 and is summarised in Appendix B.

Table 5.5: Longitudinal Flexural Steel Quantities – Both Designs

Location	Bar Designation	Number	Height (mm) *
Deck Layer 1	15 M	300 mm O/C = 15	1796
Deck Layer 2	15 M	300 mm O/C = 15	1744
Top Flange Layer 1	15 M	8	1590
Top Flange Layer 2	15 M	8	1510
Bottom Flange Layer 1	15 M	10	110
Bottom Flange Layer 2	15 M	10	60

* Refer to Figures 5.22 and 5.23 for a graphical description

5.4.3 Shear Reinforcement

Shear reinforcement for Design 1 is shown in Figure 5.4, and the shear reinforcement for Design 2 is shown in Figure 5.5. For both designs the total area of shear reinforcement per linear metre is the same. It should be noted that the spacing of 40 mm at the girder end in design 2 would not be used in a final design, and is only used here to avoid differences between the designs in terms of shear design and capacity.

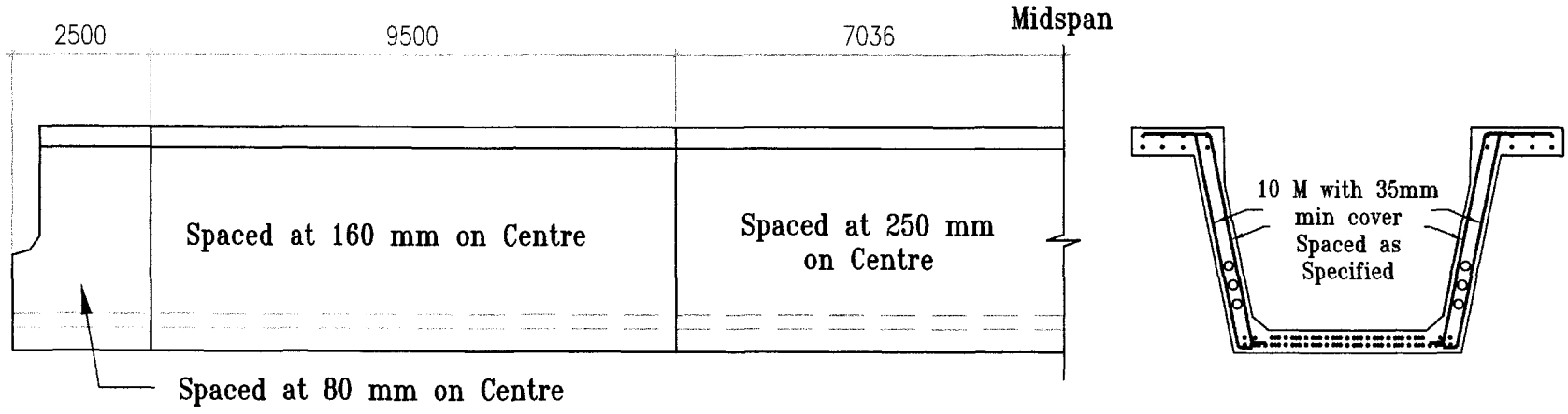

Figure 5.4: Shear Reinforcement Design – Spacing and Section – Design 1

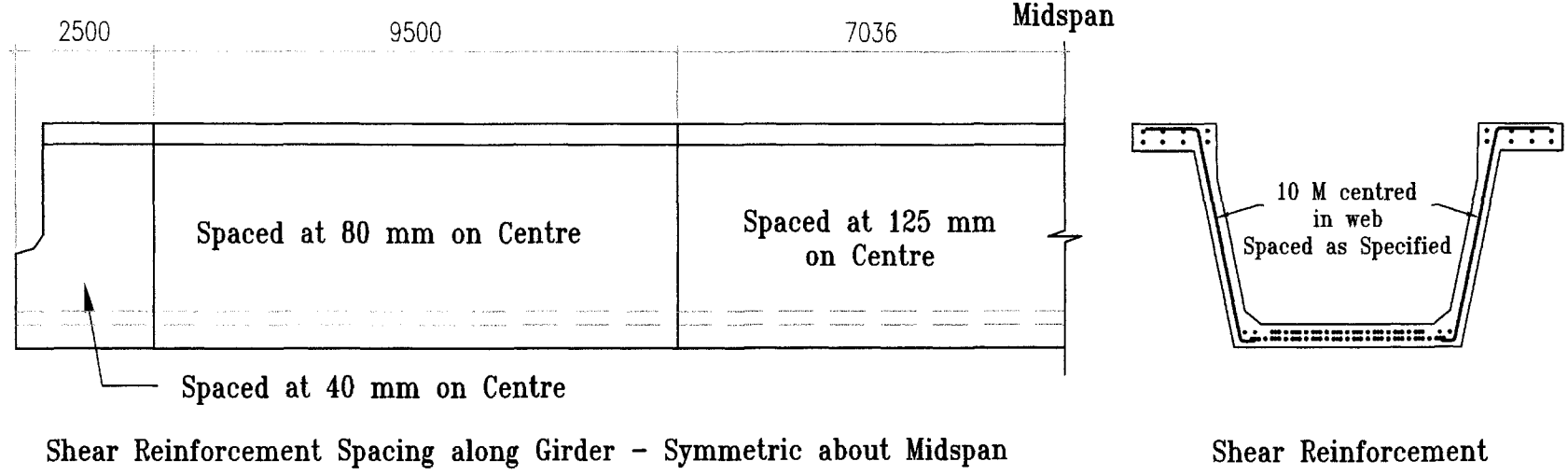

Figure 5.5: Shear Reinforcement Design – Spacing and Section – Design 2

5.4.4 Pretensioning

Figures 5.6 and 5.7 show the pretensioned strand patterns. Strands extend the length of the girders, with specified strands debonded for indicated lengths. Each strand is stressed to 75% of ultimate strength ($f_{po} = 0.75f_{pu}$).

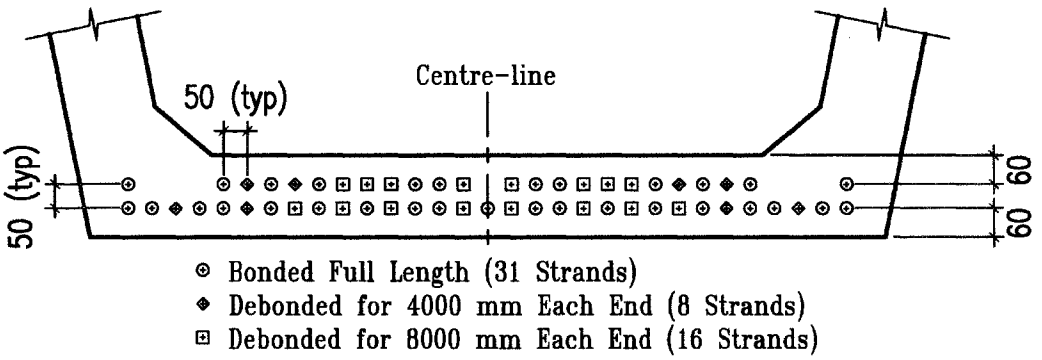

Figure 5.6: Pretensioned Strand Pattern – Design 1

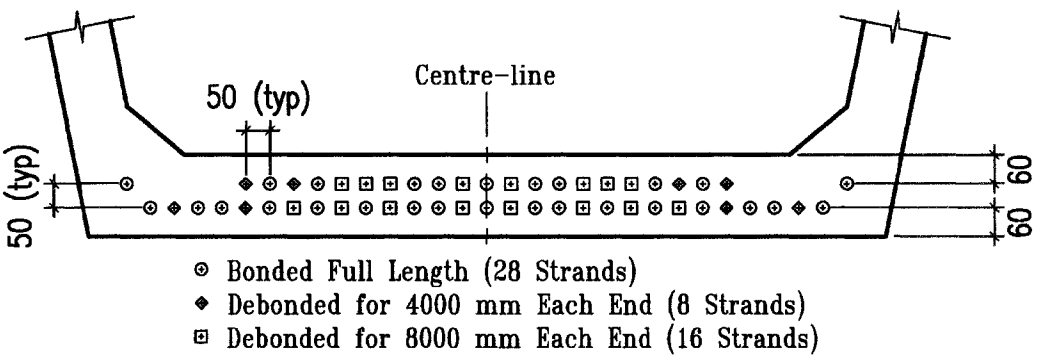

Figure 5.7: Pretensioned Strand Pattern – Design 2

5.4.5 Post-Tensioning

For Design 1, ducts are located inside the webs of the girder. Ducts are spliced through the pier diaphragm making the post-tensioning continuous over the length of the overpass. In the construction of the 130th and Deerfoot Trail overpass, tendons were tensioned from both ends simultaneously, and so for Design 1, simultaneous double-end stressing has been used. After stressing, the ducts are grouted.

For Design 2, the tendons are located outside the webs, but inside the box of the girder. Tendons are attached along the length of the girder at deviators, and at the ends at anchors. Due to minimal friction losses in external post-tensioning, sufficient stress levels in the tendons are obtained using alternate-end, single-end stressing.

Deviators consist of a bent steel pipe, cast into concrete. High-Density Polyethylene ducts that house the tendons are attached, using a sleeve, to the steel deviation pipe. After stressing, the ducts are grouted. This is done for corrosion protection and to create bond between the tendon and deviators.

Figures 5.8 and 5.9 show the tendon profile and section for Design 1 and Design 2 respectively. Note that for internal post-tensioning, the ducts must be stacked inside the webs, limiting the maximum eccentricity for each tendon. With the external post-tensioning design, the ducts can be located adjacent to one another, and all tendons can have the same eccentricity. The tendon profile for Design 1 was chosen using the method of load balancing. The magnitude of the post-tensioning force, and thus the number of tendons was chosen to satisfy the desired serviceability conditions (long-term camber and concrete stresses). The tendon profile for Design 2 was chosen to approximate the parabolic moment diagram resulting from Design 1. The number of tendons was chosen to satisfy the same desired serviceability conditions.

For Design 1, there are three tendons per web. Each tendon contains 9-15.2 mm diameter strands stressed to 79% of ultimate strength ($0.79f_{pu}$) at jacking, while for Design 2, there are two tendons per web, where each tendon contains 11-15.2 mm diameter strands stressed to 77% of ultimate strength ($0.77f_{pu}$) at jacking. These jacking stresses were chosen so that maximum tendon stress levels along the tendon would satisfy code requirements after lock-off.

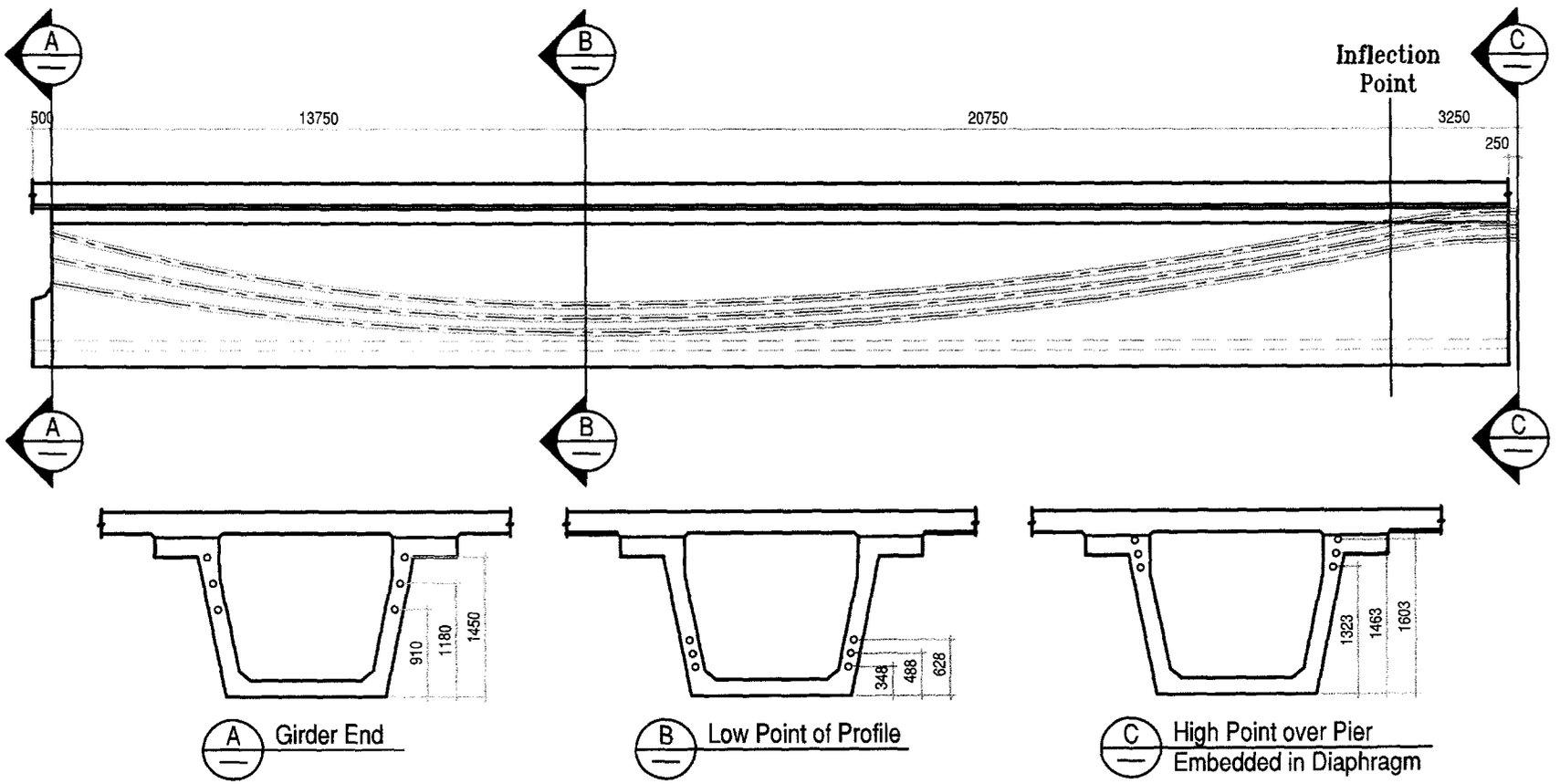

Figure 5.8: Internal Post-Tensioned Tendon Profile and Sections – Design 1

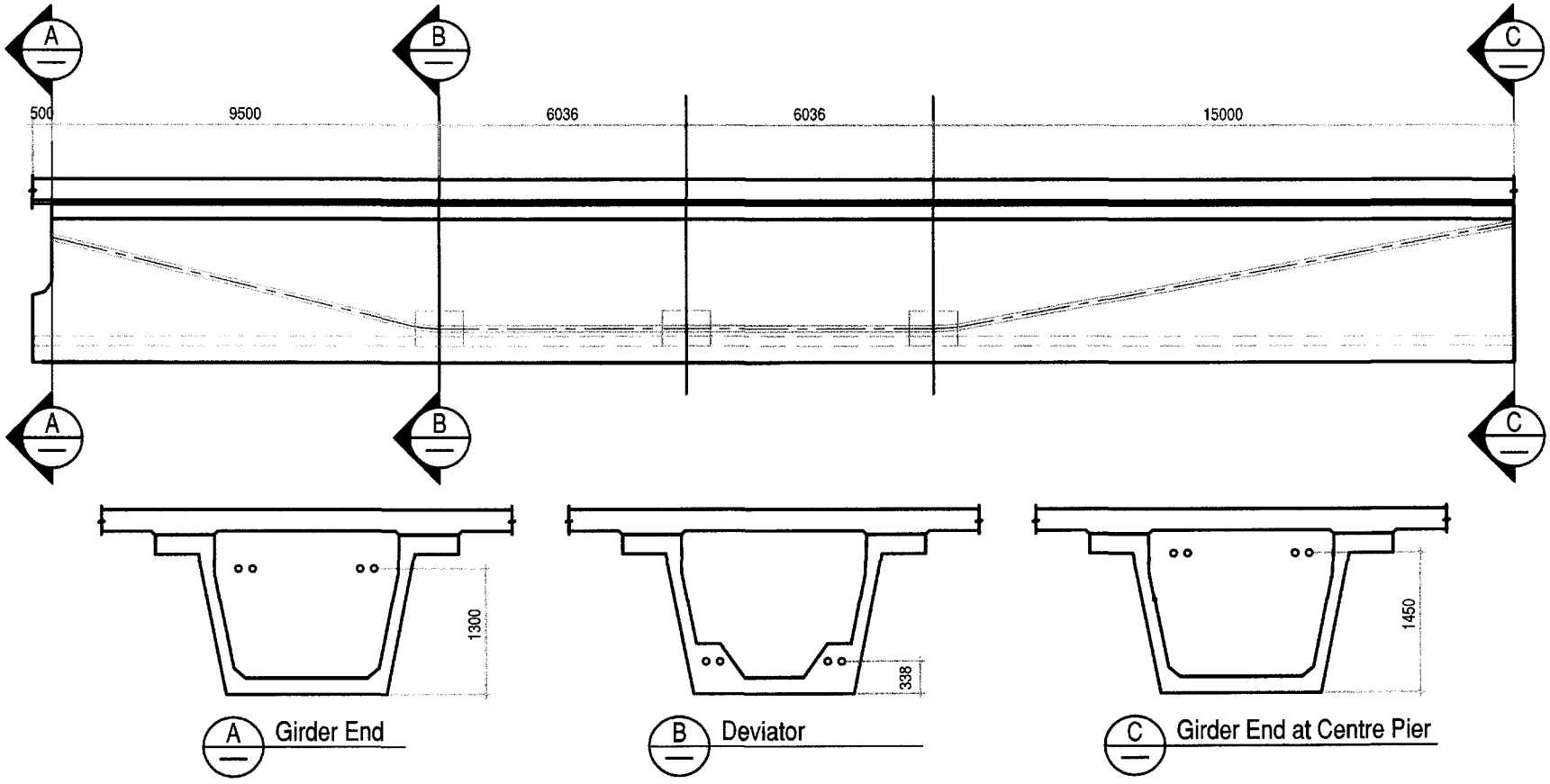

Figure 5.9: External Post-Tensioned Tendon Profile and Sections – Design 2

Friction losses in the tendons are calculated in accordance with the CSA S6-00. The tendon stress at jacking for internal tendons, accounting for friction and wobble along the length of the girder is calculated from:

$$f_p(x) = f_{po} e^{-(Kx+\mu\alpha)} \tag{5.1}$$

where $f_p(x)$ is the stress at location x, where x = 0 is at the jacking point, f_{po} is the jacking stress, K is the wobble coefficient accounting for unintentional angle changes along the length, and α is the cumulative intended angle change. The values chosen for these parameters for Design 1 are:

Wobble coefficient: K = 0.0033 / m
Coefficient of friction: μ = 0.20 / rad

For Design 2 the same equation is used, but between deviators the effect attributed to wobble does not occur because the tendon is unsupported and free of friction. The wobble coefficient and coefficient of friction for rigid steel pipe deviators are:

Wobble coefficient: K = 0.002 / m
Coefficient of friction: μ = 0.25 / rad

During construction, deviator misalignment will result in an unintentional angle change. With adequate care the pipe should be aligned within 5 mm per metre in a given plane, corresponding to 0.005 radians entering the deviator, and 0.005 radians exiting the deviator. Deviations of the pipe in the horizontal and vertical planes results in an unintentional angle change of 0.02 radians. This unintentional angle change is added to the intentional angle change, α, at each deviator. The length of end diaphragms is 1.0 m, the length of each deviator is 1.4 m, and the length of the pier diaphragm is 1.2 m.

The amount of anchorage set used in seating loss calculations is 8.0 mm.

Elastic shortening losses were included assuming that tendons are stressed one at a time.

Figure 5.10 shows the tendon stress averaged per girder line after frictional losses and anchor seating losses. For Design 1, this is equivalent to the stress for a single tendon, while for Design 2, it is equivalent to the average of two alternate-end, single-end stressed tendons.

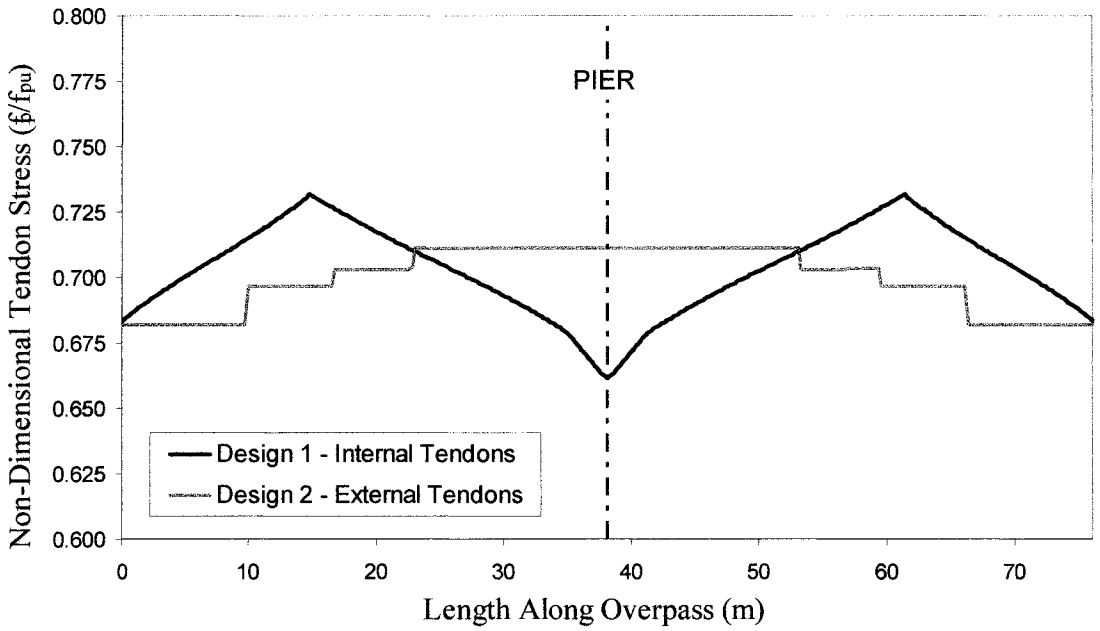

Figure 5.10: Tendon Stresses Used in Design, Averaged per Girder-Line, After Anchor Set and Elastic Shortening Losses

5.4.6 Section Properties

The transformed section properties are summarised in Table 5.6. Listed are the transformed section properties for the two girder designs at transfer, and for the composite section at 365 days.

Table 5.6: Transformed Section Properties

Cross-Section	Property	Units	Design 1	Design 2
Girder at Prestress Transfer t = 0.5 days	$E_{c\ girder}$	MPa	26600	
	A	mm^2	$1161x10^3$	$983.7x10^3$
	I_x	mm^4	$417.7x10^9$	$379.7x10^9$
	y_b	mm	759	749
Composite Section in Service t = 365 days	$E_{c\ girder}$	MPa	30600	
	$E_{c\ deck}$	MPa	32300	
	A	mm^2	$2199x10^3$	$2040x10^3$
	I_x	mm^4	$1006x10^9$	$948.8x10^9$
	y_b	mm	1262	1294

* Section properties are based on steel and deck concrete areas transformed to girder concrete

5.5 Results

The results presented include a comparison of response of the two designs at the limit states considered, a comparison of girder deflections, and prediction of the effects of tendon loss on Design 2. Required material quantities are also compared. Predictions are made using the Age-Adjusted Elastic Modulus Method, which is described in detail in Chapter 4.

5.5.1 Comparison of Concrete Stresses

Concrete stresses of the two designs are compared at the limit states TLS 1, TLS 2, and SLS 1.

5.5.1.1 Temporary Stresses

Figure 5.11 shows girder concrete stresses at TLS 1, corresponding to concrete stresses at prestress transfer and Figure 5.12 shows girder concrete stresses at TLS 2, corresponding to concrete stresses at the time of deck pour. Where applicable, the time-dependent effects of creep, shrinkage and prestress loss have been considered. In each case, two stress limits are shown: The compression and tensile limits as specified by CSA S6-00, which are applicable at transfer and during construction. As well, the cracking strength is shown.

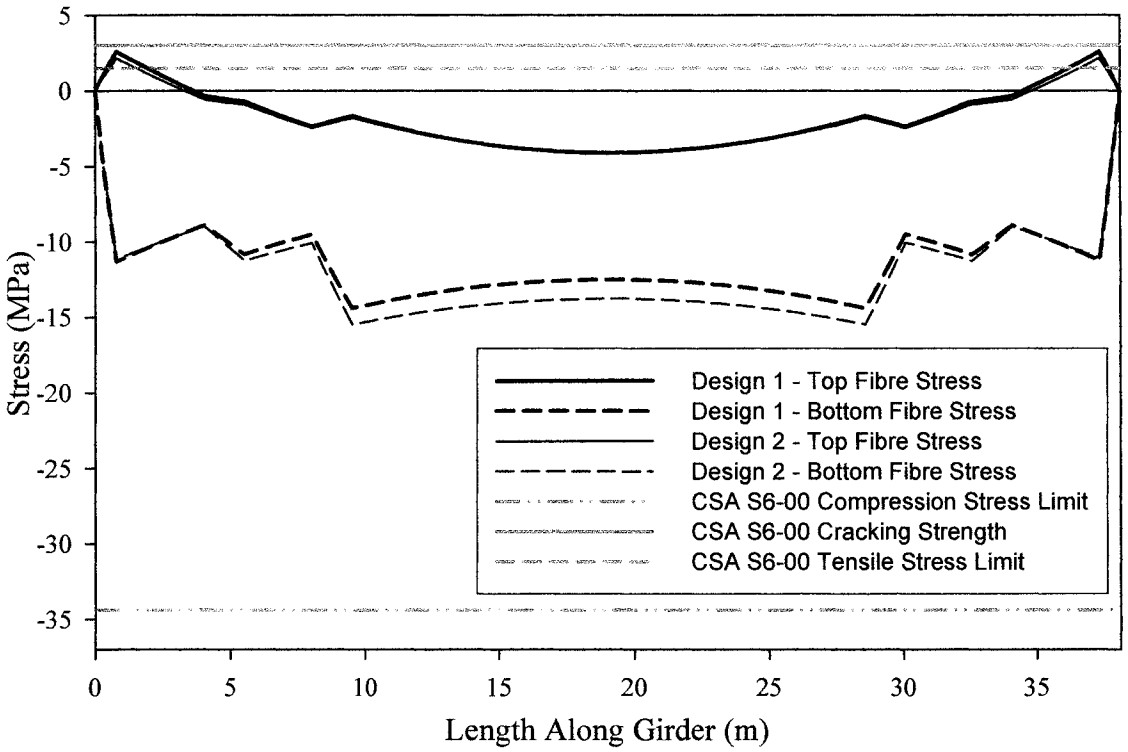

Figure 5.11: Girder Concrete Stresses at Transfer (TLS 1)

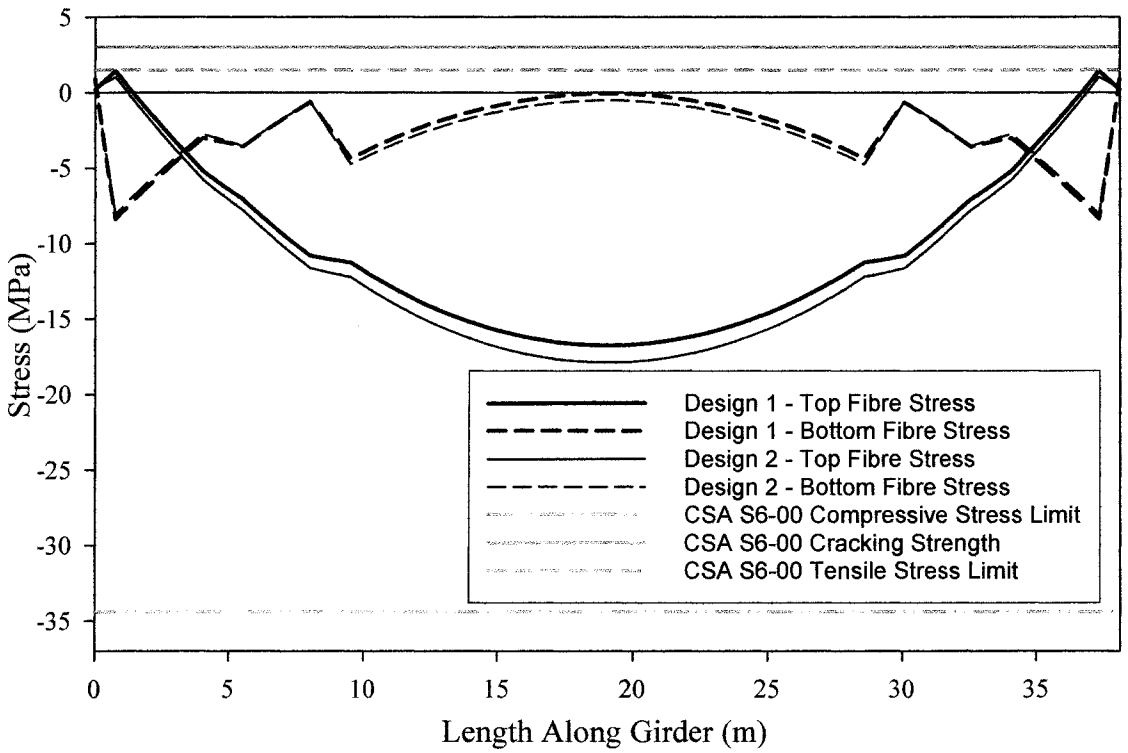

Figure 5.12: Girder Stresses at Deck Pour (TLS 2)

5.5.1.2 Service Stresses

Figures 5.13 through 5.18 show the girder and deck concrete stresses. Figures 5.13 and 5.14 show the girder and deck concrete stresses at SLS 1 without the live load, Figures 5.15 and 5.16 show the stresses at SLS 1 with the maximum positive service moment combination, and Figures 5.17 and 5.18 show the stresses at SLS 1 with the maximum negative service moment combination. The time-dependent effects of creep, shrinkage and prestress loss are considered. It should be noted that in the calculation of extreme fibre stresses shear lag was ignored. The transfer length and shear lag effects are isolated to the ends where the prestressing force is introduced. Thus, at the girder ends, calculated stresses may not be representative of real behaviour.

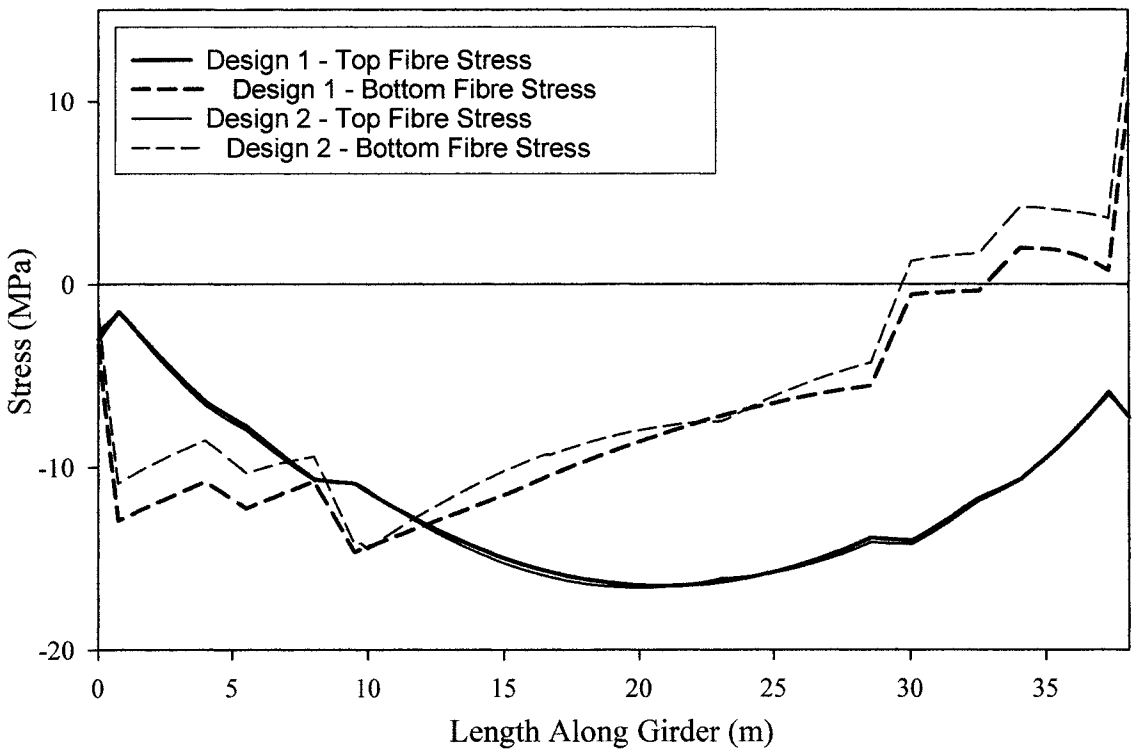

Figure 5.13: Girder Concrete Stresses at 365 Days Due to Sustained Loads

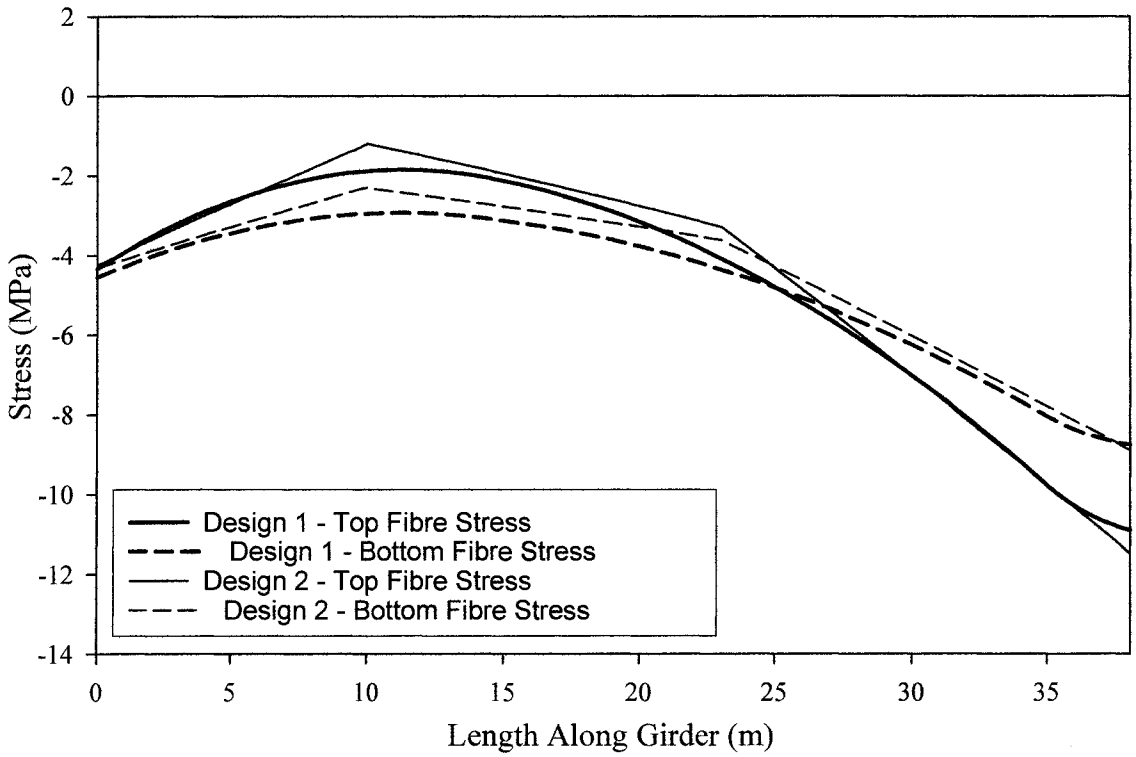

Figure 5.14: Deck Concrete Stresses at 365 Days Due to Sustained Loads

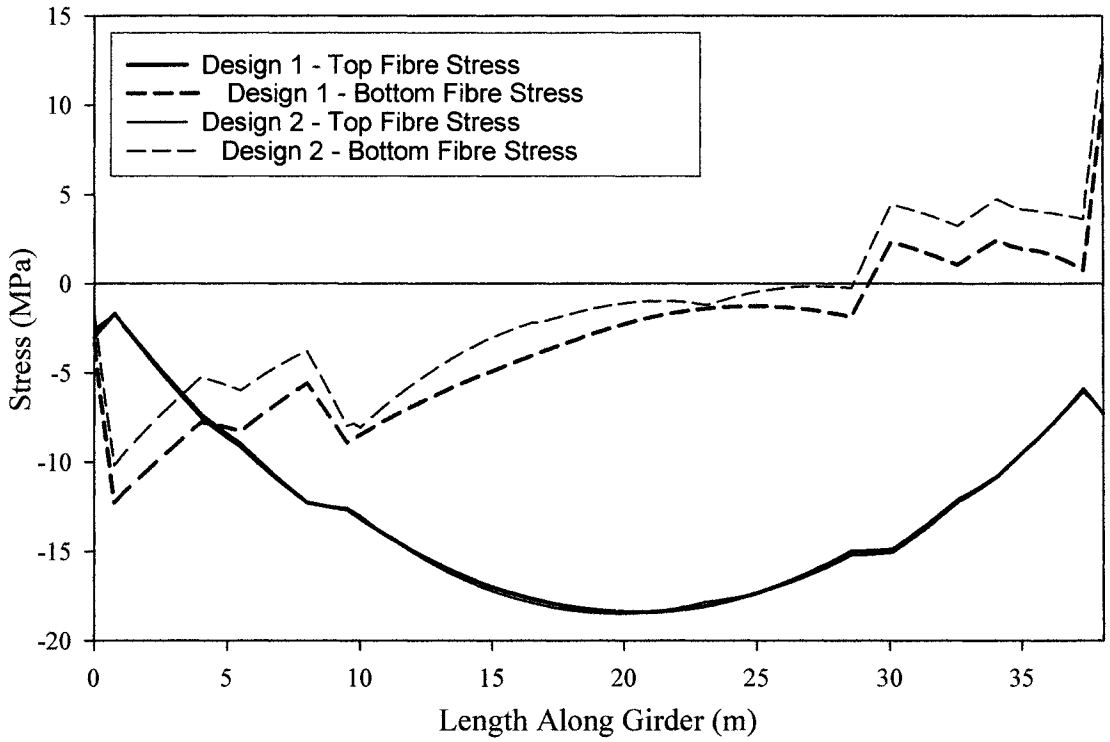

Figure 5.15: Girder Concrete Stresses at 365 Days Due to Maximum Positive Service Moment Combination

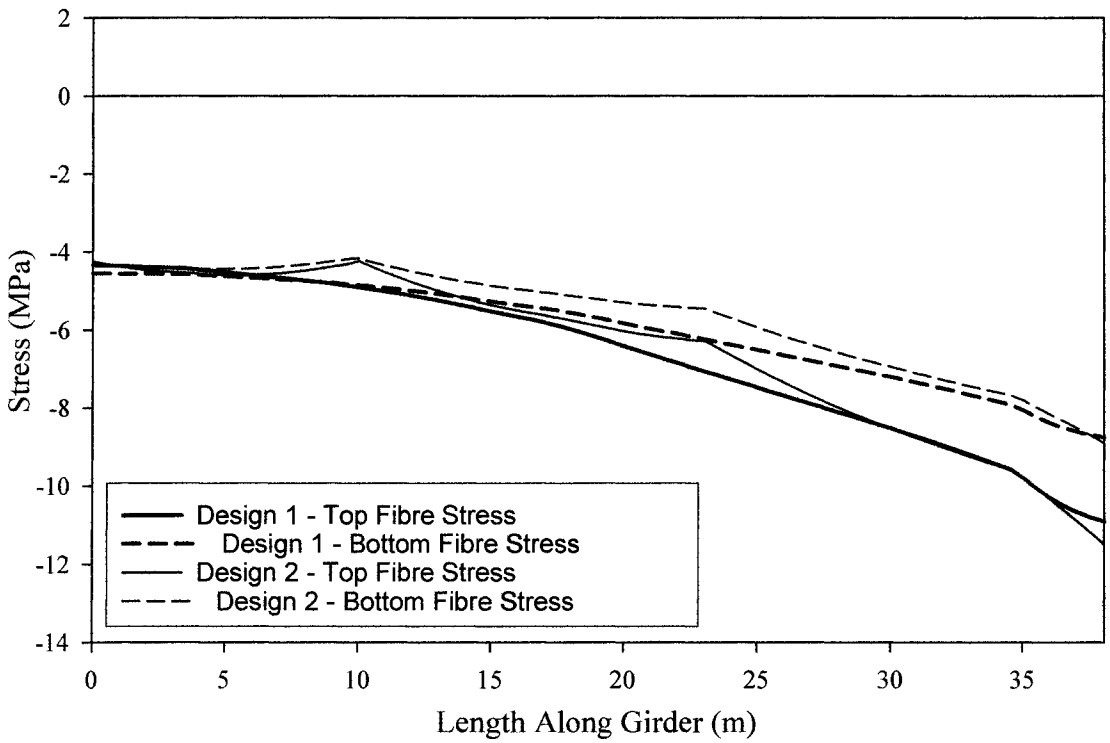

Figure 5.16: Deck Concrete Stresses at 365 Days Due to Maximum Positive Service Moment Combination

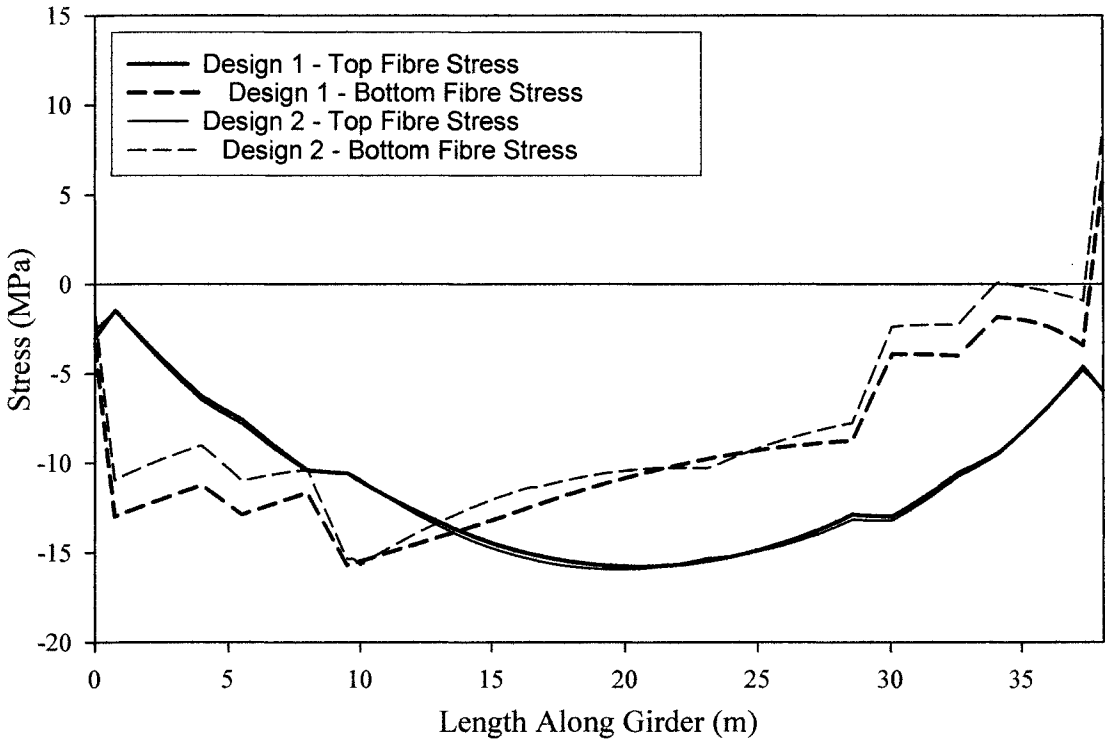

Figure 5.17 Girder Concrete Stresses at 365 Days Due to Maximum Negative Service Moment Combination

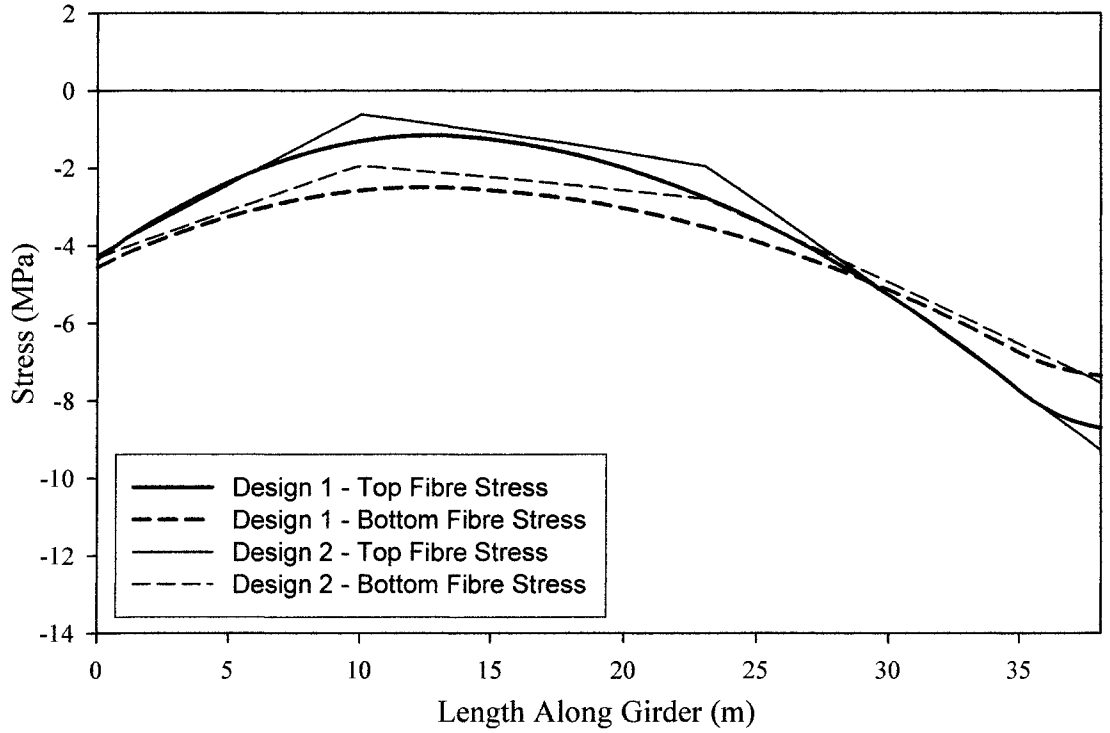

Figure 5.18: Deck Concrete Stresses at 365 Days Due to Maximum Negative Service Moment Combination

5.5.2 Deflection with Time

The Age-Adjusted Elastic Modulus Method was used to predict time-dependent deflections due to sustained loads, changes in loading conditions and changes in static conditions. Figure 5.19 shows the mid-span deflection of the girders for one year due to sustained loads. The load history uses the events summarised in Table 5.4. At the design life of 75 years, Design 1 girders are estimated to have a mid-span camber of 10.1 mm and the Design 2 girders are estimated to have a mid-span camber of 10.7 mm.

The mid-span service live load deflection is 24.7 mm for Design 1 and 26.2 mm for Design 2. In other words, the live load deflection for Design 1 corresponds to L/1500 while the live load deflection for Design 2 corresponds to L/1450.

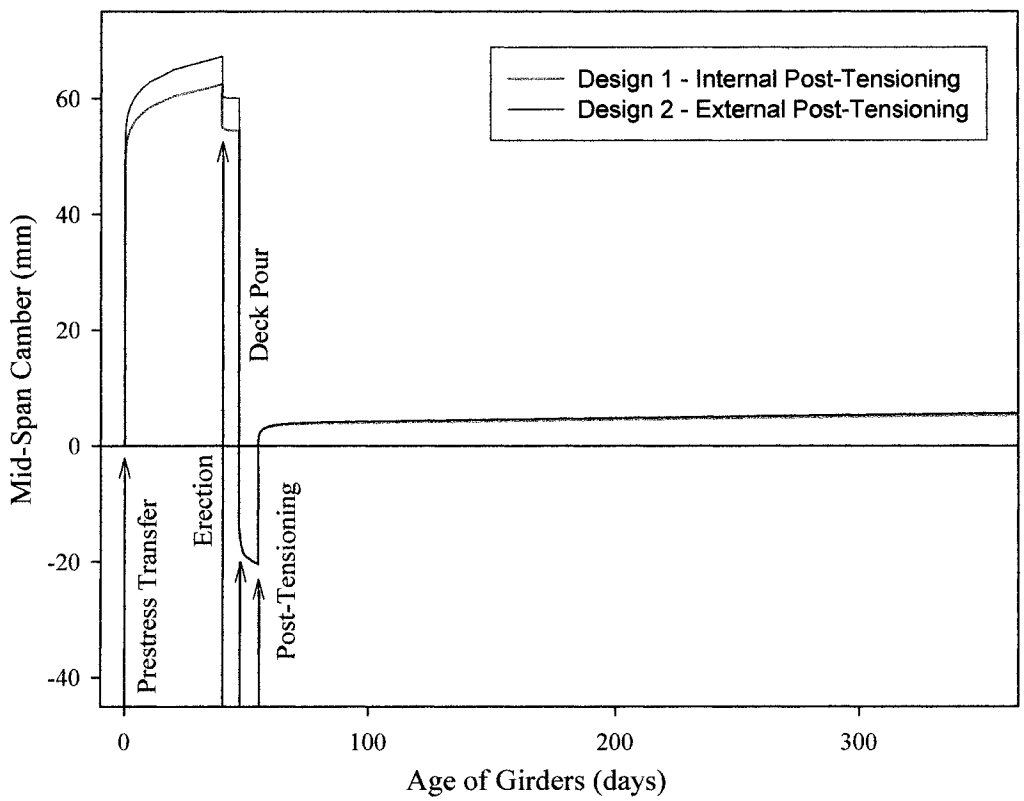

Figure 5.19: Mid-Span Camber Due to Sustained Loads

5.5.3 Comparison of Ultimate Capacity

Ultimate capacities of the two designs are compared at ULS 1.

5.5.3.1 Factored Moment Resistance

Ultimate moment capacity was calculated in accordance with CSA S6-00, which is based on the usual assumptions for flexural theory of concrete members. The only variation made is in the calculation of tendon stress at ultimate. For bonded tendons, CSA S6-00 provides an approximate equation for stress increase at ultimate. Herein, strain compatibility is used to determine tendon stress increase for Design 1.

In Chapter 2 it is shown that the stress increase in unbonded tendons at ultimate is different than for bonded tendons, and in certain circumstances, the stress increase in external tendons at ultimate is different than for interior unbonded tendons. It is also shown in Chapter 2 that the use of a deviator at mid-span will, for all practical purposes, eliminate second-order effects associated with the loss of tendon eccentricity sufficiently. In this case the externally post-tensioned beam behaves similar to an internal post-tensioned unbonded beam. In Design 2, the externally unbonded tendon stress increase is calculated using two different methods: CSA S6-00 and AASHTO (1998). In these methods the external tendon stress is limited to its yield stress. Sample calculations of moment resistance are summarised in Appendix C.

Figure 5.20 and 5.21 show the composite cross-sections and flexural steel reinforcement for Design 1 and Design 2 respectively. Table 5.6 summarises the area and vertical height of the non-prestressed flexural steel, which was the same for both Designs. As well, Figures 5.20 and 5.21 show the strain distribution at ultimate for the two designs at the mid-span section calculated in accordance with CSA S6-00. Figures 5.22 and 5.23 show the factored moment resistance, cracking moment, and the factored applied moment for positive moments in Design 1 and Design 2 respectively. For Design 2 the factored moment resistance is calculated using CSA S6-00 and AASHTO (1998). Similar

analyses were done for negative moments, but it is not shown because it adds no new information.

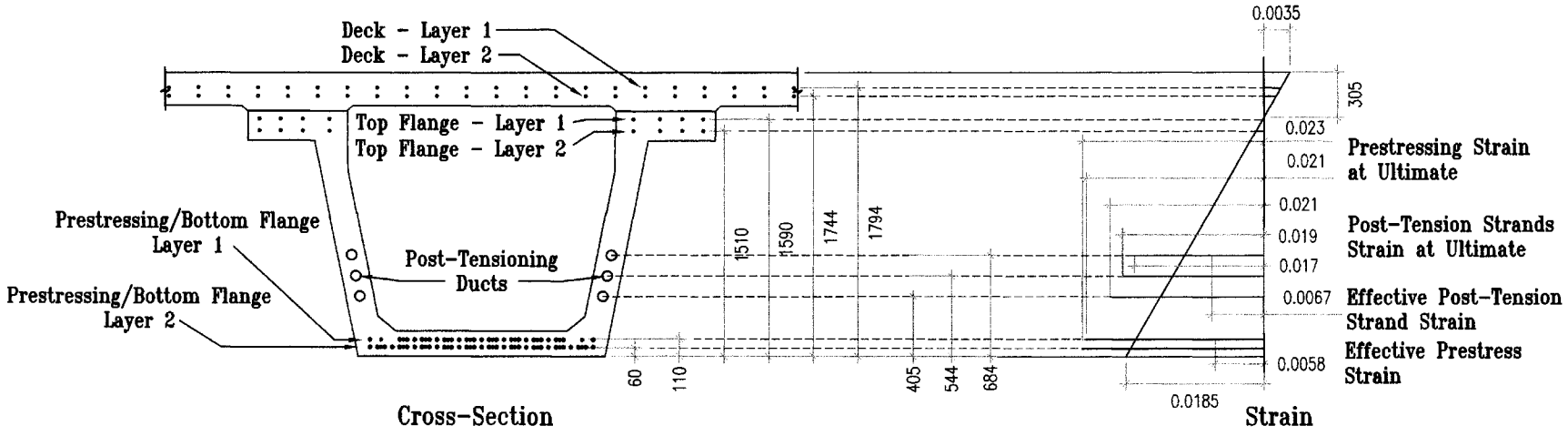

Figure 5.20: Flexural Steel Layout and Strain Distribution at Ultimate at Mid-Span Section – Design 1

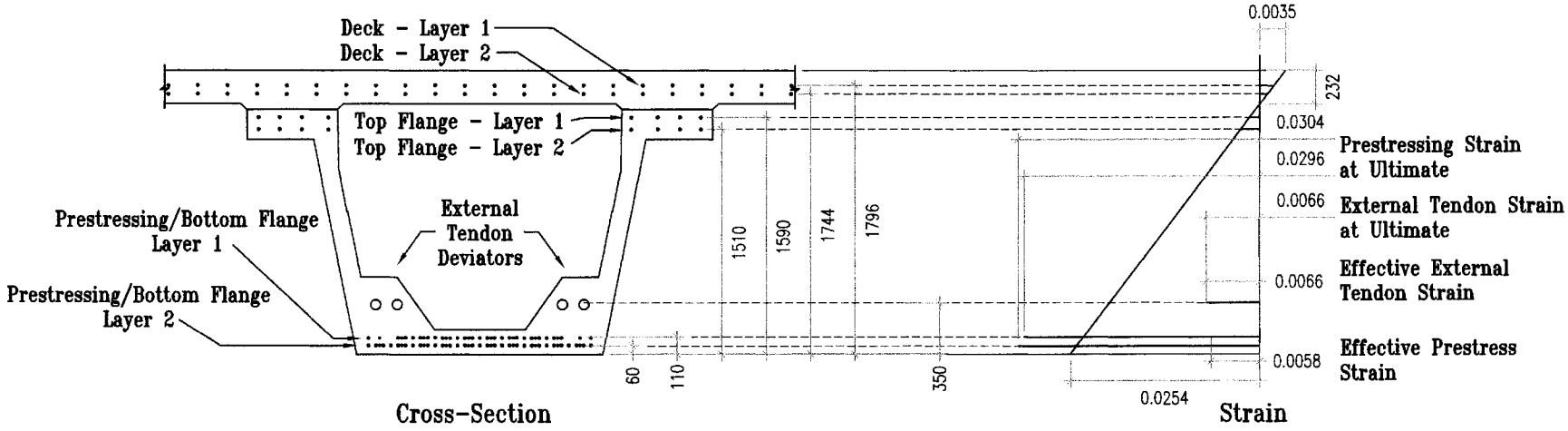

Figure 5.21: Flexural Steel Layout and Strain Distribution at Ultimate at Mid-Span Section Calculated using CSA S6-00 – Design 2

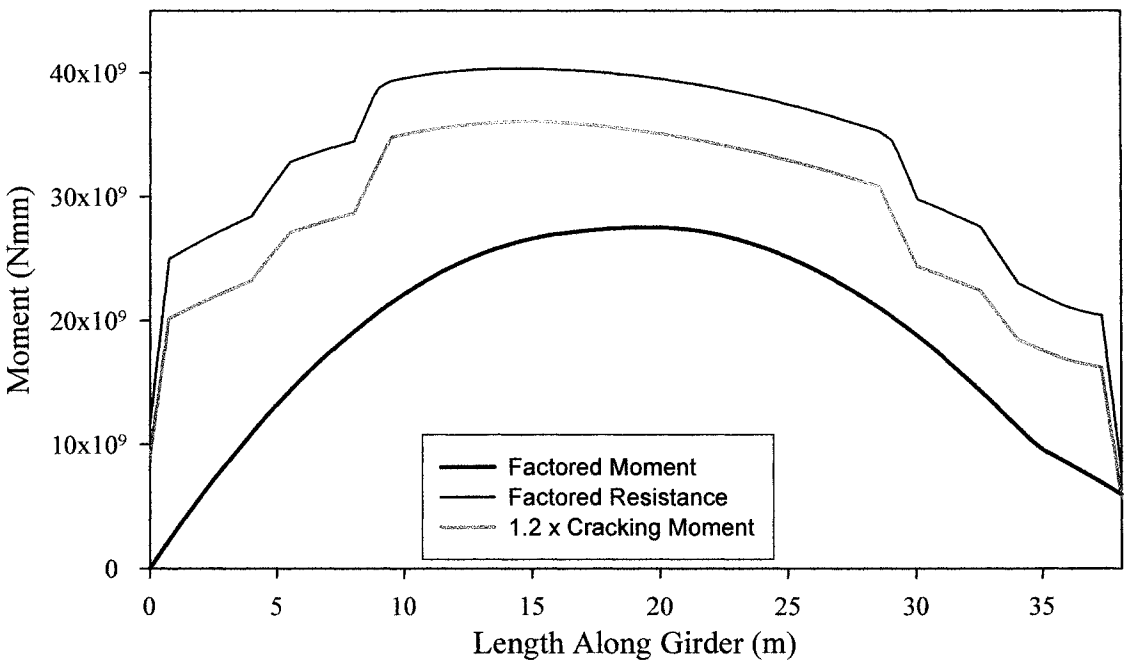

Figure 5.22: Design 1 Factored Moment Resistance

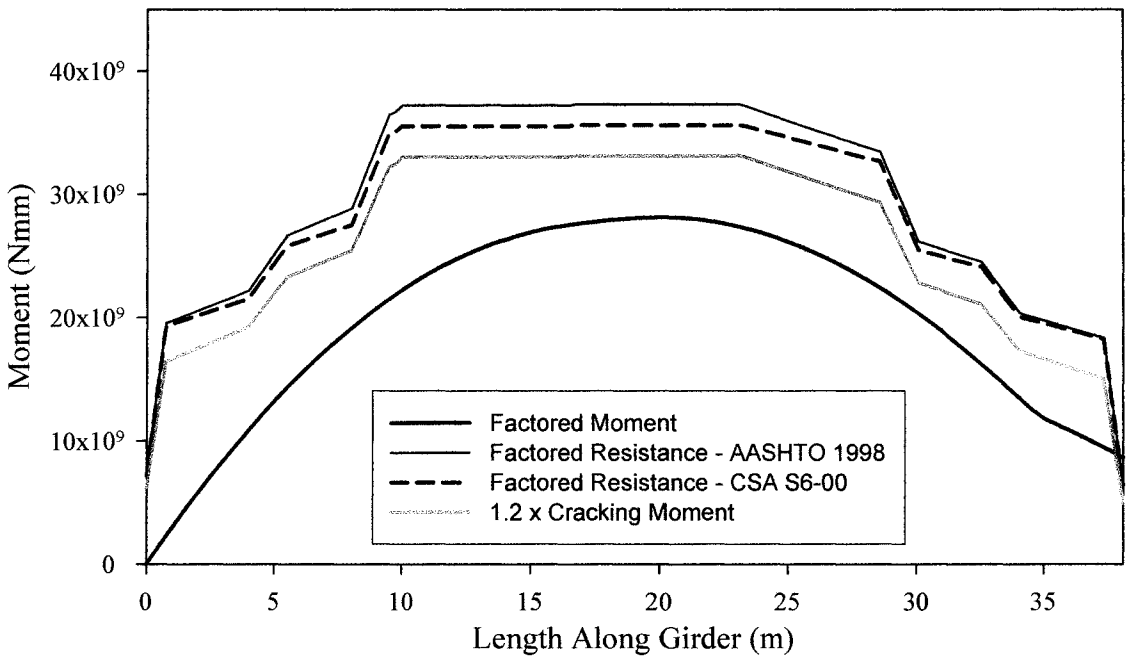

Figure 5.23: Design 2 Factored Moment Resistance

5.5.3.2 Factored Shear Resistance

The ultimate shear capacity is calculated using CSA S6-00. Differences between the designs are discussed below. The factored shear resistance, V_r, is calculated from the following equation:

$$V_r = V_c + V_s + \phi_p V_p \tag{5.2}$$

where V_c is the factored concrete contribution, V_s is the factored shear reinforcement contribution, ϕ_p is the material resistance factor for prestressing steel, and V_p is the vertical component of the prestressing steel.

One factor affecting the concrete contribution is the effective web width, b_v. The effective web width is the minimum web width within the shear depth. For webs with internal grouted ducts, one half the diameter of the ducts is subtracted from the minimum web width. Thus, for Design 1 with 75 mm ducts, b_v = 142 mm, while for Design 2 b_v = 125 mm. Even though the web thickness was reduced by 55 mm for Design 2, the effective web width used in shear calculations was only reduced by 17 mm.

Another factor that affects the factored shear resistance is the post-tensioning contribution. With the internal post-tensioning, the vertical component of prestressing varies. But with external post-tensioning the tendon inclination is constant, and relatively large in regions where the shear demand is greatest.

The factored shear resistance of both designs is shown in Figure 5.24 along with the factored shear force.

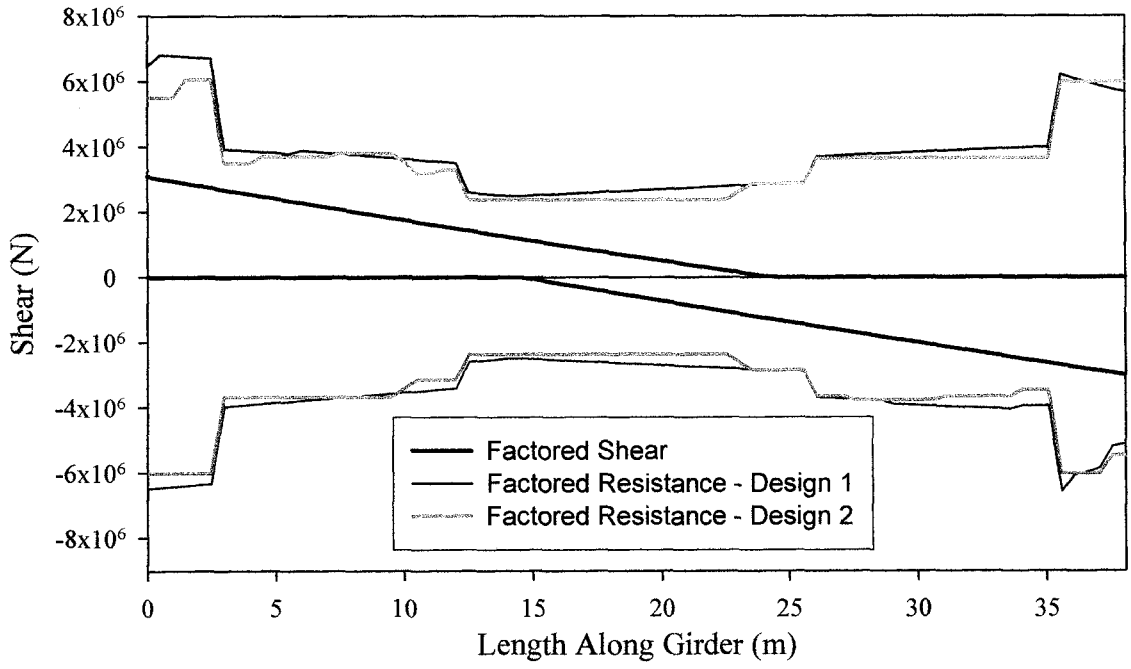

Figure 5.24: Applied Shear and Factored Resistance

5.5.4 Effects of Loss of External Tendons

To investigate the safety of Design 2, the effects resulting from the loss of external tendons were investigated. For this design, the external tendons are inside the box of the trapezoidal girder offering protection from the environment and making them less vulnerable to potential sabotage or impact damage. An adequate corrosion protection system supplemented with visual observation can ensure excellent performance of the tendons throughout the service life. However, because of the nature of external tendons, any local damage or deterioration of will cause loss of the tendon throughout its entire length. For this reason, the effects resulting from the loss of a tendon are considered. Each external tendon consists of 11-15.2 mm diameter strands.

The effects of tendon loss on service stresses, ultimate moment capacity and ultimate shear capacity are considered. To simplify the analysis, dynamic behaviour from the sudden release of tendon force and horizontal eccentricity of tendon force are not considered.

5.5.4.1 Effect on Concrete Stresses

The effect of tendon loss on girder concrete stresses is shown in Figure 5.25. The loss of an external tendon causes a loss in compression along the bottom fibre, and as a result, portions of the girder can end up experiencing tensile stresses. As well, the loss of external tendons results in a loss in upward camber of the beam. For each tendon that is lost, there is approximately 7.3 mm of elastic camber loss, if the section is assumed to remain uncracked. If the section cracks, the stiffness of the section will decrease, resulting in a greater loss of camber. With sequential loss of external tendons, there will be visible cracking and deflection giving warning prior to structural failure.

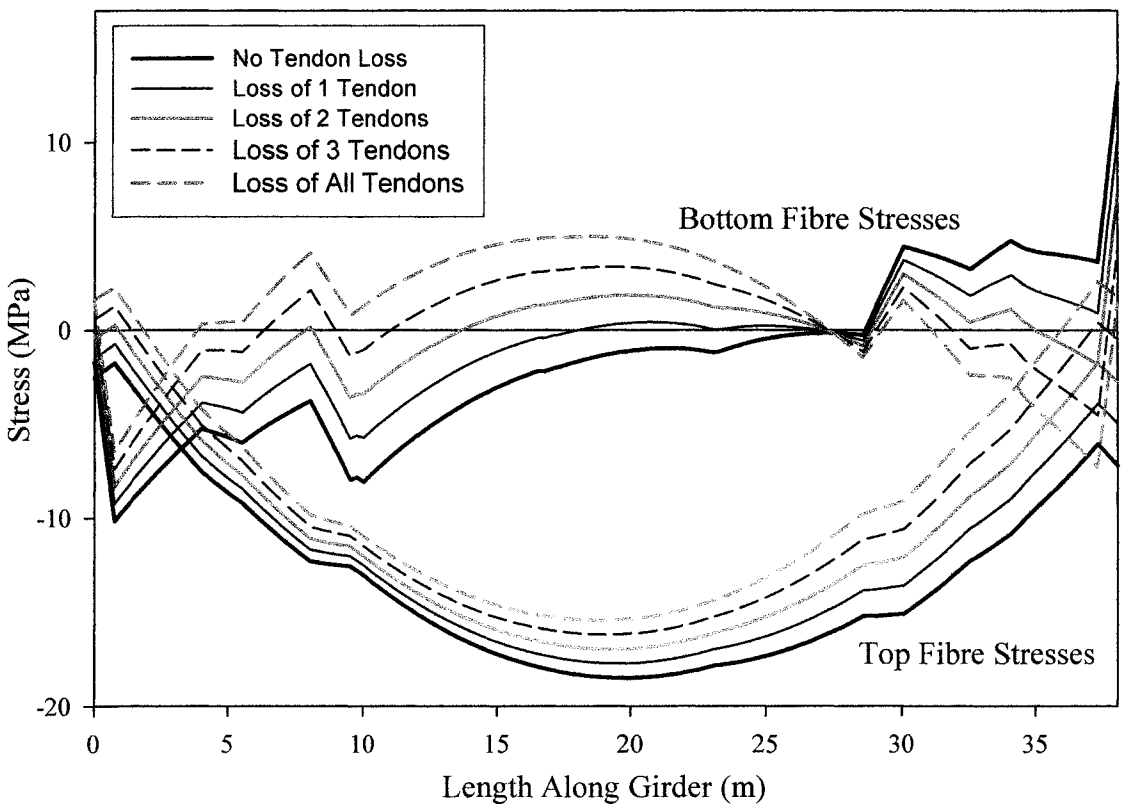

Figure 5.25: Effect of Tendon Loss on Girder Concrete Stresses Due to Maximum Positive Service Moment Combination for Design 2

The effect of tendon loss on deck concrete stresses is shown in Figure 5.26. The loss of an external tendon results in a loss in deck concrete compression. With the application of the maximum negative service moment combination portions of the deck can experience tensile stresses.

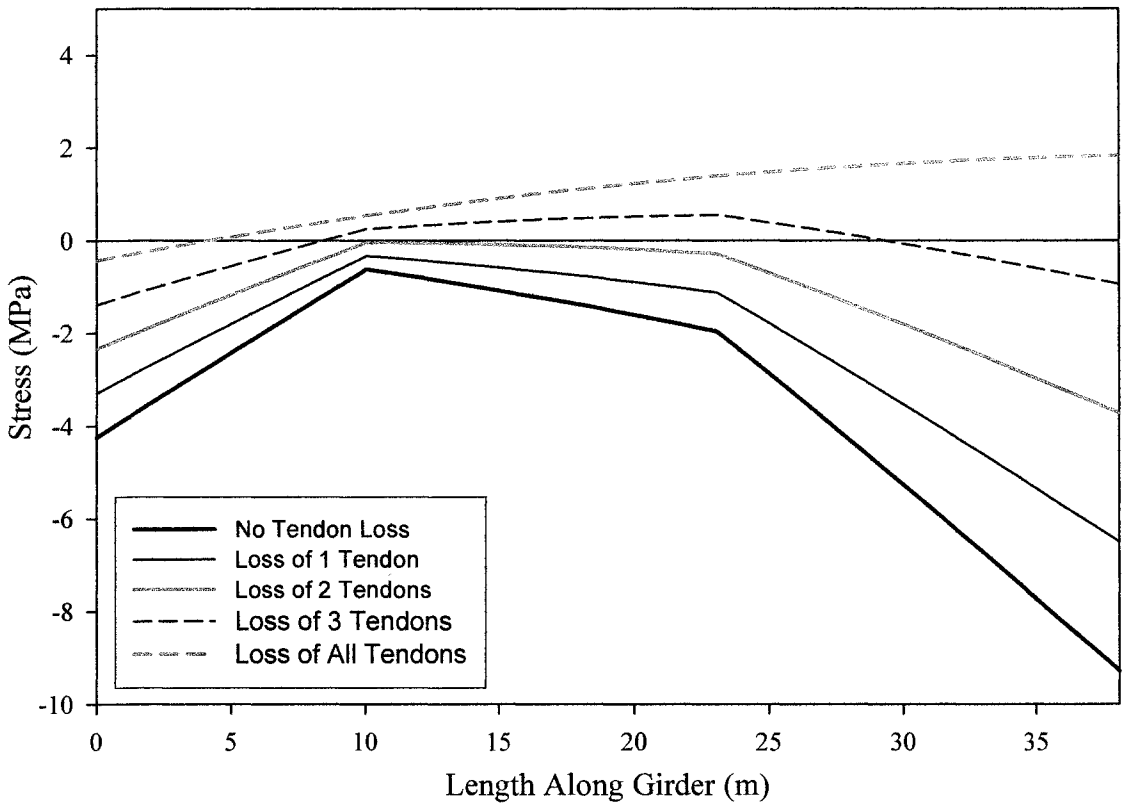

Figure 5.26: Effect of Tendon Loss on Deck Concrete Top Fibre Stress Due to Maximum Negative Service Moment Combination for Design 2

5.5.4.2 Effect on Ultimate Flexural Capacity

Figure 5.27 shows the effect of tendon loss on the ultimate moment capacity of the overpass. The predictions were made using AASHTO (1998) recommendations. The loss of each tendon reduces the moment capacity by approximately 8 percent.

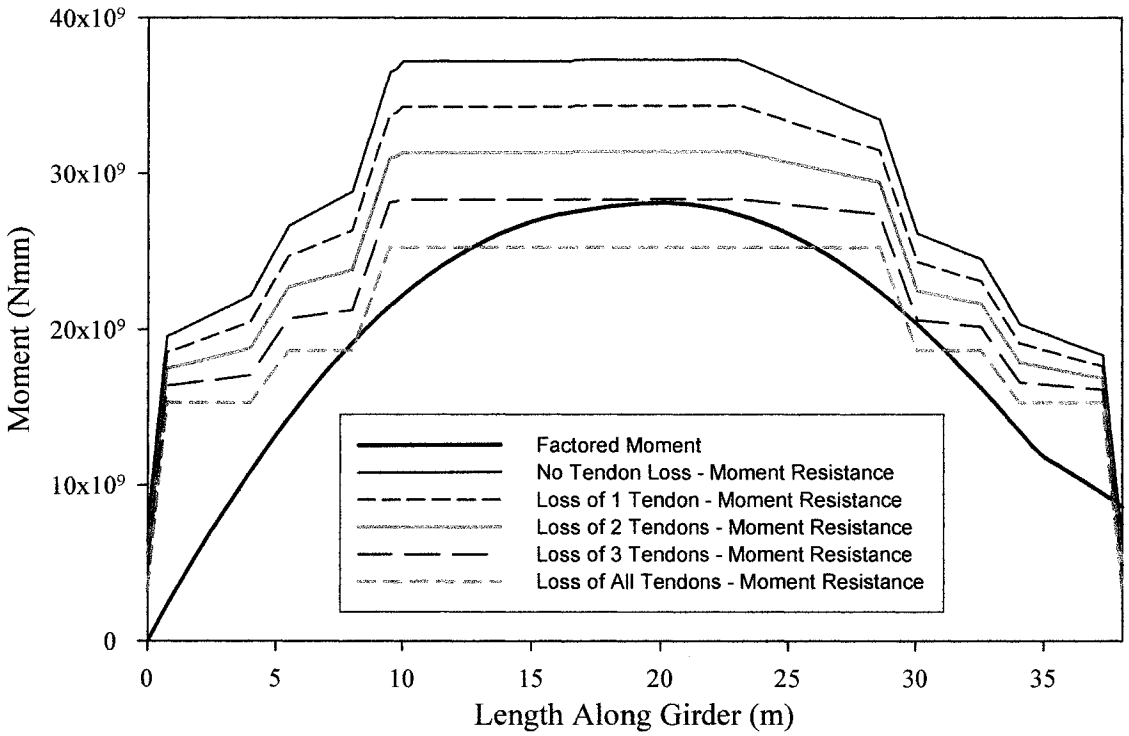

Figure 5.27: Effect of Tendon Loss on Moment Resistance for Design 2 Calculated Using AASHTO (1998)

5.5.4.3 Effect on Shear Capacity

Figure 5.28 shows the effect of tendon loss on shear resistance of the overpass. It shows that the external tendons provide little contribution to the shear resistance.

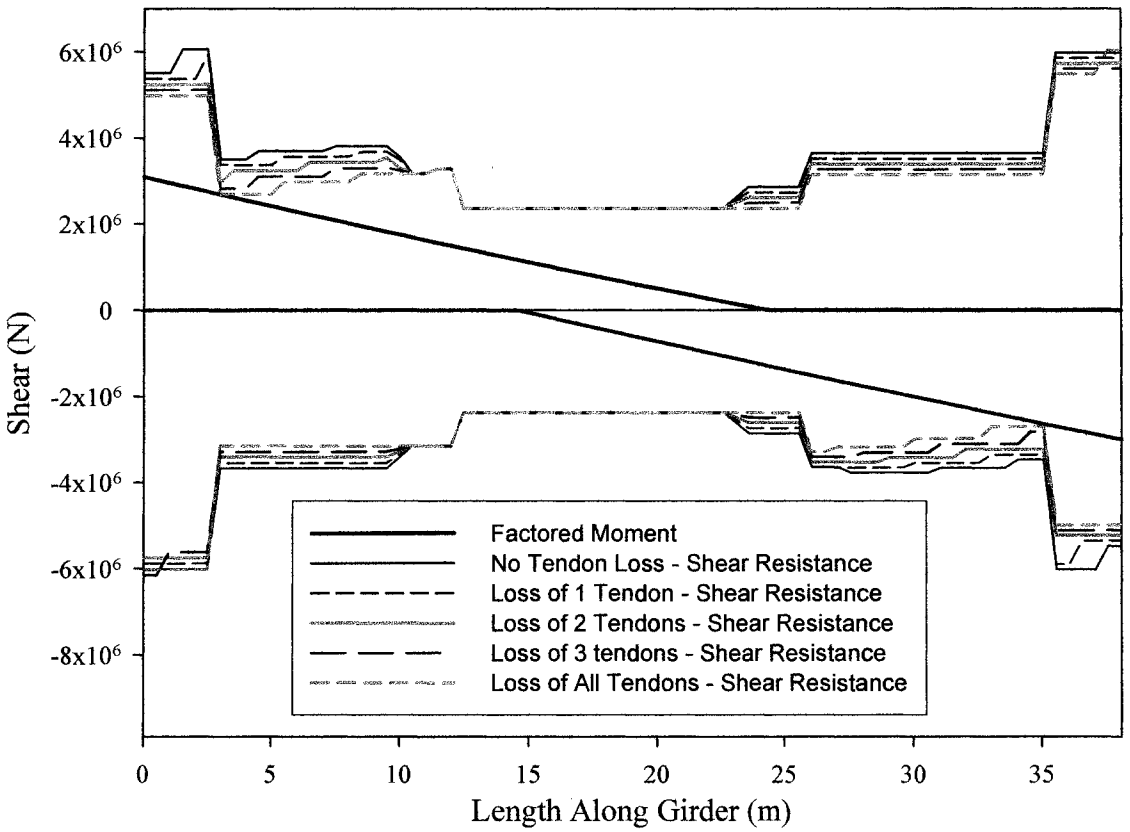

Figure 5.28: Effect of Tendon Loss on Shear Resistance for Design 2

5.6 Discussion

Comparison of Design Details

Figures 5.2 and 5.3 show the different sections used in design. The girder used in Design 1 had internal ducts, and the larger web thickness, while the girder used in Design 2 had no internal ducts and a smaller web thickness. The section used in Design 2 had a self-weight 15% less than that used in Design 1, and a 15% reduction in girder concrete volume required.

Figures 5.6 and 5.7 show the pre-tensioned strands. Design 1 had 55 strands in total, while Design 2 had 52 strands in total. Thus Design 2 had 5.5% less pre-tensioned strand. The reduced self-weight of the Design 2 girder required fewer strands to deal with the applied dead loads and achieve the same performance after deck pour. Both Design 1 and Design 2 have similar stresses at transfer (Figure 5.11) and at deck pour (Figure 5.12).

Figures 5.8 and 5.9 show the post-tension profiles for the two designs. In the internal post-tension design, it is noted that the ducts are stacked in the web. For this case, the minimum clear space between ducts is 65 mm, resulting in a centre-of-duct to centre-of duct spacing of 140 mm. In effect, the maximum eccentricity, and effectiveness of the tendons are limited, giving a maximum possible drape for the internal post-tensioning of 1000 mm. In contrast, for the external post-tension design, the tendons can be placed side-by side with the same eccentricity, giving a maximum possible drape for the external post-tensioning of 1325 mm. It should be noted that the externally post-tensioned design did not take full advantage of the available drape, so there is scope for further design refinement and improved material savings.

Figure 5.10 shows tendon stresses after anchor set. It is seen, that because of minimal friction losses in external post-tensioning, sufficient stress levels in the tendons can be obtained using alternate-end, single-end stressing. This represents a 67% reduction in number of jack pulls. For Design 1 with simultaneous stressing, an average tendon stress

of $0.705f_{pu}$, is obtained, while for Design 2 with alternate-end, single-end stressing an average tendon stress of $0.708f_{pu}$ is obtained.

The post-tensioning design for the internal tendons (Design 1) used 9-15.2 mm diameter strands per duct, with 3 ducts per web giving 54 strands in total. The external post-tensioning design (Design 2) used 11-15.2 mm diameter strands per duct, with 4 ducts giving 44 strands in total. This represents a 33% reduction in the number of post-tensioning anchorages and an 18.5% reduction in post-tensioning strand tonnage required. This reduction in the required number of strands can be attributed to a greater average eccentricity for all the strands, combined with a slightly reduced dead load.

Comparison of Concrete Stresses

Figures 5.11 and 5.12 show that at the temporary limit states considered, all concrete stresses are satisfactory. It was noted that at transfer near the girder ends, the recommended tensile limit is slightly exceed, so cracking may occur. This was deemed not to be of major concern because any cracks will close from the deck weight, and be subsequently protected against water by the deck. As well, sufficient flexural steel in the top flanges of the box section was provided for crack control.

Figures 5.13 through 5.18 show the girder and deck concrete stresses at SLS 1. As a result of post-tensioning, both designs develop tensile stresses in the girder's bottom fibre over the pier. In a complete design, the cracks would be controlled with reinforcing steel and there would be a positive moment connection over the pier.

For the stress states resulting from SLS 1, Design 1 girder concrete stresses range from a maximum compression of 18.4 MPa to a maximum tension of 10.0 MPa and Design 1 deck concrete stresses range from a maximum compression of 10.9 MPa to a minimum compression of 1.2 MPa. For Design 2, girder concrete stresses range from a maximum compression of 18.5 MPa to a maximum tension of 13.7 MPa and deck concrete stresses range from a maximum compression of 11.5 MPa to a minimum compression of 0.6 MPa. All concrete stresses are satisfactory at SLS 1. In both designs, the deck concrete

would remain uncracked throughout the design life, while tensile stresses and cracking in the girder would be isolated to a small section of the bottom flange over the centre pier.

Comparison of Camber Predictions

Deflections due to SLS 1, were calculated for both designs at one year of age. For Design 1, the live load deflection was 24.7 mm, which corresponds to $\Delta/L = 1/1500$. For Design 2, the live load deflection was 26.2 mm, which corresponds to $\Delta/L = 1/1450$. The small difference can be attributed to the slightly reduced stiffness of Design 2.

Figure 5.19 shows how the mid-span camber of the girders changes with time due to sustained loads. It can be seen that the Design 2 girders are more flexible than the Design 1 girders before composite action begins. However, after the deck hardens and the system becomes composite, the responses become very similar. Time-dependent deflections after post-tensioning appear to be nearly identical.

Comparison of Ultimate Behaviour

For ultimate behaviour, the flexural designs used identical non-prestressed steel layouts. Figures 5.20 and 5.21 show the strain distribution at ultimate at the mid-span section for the designs. In the calculation of ultimate moment capacity of the internal post-tensioned design, strand strain increases up to section failure. In the calculation of the ultimate moment capacity of the external post-tensioned design two methods were used to predict strain increase in the eternal strands. The first method used CSA S6-00, where without a more detailed analysis, the external strands are assumed to not increase in strain. The second method used AASHTO (1998) which allows for an increase in strand stress at ultimate. By comparing Figures 5.22 and 5.23, it is noted that the factored moment resistance of Design 1 is greater than that of Design 2. This can be attributed to the available stress increase of the internally bonded post-tensioning strands and the greater total area of post-tensioning tendons. Both designs are found to adequately resist the applied factored moment. Figure 5.23 shows AASHTO 1998 recommendations predict a moment capacity 4% greater than predicted using CSA S6-00.

Figures 5.4 and 5.5 show the shear reinforcement layouts for both designs. For Design 1 two layers of shear reinforcement were used, while for Design 2 only one layer was used. This results in a simpler cage to fabricate and install for Design 2, while maintaining the same area of shear steel, because the spacing used in Design 2 is half of the spacing in Design 1. As well, because Design 2 web widths were not governed by cover requirements, a greater clear concrete cover for the shear reinforcement is obtained. Figure 5.24 shows the factored shear resistance of the two designs, and it is noted that there is little difference in the resistance. Both are adequate in resisting the applied factored shear.

Effect of Tendon Loss

The final consideration in this investigation is the effect of tendon loss on the behaviour of the externally post-tensioned overpass. The three behaviours considered are girder service stresses, ultimate moment capacity and ultimate shear capacity. Figures 5.25 and 5.26 show the effect of tendon loss on service stresses. It is seen that the loss of two tendons is required to put a significant portion of the girder bottom fibres into tension. And a loss of three tendons is required to put the deck top fibres into tension. However, the effect of dynamic behaviour is not considered, and the sudden loss of one tendon could possibly cause cracking.

Figure 5.27 shows the effect of tendon loss on ultimate moment capacity. It is seen that it requires the loss of three tendons for the factored resistance to approach the ultimate factored moment.

Figure 5.28 shows the effect of tendon loss on ultimate shear capacity. Here it is seen that the external post-tensioning provides minimal contribution to the shear capacity of the overpass. The loss of all tendons does not lead to shear failure. Thus, flexural failure would occur before a shear failure.

5.7 Summary and Conclusions

An analytic study was performed to assess the practicality of external post-tensioning in highway overpass design. Two designs of a highway overpass were compared. The first was done using internal post-tensioning, as is standard, while the second used external post-tensioning. To allow for an unbiased comparison, the two overpasses were designed to have similar behaviours in terms of stresses, deflections and ultimate resistance.

Previous studies presented in Chapter 3 and Chapter 4 showed that an accurate prediction of behaviour for the traditional internally post-tensioned overpass could be performed using the analysis procedure presented. Through the use of this procedure, and with supplemental recommendations for ultimate behaviour, the behaviour of the two designs was studied.

From the results of this study, the following differences between the design using internal tendons and the design using external tendons are noted.

- With the externally post-tensioned structure, the elimination of ducts in the webs is possible, allowing for a thinner web width. This resulted in a lighter concrete section with 15% less girder concrete and 5.5% fewer pre-tensioned strands.
- The friction losses in tendon stress occurring during stressing of the post-tensioning were greater for the internally post-tensioned overpass than the externally post-tensioned overpass. This is attributed to the increased duct friction resulting from the inherent wobble associated with internal post-tensioning.
- The reduced friction losses in external post-tensioning allowed sufficient stress levels in the tendons to be obtained using alternate-end, single-end stressing and thereby reducing the number of jack set-ups by 67%.
- With internal post-tensioning, the ducts are stacked in the webs, with specified spacing between ducts. With three ducts per web, the maximum possible drape for the internal post-tensioning is 1000 mm. With external post-tensioning, the

tendons can be located side by side and extend from the top of the bottom flange to the soffit of the deck. For this design the maximum possible drape for the external post-tensioning is 1350 mm.

- The internally post-tensioned overpass required 6 tendons of 9-15.2 mm diameter strands, while the externally post-tensioned overpass only required 4 tendons of 11-15.2 mm diameter strands to achieve the same performance. This results in 33% fewer post-tensioning anchorages and 18.5% less post-tensioning strand. This is attributed to reduced dead loads, reduced friction losses, and the greater average eccentricity associated with the externally post-tensioned design.
- Due to sustained loads only, the Design 1 overpass has an estimated positive camber of 10.1 mm at an age of 75 years, while the Design 2 overpass has an estimated positive camber of 10.7 mm at an age of 75 years.
- Vehicle live loads applied to the overpass at one year of age cause live load deflections of L/1500 and L/1450 for Design 1 and Design 2 respectively. This difference in deflection is attributed to the slightly smaller stiffness of the externally post-tensioned design.
- The consideration of accidental tendon loss for externally post-tensioned structures shows that tendon loss affects serviceability foremost, where the loss of two tendons could possibly result in cracking, and would definitely cause downward deflection. For the factored moment capacity to approach the ultimate factored moment demand, three of the four external tendons would need to be lost. Thus, the sequential loss of external tendons will produce visible cracking and deflection giving warning prior to structural failure.
- The use of CSA S6-00, which neglects the stress increase in exterior tendons is conservative, but not punitively conservative. The prediction of ultimate moment capacity made using AASHTO 1998 is 4% greater than the prediction made using CSA S6-00.

5.8 References

AASHTO. 1998. *LRFD Bridge Design Specifications - Second Edition*, American Association of State Highway and Transportation Officials, Washington, D.C.

ACI Committee 209. 1997. *Prediction of Creep, Shrinkage, and Temperature Effects in Concrete Structures, (ACI 209R-92),* American Concrete Institute, Farmington Hills, MI.

Canadian Prestressed Concrete Institute. 1996. *CPCI Design Manual 3rd Edition*, Canadian Prestressed Concrete Institute, Ottawa, Ontario, Canada.

Comité Euro-International du Béton. 1993. *CEB-FIP Model Code 1990*, Thomas Telford Services Ltd., London.

Canadian Standards Association. 2000. *S6-00 Canadian Highway Bridge Design Code*, CSA International, Toronto, Ontario, Canada.

MacGregor, J. G. and Bartlett, M. 2000. *Reinforced Concrete Mechanics and Design*, Prentice Hall Canada Inc, Scarborough, Ontario, Canada.

Summary, Conclusions, and Recommendations

6.1 Summary

The present work consists of a research project involving a case study analysis of a highway overpass, and an alternative design utilising external post-tensioning. The final objective of this research project was to investigate the implications of changing the structural system of the 130th Avenue and Deerfoot Trail Overpass, from internal post-tensioning to external post-tensioning

The structure studied is the two-span 130th Avenue and Deerfoot Trail Overpass in Calgary, Alberta. The construction uses precast-prestressed trapezoidal concrete girders as the main structural elements. The girders are erected, deck and diaphragms are poured, and after the cast-in-place concrete reaches sufficient strength, the structure is longitudinally post-tensioned.

In Chapter 3, a research program was designed to investigate the time-dependent properties of the concrete used in the girders. The objectives of this study were to experimentally determine the mechanical properties of the mix, assess the abilities of

current model codes to predict the mechanical properties, propose a straightforward statistical method to fit laboratory test data to a general model, and propose a method of determining variability of the fitted model.

In Chapter 4, a field study was designed to measure the behaviour the highway overpass. Two precast, prestressed girders were instrumented and monitored for strains and deflections from fabrication to service. The objectives of this study were to identify and use a structural analysis methodology that could be used to predict the time-dependent behaviour of the overpass, and to determine how different analysis methods and concrete models affect the accuracy of prediction.

In Chapter 5, an analytical study was performed to determine the effects of changing the structural system of the overpass from internally post-tensioned to externally post-tensioned. In this study, two overpasses were designed to have comparable behaviour under service and ultimate conditions, and were designed to meet the requirements of the original design. The concrete properties measured in Chapter 3 were used to describe the mechanical properties, and the analysis methodology, summarised in Chapter 4, was used to predict the behaviour of the overpass in service. As well, a literature review, summarised in Chapter 2, was conducted to identify the differences associated with changing the structural system from internal post-tensioning to external post-tensioning, and determine how to incorporate these differences into analysis.

6.2 Conclusions

From the results of the experimental program and analyses presented in Chapter 3, the following conclusions are drawn:

- For the concrete mix studied, the CEB MC-90 model code provided the best prediction of concrete behaviour and ACI 209 provided the second best prediction of behaviour.
- The method proposed to fit measured lab data to a material model was simple, straightforward, and provides an accurate description of the concrete's mechanical

behaviour. The model chosen can be easily incorporated into structural design, and can also provide confidence intervals on the predicted behaviour.

- In the case that a probabilistic analysis is warranted, the certainty in predictions of the fitted model is much greater than that of CEB MC-90. The range of extreme behaviour for CEB MC-90 was nearly 10 times greater than that of the fitted model, Model A when predicting creep, and was over 20 times greater when predicting shrinkage.

From the results of the experimental program and analyses presented in Chapter 4, the following conclusions are drawn:

- The use of either the Effective Modulus Method or the Age-Adjusted Elastic Modulus Method with a material model that can accurately describe the concrete's mechanical properties, and a sufficient structural model will give accurate predictions of the time-dependent deformations.
- For the case study considered, the Age-Adjusted Elastic Modulus Method and the Effective Modulus Method produce predictions that diverge from one another. However, based on the measured field data, neither method can be considered to give more accurate predictions of deflected shape than the other.
- In this study, the use of either ACI 209 or CEB MC-90 to predict the material properties of the girder and deck result in an overestimate of the magnitude of curvature and deflection.
- Compared to the predictions made using ACI 209 and CEB MC-90, the use of the material model that was tuned to measured laboratory data resulted in an increase in accuracy. This increase in accuracy was evident in the prediction of both mid-span deflection and curvature.

From the results of the analytical design study presented in Chapter 5, the following major conclusions of the differences between the design using internal tendons and the design using external tendons are drawn:

- With the externally post-tensioned structure, the elimination of ducts in the webs is possible, allowing for a thinner web width. This resulted in a lighter concrete section with 15% less girder concrete and 5.5% fewer pre-tensioned strands.
- The reduced friction losses in external post-tensioning allowed sufficient stress levels in the tendons to be obtained using alternate-end, single-end stressing and thereby reducing the number of jack set-ups by 67%.
- The internally post-tensioned overpass required 6 tendons of 9-15.2 mm diameter strands, while the externally post-tensioned overpass only required 4 tendons of 11-15.2 mm diameter strands to achieve the same performance. This results in 33% fewer post-tensioning anchorages and 18.5% less post-tensioning strand. This is attributed to reduced dead loads, reduced friction losses, and the greater average eccentricity associated with the externally post-tensioned design.
- The consideration of accidental tendon loss for externally post-tensioned structures shows that tendon loss affects serviceability foremost, where the loss of two tendons could possibly result in cracking, and would definitely cause downward deflection. For the factored moment capacity to approach the ultimate factored moment demand, three of the four external tendons would need to be lost. Thus, the sequential loss of external tendons will produce visible cracking and deflection giving warning prior to structural failure.
- The use of CSA S6-00, which neglects the stress increase in exterior tendons is conservative, but not punitively conservative. The prediction of ultimate moment capacity made using AASHTO 1998 is 4% greater than the prediction made using CSA S6-00.

6.3 Recommendations

The results of the comparative study show that the alternate design using external post-tensioning has possible cost-saving advantages associated with the reduced materials required, specifically concrete quantities and prestressing strands, and with the reduced number of post-tensioning jack set-ups. As well, the reduced weight of the section and additional possible drape of the external tendons also indicate that the externally post-tensioned design may have an advantage in longer spans. The following recommendations are made following this research program:

- Thus far a material comparison has been performed. A cost-estimate is recommended to determine whether the externally post-tensioned design has an economic benefit.
- A possible limiting factor in some overpass designs is span length. Perform an analytical study to investigate design limits for longer span lengths.
- Prior to a detailed design, a dynamic analysis should be conducted to see whether the external tendons can be excited. This is to determine if there is a need for intermediate supports.

Appendix A

Girder Load Effects

A.1 Live Load

The live load is based on the CSA S6-00 CL-W loading (CL-W). The magnitude of weight is specified as W = 800 kN by Alberta Transportation.

The load effects due to live load were calculated using Beam Analysis Program by Juntunen Bridge Systems (2001), which performs a moving load analysis.

A.2 Girder Load Effects

The determination of girder load effects due to live loads is a function of the geometry and stiffness of the bridge cross-section. Table A.1 summarises the relevant parameters and their values for the bridge designed. The formulae in CSA S6-00 are lengthy, and not all equations are shown.

Table A.1: Parameters Used in Girder Load Effect Calculations

Description	Parameter	Value
Number of design lanes	n	7
Number of girders	N	6
Centre-to-centre spacing of girders (m)	S	4.3
Bridge Width (m)	B	24.5
Bridge Span (m)	L	38
Design lane width (m)	W_e	3.5
Modification factor for multilane loading	R_L	0.55

A.3 Girder Moment

The longitudinal moment per girder, M_g, is obtained from the following equation:

$$M_g = F_m M_{gave} \tag{A.1}$$

where M_{gave} is the average moment per girder determined by equally sharing the total moment on the bridge cross-section between all girders, and is determined by the following equation:

$$M_{gave} = \frac{nM_T R_L}{N} = 0.642 M_T \tag{A.2}$$

where, M_T is the moment per design lane, determined from an appropriate live load analysis. For this design, Beam Analysis Program (BAP) was used to determine the moment per design lane.

F_m is an amplification factor, which accounts for the transverse variation in longitudinal moment intensity, or in other words, for load sharing between girders. It is determined from the following equation:

$$F_m = \frac{SN}{F\left(1+\frac{\mu C_f}{100}\right)} \geq 1.05 \tag{A.3}$$

where:

$$\mu = \frac{W_e - 3.3}{0.6} = 0.333 \tag{A.4}$$

$$C_f = 16 - 2\beta \tag{A.5}$$

$$F = (14.5 - 0.7\beta)\frac{nR_L}{2.80} \tag{A.6}$$

The parameter β is a function of the bridges bending stiffness, torsional stiffness, width and length, and is correlated to Equations A.5 and A.6 to describe load sharing between girders.

$$\beta = \pi\left[\frac{B}{L_{eff}}\right]\sqrt{\frac{D_x}{D_{xy}}} \tag{A.7}$$

In Equation A.7, D_x is the total bending stiffness of the bridge cross-section divided by its width, and D_{xy} is the total torsional stiffness of the bridge section divided by the width of the bridge. L_{eff} is the effective girder span, and is 0.6L for positive moment regions and 0.5L for negative moment regions. It's found that 0.5L gives the most conservative solution, and was used for simplicity. The following values of stiffness are used:

$$D_x = 7.53x10^{12}\,N\cdot mm$$

$$D_{xy} = 3.27x10^{12}\,N\cdot mm$$

The girder moment expressed as a function of the moment per design lane is then found to be:

$$M_g = 1.17M_T \tag{A.8}$$

The moment envelope for the girder is shown in Figure A.1.

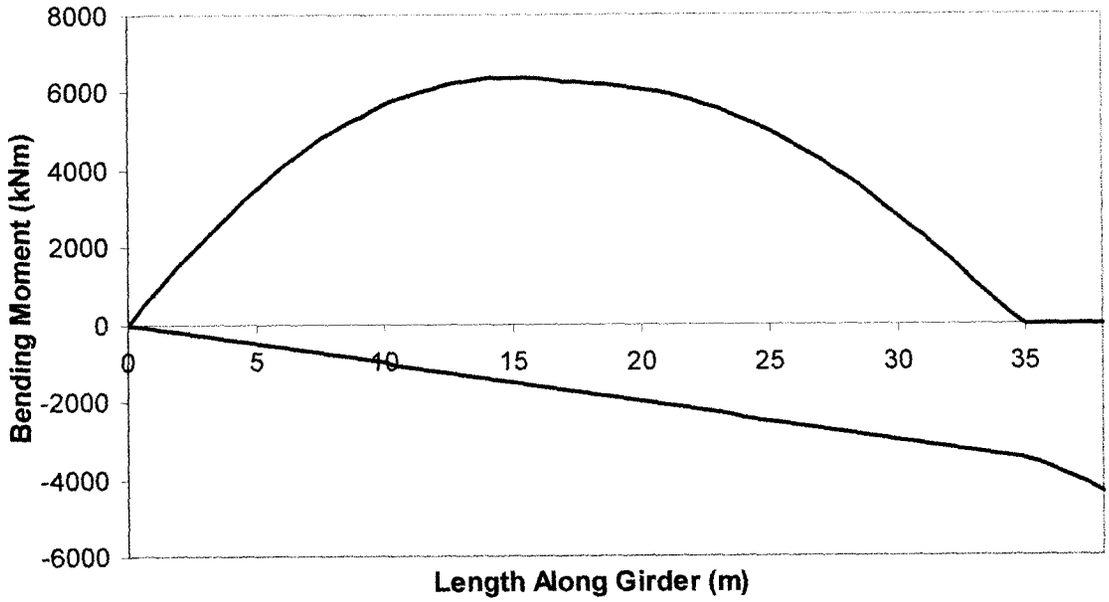

Figure A.1: Unfactored Girder Moment Envelope (Live Load)

A.4 Girder Shear

The longitudinal vertical shear per girder, V_g, is obtained from the following equation:

$$V_g = F_v V_{gave} \tag{A.9}$$

where V_{gave} is the average shear per girder determined by equally sharing the total shear on the bridge cross-section between all girders, and is determined by the following equation:

$$V_{gave} = \frac{nV_T R_L}{N} = 0.642V_T \tag{A.10}$$

where, V_T is the shear force per design lane, determined from an appropriate live load analysis. The parameter F_v is determined from:

$$F_v = \frac{SN}{F} \tag{A.11}$$

The girder shear expressed as a function of the shear per design lane is then found to be:

$$V_g = 1.17 V_T \tag{A.12}$$

The shear envelope for the girder is shown in Figure A.2.

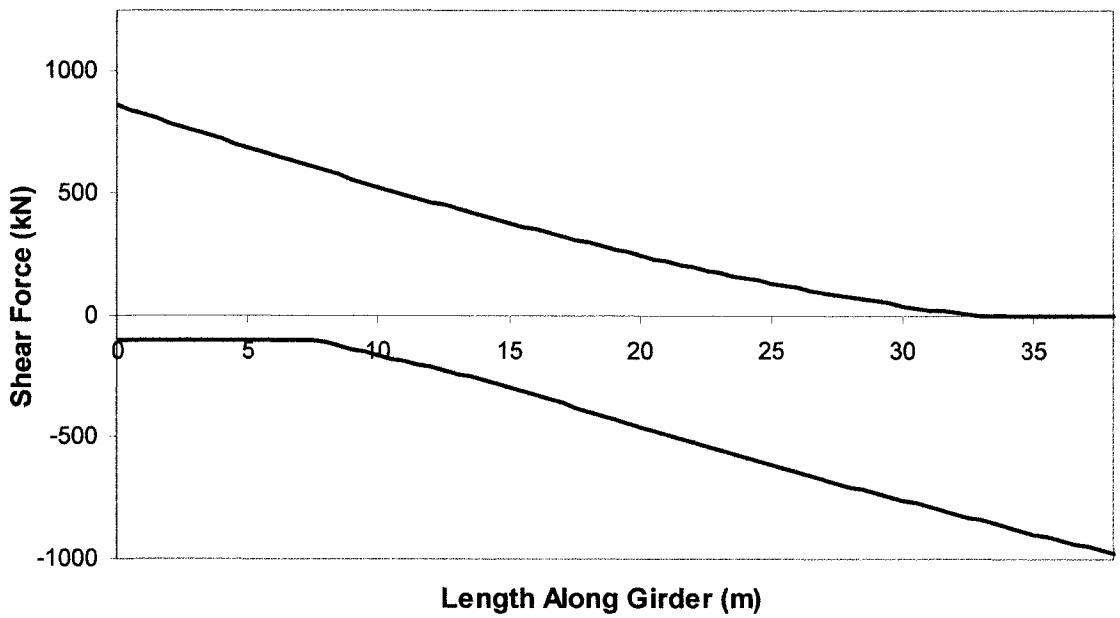

Figure A.2: Unfactored Girder Shear Envelope (Live Load)

A.5 References

Juntunen Bridge Systems. 2001. *Beam Analysis Program Version 3.01.0001*, Lansing, MI, copyright 2001.

Appendix B

Deck Design

B.1 Deck Design by the Empirical Method

This design method is allowed, provided that the system satisfies certain requirements. The bridge deck geometry was selected so that it complies with the requirements of the empirical method. Figure B.1 shows the deck reinforcement as prescribed by the empirical method.

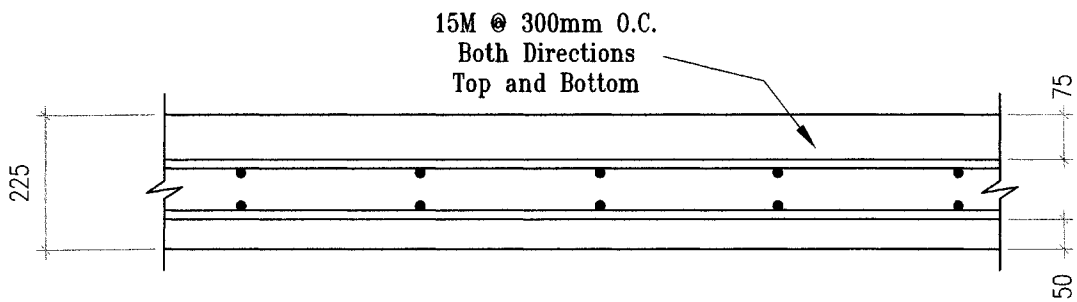

Figure B.1 Deck Slab Reinforcement

The reinforcing bars located closest to the top and closest to the bottom of the slab run perpendicular to the support girders.

The reinforcing ratio has a specified minimum of 0.003 in both directions, where the effective depth, d, is taken as the distance from the top of the slab to the centroid of the lower reinforcement assembly. The reinforcement is 15M bars spaced at 300 mm on centre. This provides a reinforcement ratio of 0.0059. The maximum spacing of reinforcement is 300 mm, which is not exceeded.

Appendix C

Factored Resistance

C.1 Factored Flexural Resistance

The assumptions made in the CSA S6-00 procedure for calculating the factored flexural resistance are those normally made in the flexural theory of concrete members.

The only variation made herein from the CSA S6-00 procedure is in the calculation of tendon stress. For bonded tendons, CSA S6-00 provides an approximate equation for stress increase at ultimate. Herein, strain compatibility is used to determine stress increase in bonded tendons. For these tendons, the effective stress (and associated strain) are taken from a reference state, where initial losses and long-term losses are accounted for. This is similar to the method outline in the Canadian Prestressed Concrete Institute (1996) Recommendations. For externally unbonded tendons, the stress increase is calculated in two methods; using CSA S6-00 and by using the recommendations of AASHTO.

The moment resistance was calculated in a section-by-section approach using an iterative algorithm to determine the curvature that meets the requirement of equilibrium. The concrete strain at ultimate is 0.0035. In calculation of the factored moment resistance, only the calculations for the mid-span sections are presented. Calculations were done at sections every 500mm along the span.

C.1.1 Design 1 – Internal Post-Tensioning

The mid-span section is shown in Figure C.1, with the ultimate strain distribution. In calculating the moment resistance, the different materials are treated separately. Table C.1 contains a summary of the materials considered, and their properties at the ultimate

condition. Note that the bottom flange ordinary reinforcement is located in the same planes as the pretensioning strands.

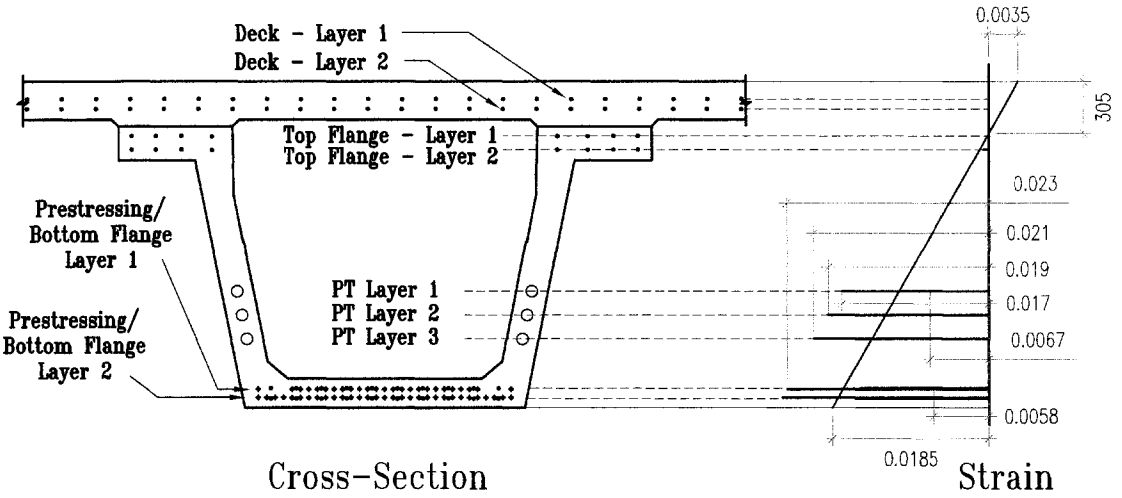

Figure C.1: Flexural Steel Layout and Strain Distribution at Ultimate – Design 1

Table C.1: Calculation of Factored Flexural Resistance – Design 1

Reinforcing Steel	y [mm]	A [mm^2]	ε_{ult}		$\phi_s\sigma$ [MPa]	F [N]	M [Nmm]
Deck - Layer 1	1796	2200	-0.00213		0	0	0
Deck - Layer 2	1744	2200	-0.00154		0	0	0
Top - Layer 1	1590	1600	0.00023		41.3	66.1×10^3	105×10^6
Top - Layer 2	1510	1600	0.00115		207	331×10^3	499×10^6
Bottom - Layer 1	110	2000	0.0172		360	720×10^3	79.2×10^6
Bottom - Layer 2	60	2000	0.0178		360	720×10^3	43.2×10^6

Pretensioning	y [mm]	A [mm^2]	ε_{pe}	ε_{ult}		$\phi_p\sigma$ [MPa]	F [N]	M [Nmm]
PS Layer 1	110	3360	0.00582	0.02193		1726	5.80×10^6	638×10^6
PS Layer 2	60	4340	0.00582	0.02361		1727	7.49×10^6	450×10^6

Post-Tensioning	y [mm]	A [mm^2]	ε_{po}	ε_{pe}	ε_{ult}	$\phi_p\sigma$ [MPa]	F [N]	M [Nmm]
PT Layer 1	684	2520	0.00698	0.00673	0.0174	1710	4.31×10^6	2.95×10^9
PT Layer 2	544	2520	0.00700	0.00676	0.0190	1716	4.33×10^6	2.35×10^9
PT Layer 3	405	2520	0.00703	0.00679	0.0206	1721	4.34×10^6	1.75×10^9

Concrete	y [mm]	a [mm]	b [mm]	A [mm^2]	$\phi_c\alpha_1 f'_c$ [MPa]	F [N]	M [Nmm]
Deck	1803	225	4300	967500	26.4	-25.6×10^6	-46.1×10^9
Top Flange	1665	25.1	1340	33634	34.2	-1.15×10^6	-1.93×10^9

Curvature	ψ =	1.15×10^{-5} [1/mm]	Σ F =	0	[N]
Depth of neutral axis	c =	305.0 [mm]	Σ M =	39.7×10^9	[Nmm]

It is seen in Table C.1 that the steel in the deck is not considered to provide any compressive resistance. This is because it is not practical to provide the ties necessary to consider the longitudinal steel as compression reinforcement.

The force, F, and moment, M, include the appropriate resistance factors, which are summarised in Table 5.4.

For pretensioned steel, the effective strain is the strain in the pretensioned steel after elastic losses and long-term relaxation. For this case, the losses resulting from friction at jacking, anchor set, and immediate elastic shortening amount to 6.3%, long-term losses due to creep and shrinkage were calculated to be 4.4%, losses from relaxation of the steel were calculated to be 2.4%, and losses from elastic shortening due to post-tensioning result in 3.4%. A jacking stress of $0.75f_{pu}$ minus losses gives an effective pretensioned strain of 0.0058.

For internal post-tensioning steel, the effective strain takes the same definition, but due to the parabolic profile, the effective strain varies along the length of the tendon. Here, the recommendations from CPCI (1996) are used to calculate the strain after stressing. The algorithm developed to analyse the structure can also provide the strain in the post-tensioning after all losses. It was found for the mid-span section that the effective post-tensioning steel strain after all losses is 0.00673 for the top layer, 0.00676 for the middle layer, and 0.00679 for the bottom layer.

Using the strain compatibility approach, the factored moment resistance of the mid-span section was found to be 39.7×10^3 kNm.

C.1.2 Design 2 – External Post-Tensioning

Two methods were used to calculate the stress increase in the external tendons at ultimate. The calculation of the ultimate moment resistance in both cases is similar to Design 1, and to avoid redundancy only differences are noted.

Design 2 Ultimate Moment Resistance using CSA S6-00

The mid-span section is shown in Figure C.2, with the ultimate strain distribution. Table C.2 contains a summary of the materials considered, and their properties at the ultimate condition.

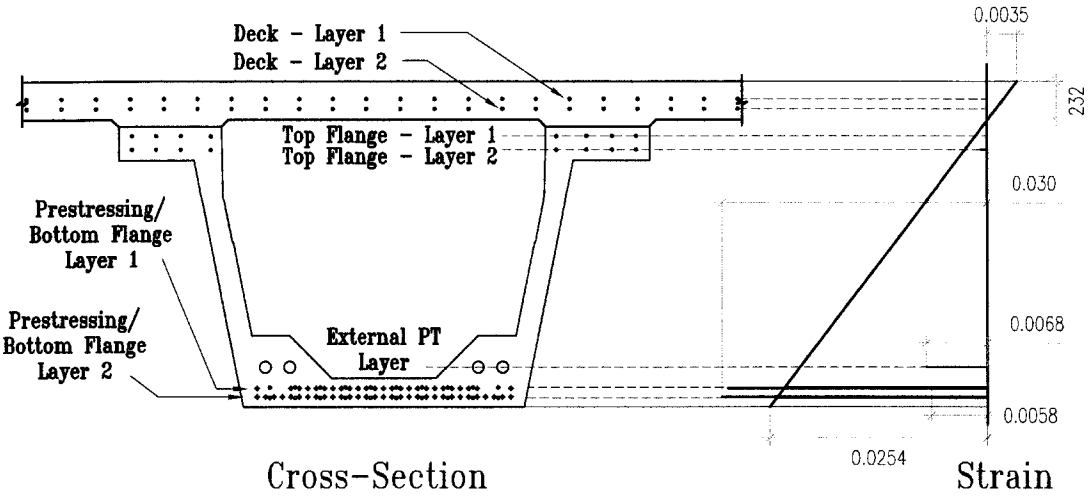

Figure C.2: Flexural Steel Layout and Strain Distribution at Ultimate – Design 2

CSA S6-00 Recommendations

Table C.2: Calculation of Factored Flexural Resistance – Design 2
CSA S6-00 Recommendations

Reinforcing Steel	y [mm]	A [mm^2]	ε_{ult}		$\phi_s\sigma$ [MPa]	F [N]	M [Nmm]
Deck - Layer 1	1796	2200	-0.0017		0	0	0
Deck - Layer 2	1744	2200	-0.00091		0	0	0
Top - Layer 1	1590	1600	0.00141		255	$407x10^3$	$648x10^6$
Top - Layer 2	1510	1600	0.00262		360	$576x10^3$	$870x10^6$
Bottom - Layer 1	110	2000	0.02379		360	$720x10^3$	$79.2x10^6$
Bottom - Layer 2	60	2000	0.02455		360	$720x10^3$	$43.2x10^6$

Pretensioning	y [mm]	A [mm^2]	ε_{pe}	ε_{ult}		$\phi_p\sigma$ [MPa]	F [N]	M [Nmm]
PS Layer 1	110	3220	0.0058	0.0296		1734	$5.59x10^6$	$614x10^6$
PS Layer 2	60	4060	0.0058	0.03035		1735	$7.04x10^6$	$423x10^6$

Post-Tensioning	y [mm]	A [mm^2]	ε_{po}	ε_{pe}	ε_{ult}	$\phi_p\sigma$ [MPa]	F [N]	M [Nmm]
External Layer	350	6160	0.0068	0.00656	0.0066	1216	$7.49x10^6$	$2.62x10^9$

Concrete	y [mm]	a [mm]	b [mm]	A [mm^2]	$\phi_c\alpha_1 f'_c$ [MPa]	F [N]	M [Nmm]
Deck	1816	198	4300	852994	26.4	$-22.5x10^6$	$-40.9x10^9$

Curvature	ψ =	$1.51x10^{-5}$	[1/mm]	Σ F =	0	[N]
Depth of neutral axis	c =	232	[mm]	Σ M =	$35.6x10^9$	[Nmm]

The same approach of strain compatibility is used for all materials except the external post-tensioning. CSA S6-00 specifies that when calculating the ultimate moment resistance for structures with external tendons, there is no increase in tendon stress beyond the effective stress, i.e. $\Delta f_{ps} = 0$ MPa. Thus any actual increase in tendon stress is neglected.

Using this approach, the factored moment resistance of the mid-span section for the externally post-tensioned design was found to be 35.6×10^3 kNm.

Design 2 Ultimate Moment Resistance using AASHTO

The mid-span section is shown in Figure C.3, with the ultimate strain distribution. Table C.3 contains a summary of the materials considered, and their properties at the ultimate condition.

AASHTO provides an equation to predict stress increase past effective stress, which is based on a collapse mechanism resulting from the formation of plastic hinges. It is recommended for internal unbonded tendons, but is considered reasonable for external post-tensioning when second-order effects associated with the loss of tendon eccentricity are minimised by the use of a mid-span deviator. The equation is:

$$f_{psu} = f_{pe} + \frac{6300}{l_e}(d_{ps} - c) \leq f_{py} \quad \text{(MPa)} \tag{C.1}$$

At mid-span, the external tendon has an effective strain of 0.0066, the depth of the external post-tensioning, d_{ps}, is 1525 mm, the effective length, l_e, is 38072 mm, and the depth of the neutral axis, c, is found to be 243 mm. Equation C.1 then has the value:

$$f_{psu} = 0.0066 \cdot 195000\text{MPa} + \frac{6300}{38072}(1525 - 243) = 1492\text{MPa} \leq f_{py} \tag{C.2}$$

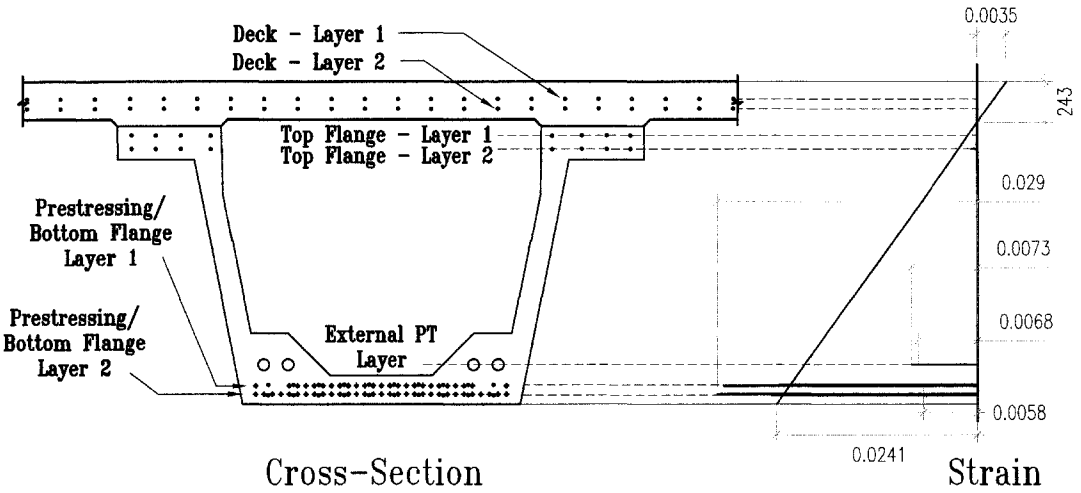

Figure C.3: Flexural Steel Layout and Strain Distribution at Ultimate – Design 2

AASHTO Recommendations

Table C.3: Calculation of Factored Flexural Resistance – Design 2
AASHTO Recommendations

Reinforcing Steel	y [mm]	A [mm^2]	ε_{ult}		$\phi_s\sigma$ [MPa]	F [N]	M [Nmm]
Deck - Layer 1	1796	2200	-0.00179		0	0	0
Deck - Layer 2	1744	2200	-0.00104		0	0	0
Top - Layer 1	1590	1600	0.00117		212	$338x10^3$	$537x10^6$
Top - Layer 2	1510	1600	0.00232		360	$576x10^3$	$870x10^6$
Bottom - Layer 1	110	2000	0.02245		360	$720x10^3$	$79.2x10^6$
Bottom - Layer 2	60	2000	0.02317		360	$720x10^3$	$43.2x10^6$

Pretensioning	y [mm]	A [mm^2]	ε_{pe}	ε_{ult}		$\phi_p\sigma$ [MPa]	F [N]	M [Nmm]
PS Layer 1	110	3220	0.0058	0.0283		1733	$5.58x10^6$	$614x10^6$
PS Layer 2	60	4060	0.0058	0.0290		1734	$7.04x10^6$	$422x10^6$

Post-Tensioning	y [mm]	A [mm^2]	ε_{po}	ε_{pe}	ε_{ult}	$\phi_p\sigma$ [MPa]	F [N]	M [Nmm]
External Layer	350	6160	0.0068	0.00656	0.0073	1417	$8.73x10^6$	$3.06x10^9$

Concrete	y [mm]	a [mm]	b [mm]	A [mm^2]	$\phi_c\alpha_1 f'_c$ [MPa]	F [N]	M [Nmm]
Deck	1816	209	4300	897516	26.4	$-23.7x10^6$	$-42.9x10^9$

Curvature	ψ =	$1.44x10^{-5}$	[1/mm]	ΣF =	0 [N]
Depth of neutral axis	c =	243	[mm]	ΣM =	$37.3x10^9$ [Nmm]

Using this approach, the factored moment resistance of the mid-span section for the externally post-tensioned design was found to be 37.3×10^3 kNm.

C.2 Factored Shear Resistance

The approach used to calculate the factored shear resistance of a section in CSA S6-00 is based on the modified compression field theory. In calculation of the factored shear resistance, only the calculations for the critical sections, d away from the pier, are presented. Calculations were done at sections every 500 mm along the span. The factored shear resistance is the sum of the concrete contribution, the shear steel contribution and the prestressing and post-tensioning steel contribution.

$$V_r = V_c + V_s + \phi_p V_p \tag{C.3}$$

C.2.1 Parameter Values

Many parameters used in the determination of factored shear resistance are common to both designs. The steel used for transverse reinforcement has a yield strength, F_y, of 400 MPa, and the concrete of the girder has a specified compressive strength, f'_c, of 60 MPa.

In Design 1, the factored load effects as determined per girder at the critical section, d away from the pier, are:

$$N_f = 0\text{kN} \tag{C.4}$$

$$V_f = 2.76 \times 10^3 \text{kN} \tag{C.5}$$

$$M_f = 8.40 \times 10^3 \text{kN} \cdot \text{m} \tag{C.6}$$

In Design 2 at the same location, the factored loads as determined per girder, are:

$$N_f = 0\text{kN} \tag{C.7}$$

$$V_f = 2.69 \times 10^3 \text{kN} \tag{C.8}$$

$$M_f = 8.24 \times 10^3 \text{kN} \cdot \text{m} \tag{C.9}$$

There is no vertical contribution from the pretensioning in either design. For Design 1 the contribution from the internal post-tensioning per girder is:

$$V_p = 516\text{kN} \tag{C.10}$$

For Design 2, the contribution from the external post-tensioning per girder is:

$$V_p = 515\text{kN} \tag{C.11}$$

The effective web width, b_v, is taken as the minimum web width within the effective shear depth, d_v. It is reduced by half the diameter of grouted ducts that are located within the depth. Thus, for Design 1, the effective web width for the girder is:

$$b_v = 2 \times (180\text{mm} - 0.5 \times 76\text{mm}) = 284\text{mm} \tag{C.12}$$

For Design 2, there are no ducts in the section, and thus the whole width is effective. It is found to be:

$$b_v = 2 \times (125\text{mm}) = 250\text{mm} \tag{C.13}$$

The effective shear depth, d_v, is taken as the distance between the resultants of the tensile and compressive forces due to flexure, but need not be less than 0.72h, where h is the overall section depth. It was found for both designs that at the critical section for shear,

the calculated value for d_v was less than the minimum value of 0.72h. Thus, for both designs the minimum value is used:

$$d_v = 0.72 \times 1915\text{mm} = 1379\text{mm} \tag{C.14}$$

In accordance with CSA S6-00, the decompression stress, f_{po}, may be taken as 110% of the effective stress.

C.2.2 Design 1 – Internal Post-Tensioning

Concrete Contribution

The concrete contribution is calculated from:

$$V_c = 2.5\beta\phi_c f_{cr} b_v d_v \tag{C.15}$$

where, for sections with at least the minimum transverse reinforcement, the value for β comes from a table. It is found as a function of the longitudinal strain, ε_x, the ratio $v/\phi_c f'_c$. The longitudinal strain is also a function of the crack angle, θ, which is located in the same table as β. The process to convergence is iterative, but usually only takes 2 iterations.

The nominal shear stress, v, is determined from the following equation, and may not exceed $0.25\phi_c f'_c$.

$$v = \frac{V_f - \phi_p V_p}{b_v d_v} \tag{C.16}$$

Thus, at the critical section, the nominal shear stress is:

$$v = 5.80\text{MPa} < 11.3\text{MPa} \tag{C.17}$$

The criterion for section nominal shear stress is satisfied. Then, the ratio $v/\phi_c f'_c$ is found to be:

$$\frac{v}{\phi_c f_c'} = 0.129 \tag{C.18}$$

The longitudinal strain is determined from:

$$\varepsilon_x = \frac{0.5N_f + 0.5(V_f - \phi_p V_p)\cot\theta + {M_f}/{d_v} - A_{ps}f_{po}}{E_s A_s + E_p A_{ps}} \leq 0.002 \tag{C.19}$$

At the critical section, convergence is found with $\theta = 25^\circ$ and β=0.212. The concrete contribution as defined by Equation C.15 is found to be:

$$V_c = 483\text{kN} \tag{C.20}$$

Transverse Steel Contribution

In the case that the transverse reinforcement is perpendicular to the longitudinal axis, the steel contribution is computed from:

$$V_s = \frac{\phi_s f_y A_v d_v \cot\theta}{s} \tag{C.21}$$

The design spacing, d away from the pier, is 80 mm on centre, with 2 layers of 10 M bars per web. This gives a transverse steel area of 400 mm^2. The steel contribution is then calculated to be:

$$V_s = 5.32 \times 10^3 \text{kN} \tag{C.22}$$

Pretensioned Steel Contribution

The pretensioned steel provides no contribution. The post-tensioning provides:

$$\phi_p V_p = 490\text{kN} \tag{C.23}$$

Factored Shear Resistance

From Equation C.3 the factored shear resistance is then calculated to be:

$$V_r = 483\text{kN} + 5.32\times10^3\,\text{kN} + 490\text{kN} = 6.29\times10^3\,\text{kN} \tag{C.24}$$

C.2.3 Design 2 – External Post-Tensioning

Concrete Contribution

For this design, the nominal shear stress is determined to be:

$$v = 6.37\text{MPa} < 11.3\text{MPa} \tag{C.25}$$

This satisfies the criterion for section nominal shear stress. The ratio $v/\phi_c f'_c$ is then found to be:

$$\frac{v}{\phi_c f_c'} = 0.142 \tag{C.26}$$

At the critical section, Equation C.19 is found to converge with $\theta = 25^\circ$ and β=0.212. The concrete contribution as defined by Equation C.15 is found to be:

$$V_c = 425\text{kN}$$

Transverse Steel Contribution

In the case that the transverse reinforcement is perpendicular to the longitudinal axis, the steel contribution is computed from:

$$V_s = \frac{\phi_s f_y A_v d_v \cot\theta}{s} \tag{C.27}$$

The design spacing at the section considered is 40 mm on centre, with 1 layer of 10 M bars per web. This gives a transverse steel area of 200 mm^2. The steel contribution is then calculated to be:

$$V_s = 5.32 \times 10^3 kN \tag{C.28}$$

Prestressed Steel Contribution

The pretensioned steel provides no contribution. The post-tensioning provides:

$$\phi_p V_p = 489kN \tag{C.29}$$

Factored Shear Resistance

From Equation C.3 the factored shear resistance can then be calculated.

$$V_r = 425kN + 5.32 \times 10^3 kN + 489kN = 6.23 \times 10^3 kN \tag{C.30}$$